ABSTRACT

**DEVELOPMENT OF CORRECTION ALGORITHM FOR PULSED
TERAHERTZ COMPUTED TOMOGRAPHY (THz-CT)**

By

Suman Mukherjee

For last couple of decades, there has been a considerable improvement in Terahertz (THz) science, technology, and imaging. In particular, the technique of 3-D computed tomography has been adapted to the THz range. However, it has been widely recognized that a fundamental limitation to THz computed tomography imaging is the refractive effects of the sample under study. The finite refractive index of materials in the THz range can severally refract THz beams which probe the internal structure of a sample during the acquisition of tomography data. Refractive effects lead to anomalously high local absorption coefficients in the reconstructed image near the material's boundaries. Three refractive effects are identified: (a) Fresnel reflection power losses at the boundaries, (b) an increase in path length of the probing THz radiation, and (c) steering of the THz beam by the sample such that the emerging THz radiation is no longer collected by the THz detector. In addition, the finite size of the THz beam dominates the measured THz transmission when the edges of the sample are probed using THz tomography. These boundary phenomena can dominate in the reconstructed THz-CT images making it difficult to distinguish any hidden finer structural defect(s) inside the material. In this dissertation, an algorithm has been developed to remove these refractive and finite beam size effects from THz-CT reconstructed images. The algorithm is successfully implemented on cylindrical shaped objects.

A longer term goal of the research is to study the internal structure of natural cork wine stoppers by pulsed Terahertz tomography (THz-CT). It has previously been shown that THz imaging can detect the internal structure of natural cork. Moreover, the internal structure of natural cork stoppers dominates the diffusion of gasses and liquids through the cork. By using THz computed tomography, one can recreate a 3D image of the sample's internal structure which could then be used to predict non-destructively the diffusion properties of the cork. However, refractive and boundary effects which arise in the THz tomographic image masks the presence of the cork's internal structure. Applying the correction algorithms which are developed in this dissertation to natural cork stoppers suppresses the refractive and boundary anomalies enabling better visualization of the cork's internal structure.

DEVELOPMENT OF CORRECTION ALGORITHM FOR PULSED TERAHERTZ COMPUTED TOMOGRAPHY (THz-CT)

by
Suman Mukherjee

A Dissertation
Submitted to the Faculty of
New Jersey Institute of Technology
and Rutgers, The State University of New Jersey – Newark
in Partial Fulfillment of the Requirements for the Degree of
Doctor of Philosophy in Applied Physics

Federated Department of Physics

August 2013

APPROVAL PAGE

DEVELOPMENT OF CORRECTION ALGORITHM FOR PULSED
TERAHERTZ COMPUTED TOMOGRAPHY (THz-CT)

Suman Mukherjee

Dr. John F. Federici, Dissertation Advisor	Date
Distinguished Professor of Physics, NJIT	

Dr. Dale Gary, Committee Member	Date
Distinguished Professor of Physics, NJIT	

Dr. Robert Barat, Committee Member	Date
Professor of Chemical Engineering, NJIT	

Dr. Zhen Wu, Committee Member	Date
Professor of Physics, Rutgers University, Newark, NJ	

Dr. Keun Ahn, Committee Member	Date
Assistant Professor of Physics, NJIT	

BIOGRAPHICAL SKETCH

Author: Suman Mukherjee

Degree: Doctor of Philosophy

Date: August 2013

Undergraduate and Graduate Education:

- Doctor of Philosophy in Applied Physics,
  New Jersey Institute of Technology, Newark, NJ, 2013

- Master of Science in Physics,
  Banaras Hindu University, Varanasi, India, 2002

- Bachelor of Science in Applied Physics,
  University of Burdwan, Burdwan, India, 2000

Major: Applied Physics

Presentations and Publications:

S. Mukherjee and J. F. Federici, *Elimination of Fresnel Reflection Boundary Effects and Beam Steering in Pulsed Terahertz Computed Tomography*. 2013. (Submitted)

Z-H. Michalopoulou, S. Mukherjee, Y. L. Hor, K. Su, Z. Liu, R. B. Barat, D. E. Gary, J. F. Federici, *RDX Detection with THz Spectroscopy*. Journal of Infrared, Millimeter, and Terahertz Waves, 2010. **31**(10): pp.1171-1181.

J. F. Federici, R. L. Wample, D. Rodriguez, and S. Mukherjee, *Application of terahertz Gouy phase shift from curved surfaces for estimation of crop yield*. Applied Optics**,** 2009. **48** (7): pp. 1382-1388.

S. Mukherjee, J. F. Federici, *Study of structural defects inside natural cork by pulsed terahertz tomography***.** IRMMW-THz 2011 - 36th International Conference on Infrared, Millimeter, and Terahertz Waves, 2011. art. No. 6104965. (Talk)

S. Mukherjee, J. F. Federici**,** *Study of structural defects inside natural cork by pulsed terahertz tomography.* The 2011 Dana Knox Student Research Showcase*,* NJIT, 2011. (Poster)

Dedicated to my beloved Parents.

ACKNOWLEDGMENT

I am deeply grateful to my advisor, Prof. John Federici at NJIT for suggesting and supervising the work presented in this dissertation. He has been enormously supportive of me throughout the course of my PhD.

I benefitted greatly from the advice and insights of the members of my Dissertation Committees members Prof. Dale Gary, Prof. Robert Barat and Prof. Ken Ahn of NJIT, and Prof. Zhen Wu of Rutgers, Newark.

I am especially grateful to my colleagues and lab mates at NJIT for all their support and encouragement during my PhD program here.

I would like to acknowledge my deepest gratitude towards my family for supporting me all this while. I owe all this to my dear parents, Mr. Debabrata Mukherjee and Mrs. Debi Mukherjee.

Last, but not the least, I would especially like to thank to all my close friends for their constant encouragement and support.

TABLE OF CONTENTS

TABLE OF CONTENTS
(Continued)

LIST OF TABLES

LIST OF FIGURES

Figure   Page

LIST OF FIGURES
(Continued)

CHAPTER 1

INTRODUCTION

1.1 Terahertz (THz) Spectroscopy

In this chapter, a basic introduction to Terahertz radiation, its production, as well as its application in imaging are discussed. While the field of Terahertz radiation is relatively new compared to other regions in the electro-magnetic spectrum, the THz field has rapidly developed from the late 20th century. With the farther development of instrumentation in the field of Terahertz science and technology, scientists have employed it in a variety of areas.
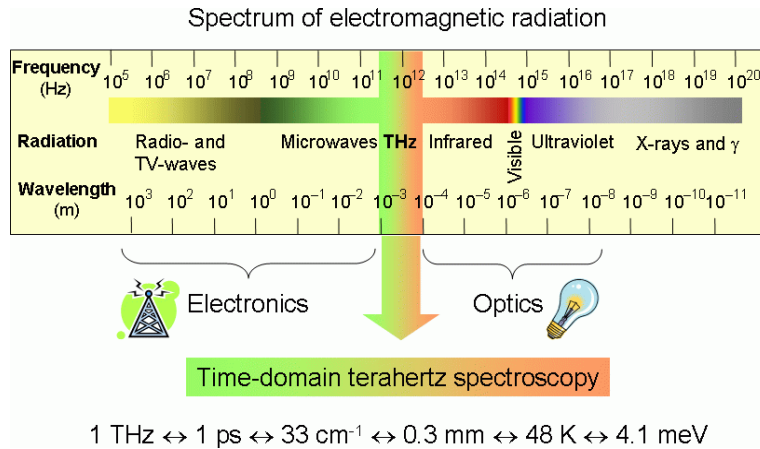
Figure 1.1 Spectrum of electromagnetic radiation. [1]

Terahertz (THz), a part of the electromagnetic spectrum, was one of the least explored areas of spectroscopy and imaging due to lack of proper sources and detectors. The development of new sources and detectors over the past 20 years has enabled a huge growth in THz-related science, spectroscopy, and imaging. The THz region of the

electromagnetic spectrum (Figure 1.1) lies in the gap between microwave and infrared reigns. The pulsed Terahertz region is commonly defined to lie between 0.1 THz to 3 THz (1 THz= 10^{12} cycles/second). Until now there are many viable sources of Terahertz radiation such as the gyrotron, the backward wave oscillator (BWO), the far infrared laser (FIR laser), quantum cascade laser, the free electron laser (FEL), synchrotron light sources, photo mixing sources etc.

Terahertz (THz) spectroscopy and imaging [2] has received considerable attention for non-destructive evaluation of various materials including polymers, pharmaceuticals [3] and detection of concealed weapons and explosives [4] [5]. The technique has also been applied to non-destructive evaluation of moisture content in grain [6] [7], leaves [8] [9] [10], wood [11], as well as polymers [12] [13]. Pulsed Terahertz (THz) imaging was first proposed by Hu and Nuss in 1995 [14]. It utilizes the THz or far-infrared region of the electromagnetic spectrum and is based upon the technique of Terahertz time-domain spectroscopy (THz-TDS). The THz-TDS technique consists of generation and detection of short (a few picoseconds) broad spectral pulses of Terahertz energy via optoelectronic devices [15] [16].

A major advantage of Terahertz time domain spectroscopy (THz-TDS) compared to other THz methods is its exceptional sensitivity and ability to investigate both amplitude and phase of the propagating THz wave simultaneously because it is a phase sensitive measurement. Although the energy of Terahertz beam is very low ($P_{average} < 1\,\mu W$), it opens up a wide spectral widow (0.1 THz- 3 THz) for study.

1.2   Terahertz (THz) Time-domain spectroscopy

The Terahertz (THz) time-domain technique produces electromagnetic pulses whose spectrum typically contains frequencies from 0.1 THz to 3THz. The techniques for generating, manipulating and detecting sub-picoseconds pulses have been shown extensively in the literature [17] [18] [15]. For this work, a commercial THz-TDS system made by Picometrix Inc (T-Ray 2000®) is used. A schematic diagram of the T-Ray 2000 is given below.
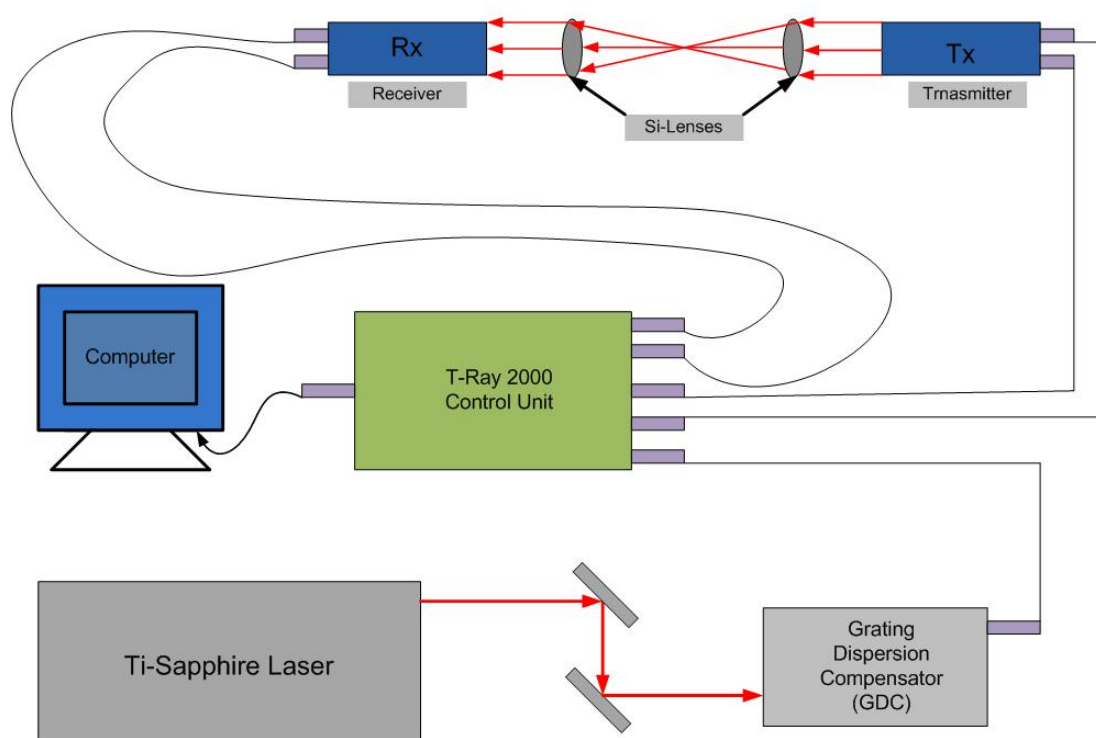
Figure 1.2 Schematic diagram of the T-Ray 2000. [19]

The T-Ray 2000 THz-TDS unit consists of several components (Figure 1.2). The Ti-Sapphire laser is pumped by a Diode Array Laser (Not shown in Figure). A grating dispersion compensator (GDC) is used to compensate for the dispersion in the fiber optical cables which deliver the pulsed laser light to the THz transmitter (TX) and receiver (RX). The control unit includes an optical delay line, which is essential for detecting the THz time-domain waveform. The THz TX and RX consist of photoconductive antenna structures, which convert the energy from the infrared-to-THz spectral range. All the electronics and antennas are packaged inside the TX and RX modules for generation and detection of THz radiation. Two silicon lenses focus the THz beam on the sample. A computer controls the digitization and recording of the THz waveform from the THz RX. Due to the fact that the system utilizes fiber-optic cables to deliver the laser power to the THz transmitter and receiver, with this system one can measure both transmission and reflection spectroscopy simply by changing the orientation of the TX and RX. A typical THz-TDS system consists of many optical components (Figure 1.2) including a femtosecond laser, which produces pulses of near infrared light. The femtosecond laser source used for this dissertation is a Ti:Sapphire laser with a pulse duration of ~100fs. This source consists of several components, which includes a semiconductor diode array pump laser, which produces femtosecond pulses from a Ti-Sa laser. Ti-Sapphire Lasers (also known as TI:Al_2O_3 Lasers titanium-sapphires lasers, or simply Ti:sapphire) are tunable lasers which emit red and near-infrared light in the range from 650nm to 1100nm. The Laser used for generation of THz radiation has a central wavelength around 800nm and a repetition rate of 100 MHz.

The output of the laser is divided into two parts. One generates Terahertz radiation while the other passes through the optical delay line before illuminating the THz detector. Between transmitter and detector, there are two silicon lenses to focus the THz beam on to the desired sample.
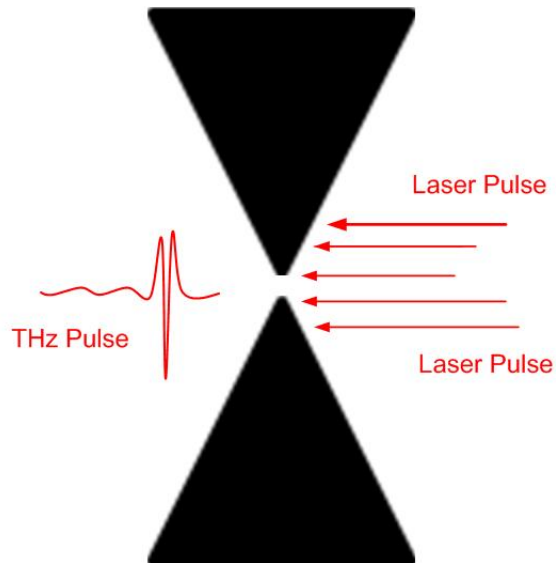
Figure 1.3 THz transmitter antenna made up of low temperature GaAs.

The Terahertz transmitter consists of a photoconductive bow-tie antenna [20] made typically from low temperature GaAs biased by a dc electric field (Figure 1.3). The low temperature GaAs acts as a fast photoconductive switch with a photoconductive lifetime <1ps. A lens (not shown in Figure) mounted above the antenna reduces the divergence of the emitted THZ radiation. For the Picometrix T-Ray 2000 system used for this dissertation, the THz transmitter module uses a bowtie antenna structure (Figure 1.3), a 3cm focal length silicon lens, and a hemispherical lens mounted on the GaAs substrate to produce a collimated THz beam with a beam diameter of roughly 1.5 inches. The

Ti:Sapphire laser light is fiber-optically coupled to both the THz TX and Rx. This enables independent positioning of either unit without time-consuming optical realignment to maintain the laser illumination of the antenna's gap structure.

When a laser pulse falls into the antenna, absorption of energy from the incoming laser pulse generates electron-hole pairs. As the antennas are DC biased, the generated electron-hole pairs are accelerated by the applied biased field and transient current is produced before the photo-generated carriers recombine. The duration of the emitted Terahertz pulse depends upon the recombination time of the electron-hole pairs. According to the Maxwell's electromagnetic theory ($E(t) \propto \dfrac{\partial I(t)}{\partial t}$), the time-varying current produces an electromagnetic wave. The antenna structure is designed to efficiently radiate the electromagnetic wave as a THZ pulse into free space.
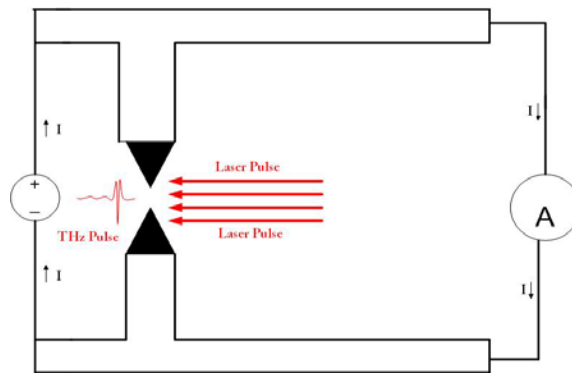
Figure 1.4 Lt-GaAs Photo conducting antenna used for THz detection.

Detection of emitted Terahertz radiation in THz-TDS can either be accomplished by electro-optic or photoconductive sampling [21]. Here photoconductive sampling which is employed in the THz T-Ray 2000 system will be focussed. Photoconductive

sampling is complementary to THz generation by photoconductive antenna structures. Another photo-conducting antenna detects the incident electric field of the THz radiation (Figure 1.4).

Since fast detection electronics operating at THz rates until only very recently, have been not available, a repetitive photoconductive sampling method is used to measure the incoming Terahertz radiation to the detector. In the detector, the photoconductive antenna is not biased with a constant voltage as is done with the THz transmitter. Instead, the incoming THz radiation acts as the electrical bias. In the presence of the THz electric field, a portion of the Ti:Sapphire Laser pulse which is used to generate electron-hole pairs for THz generation, is also used to "gate" or "turn on" the detector. In order to enable the simultaneous arrival of the THz radiation and the laser gating pulse, the gating laser pulse is delayed appropriately so that both the generating and detecting optical path lengths from the beam splitter to the THz detector are equal. On the detector side, the laser pulse generates electron-hole pairs and at the same time, a THz pulse is incident on to the detector antenna. Photo-generated charged particles produce a transient current, which is proportional to the instantaneous THz electric field. The transient current is detected, amplified, and digitized using a computer's Data Acquisition Board for further data processing.

Clearly, it is necessary that the photo carrier lifetime must be much smaller than the pulse duration of the incident THZ pulse so that the detected transient current is proportional to the instantaneous THz electric field present at the detector upon optical illumination. One reconstructs the entire THz field as a function of time by delaying the arrival of the THz beam relative to the gating optical pulse. This is achieved by slowly

scanning the optical delay line. Since all the Terahertz radiation coming from the transmitter antenna is identical, one can completely reproduce the entire Terahertz pulse (a time window of 80 picoseconds) as the delay line is scanned in length. This is called photoconductive sampling. By this method, one does not detect the entire Terahertz pulse at once; rather one samples a point of the Terahertz pulse and reconstructs the entire waveform by successively changing the length of the delay line and recording the value of the waveform for each delay. This process reproduces the entire pulse after several samplings.

During the measurement of THz time domain spectroscopy, one of the most critical elements is to make sure there is good coupling between THz source and THz detector. There are several reasons for the increased care that is required to ensuring good coupling. First, the fact that the size of the photoconductive THz antenna is comparable to the wavelength means the antenna is not highly directional. Additional coupling optics is required to produce a well-collimated THz beam. Second, because the wavelength to beam diameter ratio is much less, for THz pulses than for optical pulses, diffraction plays a larger role in beam propagation and the THz beam can quickly increase in size due to diffraction. Third, because the frequency components that make up the THz pulse typically cover more than a decade in frequency, different frequencies of the pulse have very different propagation characteristics.

Due to the dominance of THz-TDS instrumentation, many research activities are driven by applications of this instrumentation. Applications of THz-TDS spectroscopy and imaging address important problems such as non-destructive testing, as well as new approaches to medical diagnostics and rapid screening of drug development. One of the

research directions in THz science and technology is to increase the bandwidth of short Terahertz frequency radiation pulses. Non-linear optical phenomena such as optical rectification and the linear optical effect are attractive options for broadband generation and detection of THz radiation [21].

A typical THz time-domain waveform and its magnitude are shown in Figure 1.5 and Figure 1.6. From the THz pulse obtained by THz-TDS, one can produce the frequency domain pulse by a fast Fourier transform (FFT). One can retrieve phase as well as amplitude information from the FFT. From the phase and amplitude data, one can calculate both the real and imaginary refractive index of a sample material [17]. Much research has been done in THz-TDS for the spectroscopic measurement of different materials [15] [16] [17].
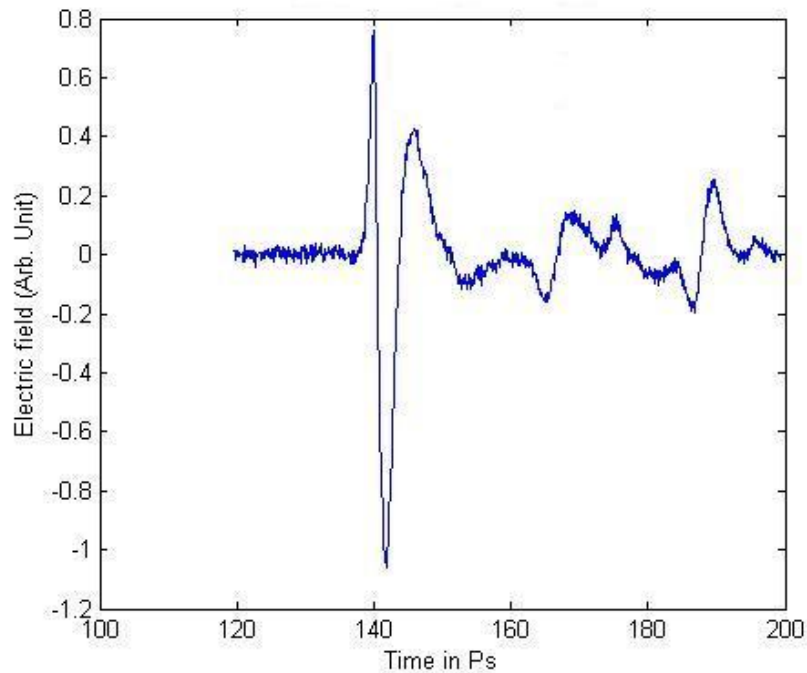
Figure 1.5 Typical pulse as measured with THz Time-domain spectroscopy.
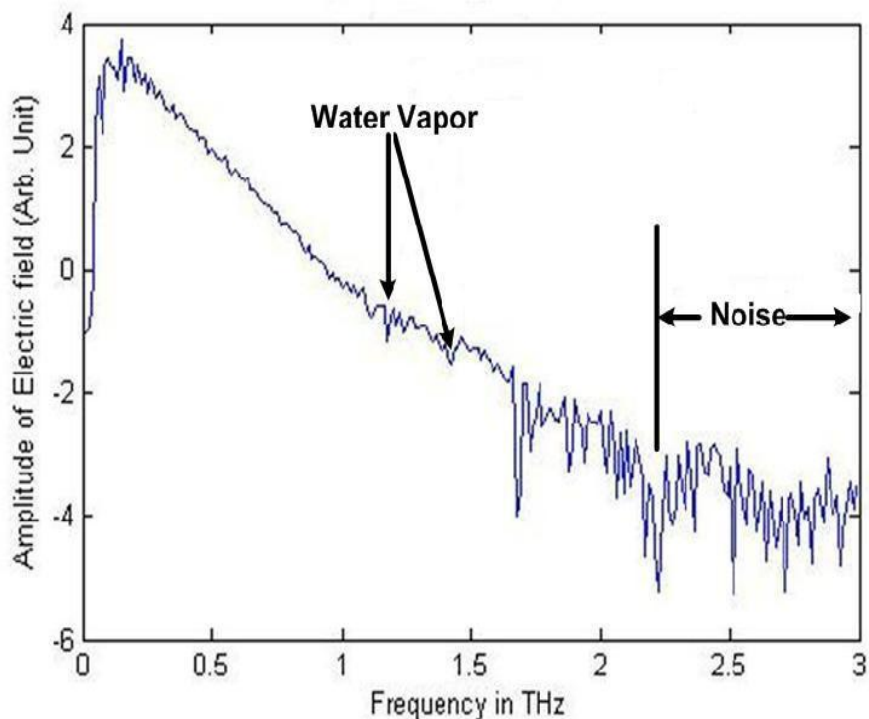
Figure 1.6 Fourier transform of Time-domain spectrum.

1.3 Terahertz (THz) imaging

Another major growth field in the Terahertz domain is Terahertz imaging. In the early 1970s, people faced many challenges in the field of THz imaging because of the lack of proper sources and detectors. At that time the most intense source of THz radiation was the HCN laser operating at 1.12 THz [18]. With the development of the pyro-electric detectors, hot electron bolometers and several types of diode detectors, Fourier Transform Infrared (FTIR) imaging was also becoming a major tool in the far-infrared region. For the last decade, there have been frequent and major developments of Terahertz time domain spectroscopy as an experimental technique. Several new

techniques for generation, manipulation and detection in THz science and technology have revolutionized this field [18]. Many people have shown interest in THz radiation due to its ability to penetrate through many materials in a non-destructive manner. Among the list of proposed uses, people find it important to use THz as security screening and quality control. Many techniques used for THz imaging has been borrowed from other electromagnetic frequency ranges, such as X-Ray CT, and millimeter wave synthetic aperture radar etc. Terahertz imaging has been demonstrated for imaging flames [22], scale-model aircraft [23], leaf moisture content [8], skin burn severity, tooth cavities [24], skin tumors [25] etc. One of the primary advantages of Terahertz imaging is the fact that coherent detection of the broadband pulses provides rich frequency dependent information on the target's far-infrared optical properties.
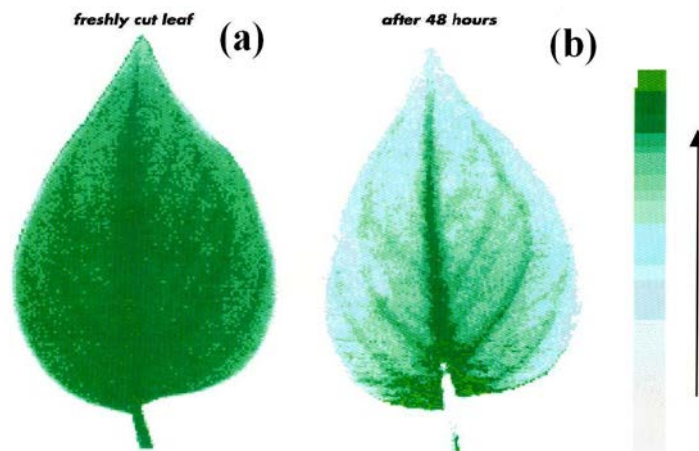
Figure 1.7 (a) The image of a fresh leaf. Attenuation of THz radiation through the leaf is largely due to water within the leaf. (b) THz image of the same leaf after 48 hours. Water has clearly evaporated from the leaf, except from the stems of the leaf. [14]
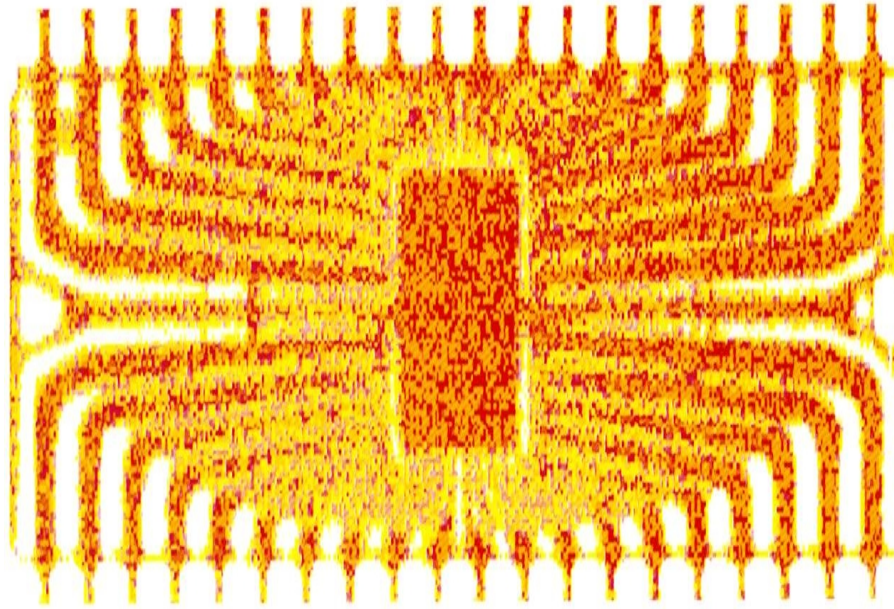
Figure 1.8 THz image of a packaged semiconductor IC. [14]

In its simplest version, the THz-TDS system of Figure 1.2 can be used to image objects by keeping the positions of the transmitter and receiver fixed while varying the position of the sample using motorized translational stages. A 2-D THz image is required a pixel at a time with each pixel corresponding to a different position of the sample. In fact, the first pulsed THz images of a leaf [14] were acquired in this manner (Figure 1.7). Hu and Nuss reported the first images (Figure 1.7 and Figure 1.8) by THz-TDS in 1995 [14]. Their work created a great deal of excitement among the scientific community for subsequent development of THz imaging systems and techniques.

THz-TDS has been used in the majority of research work in the field of THz imaging for more than a decade and in most of the cases THz radiation is generated in the form of single cycle pulses of duration 1ps or less. In addition to the development of

THz-TDS systems, THz CW systems and imaging techniques were developed during this time [26-32]. There has been significant development of THz transmitter and detection mechanisms [33-62]. Reference [63] details a good comparison between pulsed THz-TDS and continuous wave THz imaging.
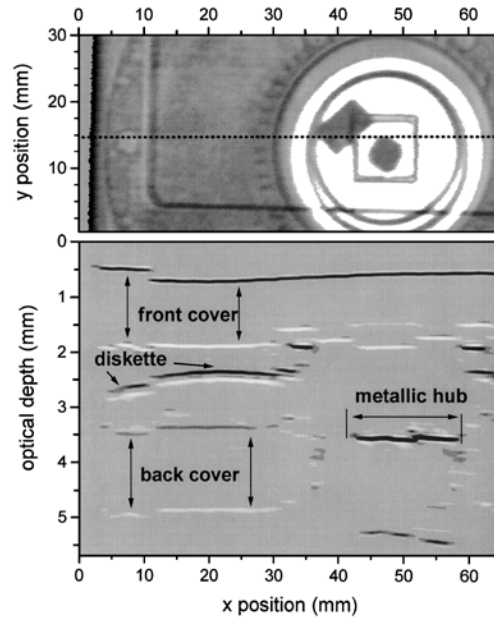
Figure 1.9 Conventional reflective T-Ray Image of a 3.5-inch floppy disk. [64]

As an example of alternative THz imaging hardware, Alan W.M.Lee *et al.* [65] demonstrated THz standoff (> 25m) imaging using a tunable single frequency terahertz quantum cascade laser (QCL) and a room temperature micro bolometer array. Figure 1.10 shows the experimental set-up used by the authors and Figure 1.11 shows the visible and terahertz image of the seed-pod respectively. Here authors demonstrated real-time imaging using a quantum cascade laser.
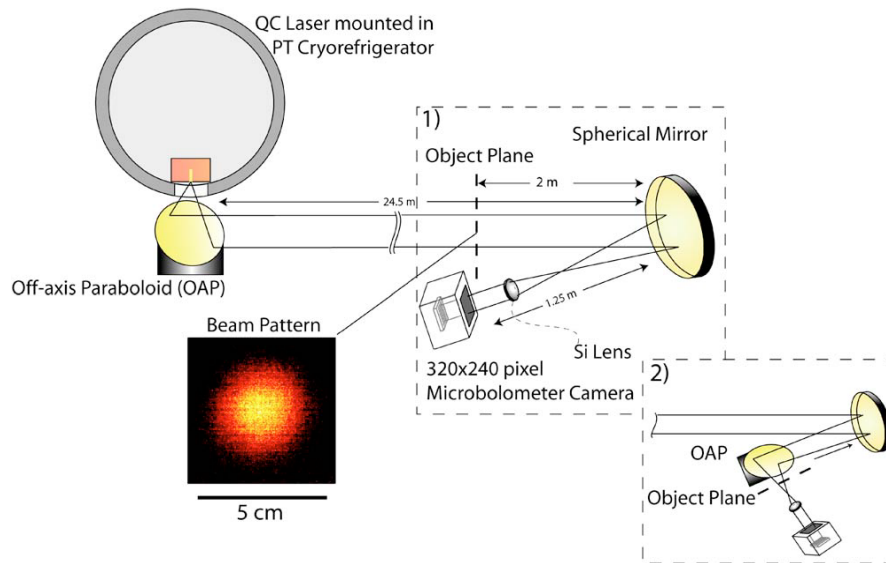
Figure 1.10 Experimental setup for imaging over a distance of 25.75 m. A QCL device is mounted in a pulse-tube cryo-cooler, with emitted beam collimated by an off-axis parabolic mirror, for transmission over a 24.5 m path before collection by a 15 cm diameter spherical mirror. In configuration, (1) an object is placed 2 m before a spherical mirror; in configuration, (2) an object is placed after a second off-axis parabolic mirror. Also shown is the beam pattern for configuration (1) measured at distance 23 m from the laser source and taken with a (320 X 240) element focal-plane array camera with 1 s integration. [65]
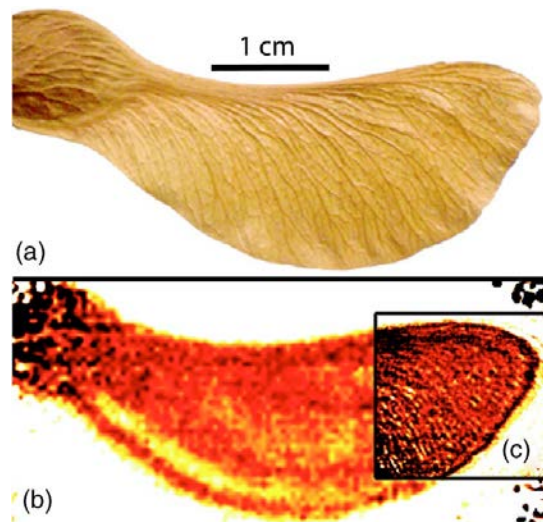
Figure 1.11 Sample images of a dried seed-pod: (a) image at visible freuency, (b) terahertz image taken with configuration (1), and (c)   (Continued to next page)

terahertz image taken with configuration (2). Both (b) and (c) are taken with 1 S integration (average of 20 frames).[65]

It is true that many common materials are transparent in the THz range but there are substances, which are not. THz radiation is highly reflected by metals due to the high free charge carrier density. Living tissues and any living body is highly absorptive in THz radiation because of its water content. As water molecules as well as any polar molecules absorb THz radiation, transmission spectroscopy through a thick layer of those materials is highly improbable. For thick layers, one needs to study reflection spectroscopy. The first demonstration of 3D THz image reconstruction was described in 1997 by Mittleman *et al* [64]. In that work, the authors studied a conventional 3.5-inch floppy disk by reflective T-Ray imaging and reconstructed 3D image of the disk (Figure 1.9).

Recently, much attention has been focused on three-dimensional (3D) THz imaging [15] [16]. THz-TDS and THz imaging is a coherent measurement technology which is based on the measurement of both phase as well as amplitude of the Terahertz pulse at each frequency. THz waves provide temporal and spectroscopic information that allows us to develop various three-dimensional (3D) Terahertz tomography-imaging modalities. There are several different types of three-dimensional Terahertz tomography imaging techniques. These are: Terahertz diffraction tomography (THz-DT), Terahertz computed tomography (THz-CT), THz binary lens tomography and THz digital holography [16, 64]. The interaction between a coherent THz pulse and an object provides rich information about the object under study; therefore, three-dimensional Terahertz imaging can be a very useful tool to inspect or characterize several types of objects.

Tomographic imaging is largely used in X-Ray diagnostics, seismic imaging, synthetic aperture radar, ultrasonic imaging etc. Each of these imaging techniques has their own source and detector configuration and separate algorithm to generate those images. The orientation of the source and detector always depends on the nature of the problem. Tomographic imaging can be achieved by both pulsed and continuous wave THz radiation.

CHAPTER 2

TERAHERTZ TOMOGRAPHY

2.1 Introduction

Tomography is the reconstruction of the internal or external structure of any object or a section of the object by the penetration or diffraction of wave through or by the object. The word tomography came from the Greek word tomos ("part" or "section") and graphein ("to write"). Tomography is not new in the field of imaging and diagnostics. It is a method of reconstruction of images, both 2D and 3D, to study the internal structure of any object or its cross-section. Tomography has a wide range of application in various disciplines, *i.e.*, astrophysics, material science, quantum information, geophysics, biology, oceanography, archeology, radiology etc. Terahertz tomography is a tomographic imaging technique performed using Terahertz radiation. Because Terahertz can penetrate through many materials where visible or IR radiation cannot, unique information can be obtained through Terahertz tomography. It is similar to X-Ray tomography [66] but without the harmful effect of x-ray exposure. Recently, tomography is widely being used in airport security scanning to acquire full or partial body scans. X-Ray computed tomography was first introduced by radiologist Alessandro Vallebona in 1930 and it is being widely used by radiologists all over the world to scan full or parts of animal bodies. With the advancement of more powerful reconstruction algorithms, the application of tomography has not just been limited to the clinics by radiologists, but has spread to different applications, and has been applied in different regions of the electromagnetic spectrum. The following are the various types of tomographic imaging techniques used in different sectors: computed tomography (CT), Single-photon emission computed tomography (SPECT), Magnetic resonance

imaging (MRI), Positron emission tomography (PET), electron tomography, atom probe tomography, magnetic particle imaging etc.

Tomographic images can be generated by both pulsed [16] and continuous wave (CW) [67, 68] Terahertz radiation. In this dissertation, the tomographic work has been performed by pulsed Terahertz radiation [16, 69, 70]. Hence, the focus of this dissertation will be on pulsed Terahertz tomography [64, 71-73]. The various three-dimensional Terahertz tomographic imaging modalities are Terahertz diffraction tomography (THz-DT), Terahertz binary lens tomography, Terahertz digital holography and Terahertz computed tomography (THz-CT) [16].

2.2   THz Computed Tomography

Computed tomography is not a new technique. X-Ray computed tomography was introduced 42 years ago and implemented in medical diagnosis. There has been tremendous development in X-Ray computed tomography for the last many decades. With the instrumentation advancement, X-Ray computed tomography is being used almost everywhere in medical diagnosis. Computed tomography has not remained confined in the area of X-Ray imaging, but has been adapted to different regions of the EM spectrum. The formulation of THz computed tomography has been borrowed from X-Ray CT. Not surprisingly, the measuring techniques in the THz range are also same as technicians used in X-Ray CT. The basis of all tomography comes from Radon transformation, which was introduced by mathematician Johann Radon in 1917 [74].
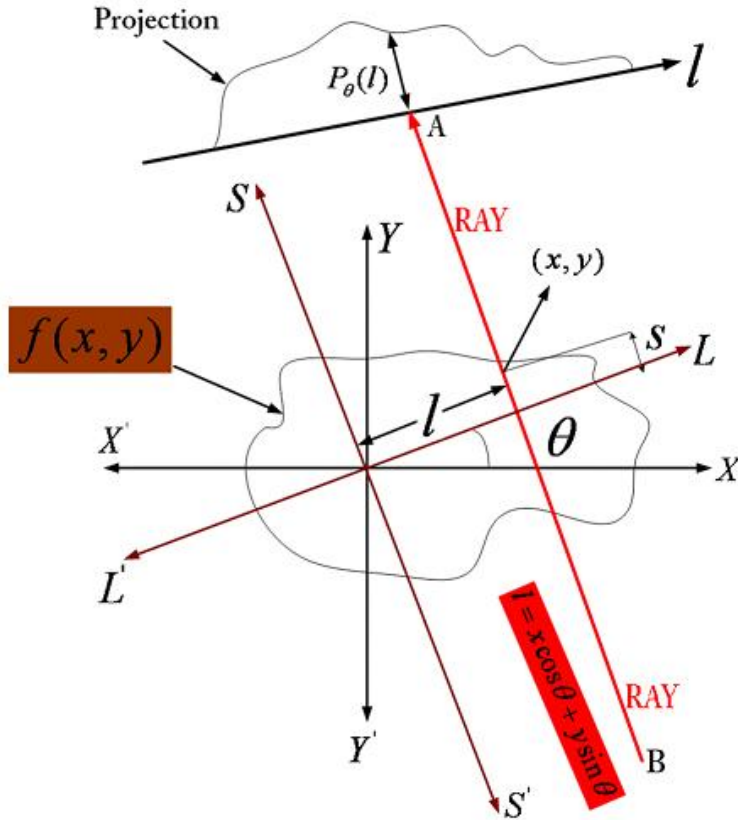
Figure 2.1 An object, $f(x,y)$, and its projection $P_\theta(l)$ are shown for an angle of θ.

The following mathematical basis for tomography [75] is valid for non-diffracting sources. An object is in the space and the object function is defined as $f(x, y)$ shown in Figure 2.1. The attenuation of the THz rays will be considered as they propagate through an object so that $f(x, y)$ represents the local attenuation coefficient of the material. Rays are propagating through the object and the total attenuation is measured along the ray's path through the material ($P_\theta(l)$). $P_\theta(l)$ is called the projection. While the attenuation is measured in the specific example shown, it could also be the time delay of the THz pulse, or any other measureable THz parameter. As the object rotates, the projection is measured at each angular

orientation. The coordinate system defined in Figure 2.1 will be used to describe line integrals and projections. The equation of the line AB in [75] is,

$$x\cos\theta + y\sin\theta = l .$$

(2.1)

The projection ($P_\theta(l)$) can be defined as [75],

$$P_\theta(l) = \int_{(\theta,l)line} f(x,y)ds = \int_{(\theta,l)line} f(x,y)dx\,dy .$$

(2.2)

Equation (2.2) is known as Radon Transformation [74] and this is the basis of both X-Ray and Terahertz computed tomography (THz-CT). Using a delta function, the above equation could be written as [75],

$$P_\theta(l) = \int_{-\infty}^{\infty}\int_{-\infty}^{\infty} f(x,y)\delta(x\cos\theta + y\sin\theta - l)dx\,dy .$$

(2.3)
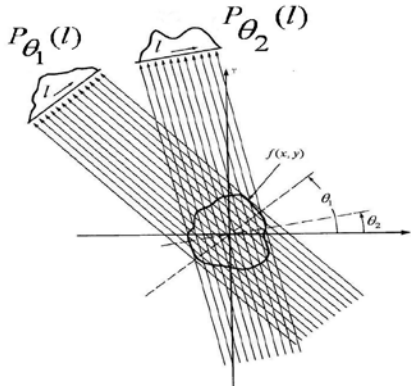
Figure 2.2 Parallel projections are taken by measuring a set of parallel rays for a number of different angles. [75]

A projection $P_\theta(l)$ is formed by combining a set of line integrals. The simplest projection is a collection of parallel ray integrals as is given by $P_\theta(l)$ for a constant θ. This is known as a parallel projection and is shown in Figure 2.2. It could be measured, for example, by moving a source and detector along parallel lines on opposite sides of an object or by keeping the source and detector fixed opposite to each other and rotating the object along a suitable axis or by moving the object either along a fixed vertical/horizontal plane.
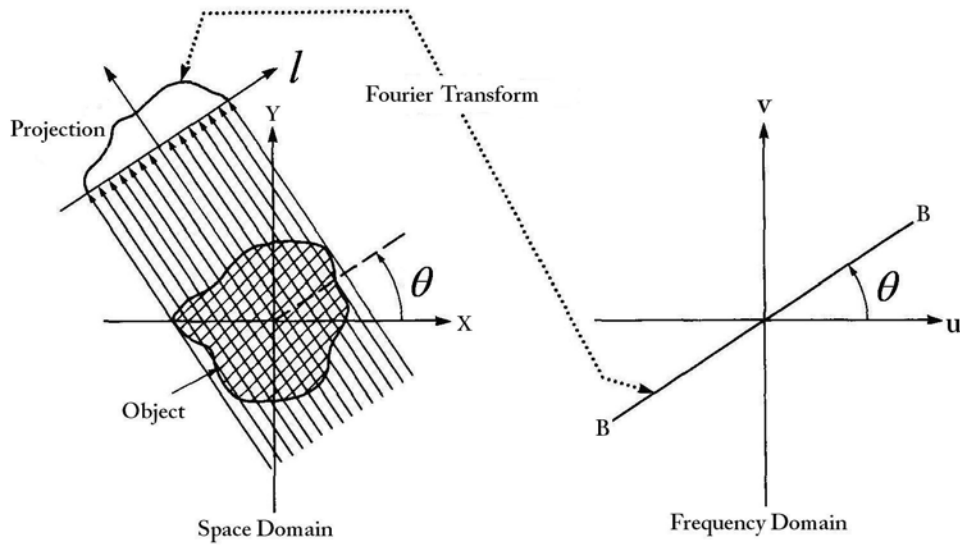
Figure 2.3 The Fourier slice theorem relates the Fourier transform of a projection to the Fourier transform of the object along a parallel line. [75]

When an object is illuminated with a planar wave in two-dimensional space as shown in Figure 2.3, the Fourier transformation of the transmitted wave or parallel projection measured on the line l is proportional to the two dimensional transformation of the object function along a semi-circular arc in the object frequency space. This is known as the Fourier slice theorem. Essentially this means that if one measures the projection data for attenuation at all angles; the Fourier transform of this data will reconstruct a 3D image of the local attenuation. Let us consider two dimensional Fourier transform of object function as [75],

$$F(u,v) = \int_{-\infty}^{\infty} \int_{-\infty}^{\infty} f(x,y)\exp\left[-2\pi i\left(ux + vy\right)\right]dx\,dy \tag{2.4}$$

.

The Fourier transform of the projection $P_\theta(l)$ at an angle θ is,

$$S_\theta(w) = \int_{-\infty}^{\infty} P_\theta(l) \exp[-2\pi iwl] dl$$

(2.5)

.

Let us consider $\theta = 0$ and v=0 one can write equation (2.4) as [75],

$$F(u,0) = \int_{-\infty}^{\infty} \left[\int_{-\infty}^{\infty} f(x,y) dy \right] \exp[-2\pi iux] dx$$

(2.6)

.

From the definition of parallel projection,

$$P_{\theta=0}(x) = \int_{-\infty}^{\infty} f(x,y) dy.$$

(2.7)

Plugging in the above in equation(2.6) [75],

$$F(u,0) = \int_{-\infty}^{\infty} P_{\theta=0}(x) \exp[-2\pi iux] dx$$

(2.8)

.

Therefore,

$$F(u,0) = S_{\theta=0}(u) \,. \tag{2.9}$$

This is the simplest form of Fourier slice theorem. This result is independent of the orientation between the object and the coordinate system. The Fourier transform of a parallel projection of an object $f(x,y)$ taken at an angle θ gives a slice of the two dimensional transform, $F(u,v)$, subtending an angle θ with the u axis. Simply, the Fourier transforms of $P_\theta(l)$ gives the values of $F(u,v)$ along the line BB in Figure 2.3. The relationship between the *(l,s)* coordinate system and *(x,y)* coordinate system can be given as [75],

$$\begin{bmatrix} l \\ s \end{bmatrix} = \begin{bmatrix} \cos\theta & \sin\theta \\ -\sin\theta & \cos\theta \end{bmatrix} \begin{bmatrix} x \\ y \end{bmatrix}. \tag{2.10}$$

In the (*l*,s) coordinate system the projection along *l* is,

$$p_\theta(l) = \int\limits_{-\infty}^{\infty} f(l,s) ds \,. \tag{2.11}$$

Fourier transform of equation (2.11) is,

$$S_\theta(w) = \int\limits_{-\infty}^{\infty} P_\theta(l) \exp\left[-2\pi i w l\right] dl \,. \tag{2.12}$$

.

Using equation (2.10), the above result can be written as [75],

$$S_\theta(w) = \int\limits_{-\infty}^{\infty} \int\limits_{-\infty}^{\infty} f(x, y) \exp\left[-2\pi i w \left(x\cos\theta + y\sin\theta\right)\right] dx\, dy \qquad (2.13)$$

Therefore,

$$S_\theta(w) = F(w,\theta) = F(w\cos\theta, w\sin\theta) \qquad (2.14)$$

The object function is the inverse Fourier transform of $F(u,v)$ [75],

$$f(x, y) = \int\limits_{-\infty}^{\infty} \int\limits_{-\infty}^{\infty} F(u,v) \exp\left[2\pi i \left(ux + vy\right)\right] du\, dv \qquad (2.15)$$

The image of the object function is reconstructed by filtered back-projection algorithm. Equation (2.15) is the expression of object function using the Fourier slice theorem. Replacing the rectangular coordinate system in the frequency domain (u,v) to the polar coordinate system (w,θ) by the following transformation [75],

$$u = w\cos\theta \qquad (2.16)$$

$$v = w\sin\theta \qquad (2.17)$$

$$du\, dv = w\, dw\, d\theta \qquad (2.18)$$

In the polar coordinate system, the object function could be expressed as described in [75],

$$f(x, y) = \int_0^{2\pi} \int_0^\infty F(w, \theta) \exp\left[2\pi wi\left(x\cos\theta + y\sin\theta\right)\right] w \ dw \ d\theta . \qquad (2.19)$$

$$f(x, y) = \int_0^\pi \int_0^\infty F(w, \theta) \exp\left[2\pi wi\left(x\cos\theta + y\sin\theta\right)\right] w \, dw \, d\theta$$
$$+ \int_0^\pi \int_0^\infty F(w, \theta + \pi) \exp\left[2\pi wi\left\{x\cos\left(\theta + \pi\right) + y\sin\left(\theta + \pi\right)\right\}\right] w \, dw \, d\theta . \qquad (2.20)$$

Again, it is known that,

$$F(w, \theta + \pi) = F(-w, \theta) . \qquad (2.21)$$

Equation (2.20) could be written as described in [75],

$$f(x, y) = \int_0^\pi \left[\int_{-\infty}^\infty F(w, \theta) |w| \exp\left[2\pi iwl\right] dw \right] d\theta . \qquad (2.22)$$

Here the following expression has been used [75],

$$l = x\cos\theta + y\sin\theta . \qquad (2.23)$$

From equation(2.13), $S_\theta(w) = F(w, \theta)$ .Therefore equation (2.22) can be written as described in

[75],

$$f(x, y) = \int_0^\pi \left[\int_{-\infty}^\infty S_\theta(w) |w| \exp\left[2\pi iwl\right] dw \right] d\theta . \qquad (2.24)$$

Equation (2.24) is the expression for reconstructed object function using Radon transformation and filtered back projection. The above expression reconstructs the object from the Fourier transform of the projection $S_\theta(w)$. The above integration is for a continuous function, but in practice the projection as well as its Fourier transform is not continuous; they are both discrete. Therefore, the integration is replaced by a summation with some finite variable. In the discrete summation form, the above expression can be written as,

$$f(x, y) = \sum_{\theta=0}^{\pi} \sum_{w=-l}^{l} S_\theta(w) |w| \exp\left[2\pi i w l\right]$$

(2.25)

.

In this dissertation, the reconstruction of images is performed using Matlab's, inbuilt code for the Radon transformation.

2.3   THz Computed Tomography Experimental Setup

All the experiments in this dissertation have been performed using a commercial THz-TDS system made by Picometrix Inc (T-Ray 2000®) as shown in Figure 1.2. In this section, the additional hardware, which is required to convert the T-Ray 2000 system to a THz-CT system, is described. A schematic of the rotational and translational components for CT scanning is shown in Figure 2.5. Samples are placed in the middle between the two Si-lenses for tomographic measurements. The sample is mounted to a translation stage enabling movement in both horizontal and vertical directions. The translational stage can be operated by the supplied software with the system. A rotating stage (Figure 2.4) has been developed in the lab to rotate the cork sample. As it is a tomographic measurement, rotation of the sample is very important. A Lab-view code has been developed to automate the rotational and translational stages altogether.
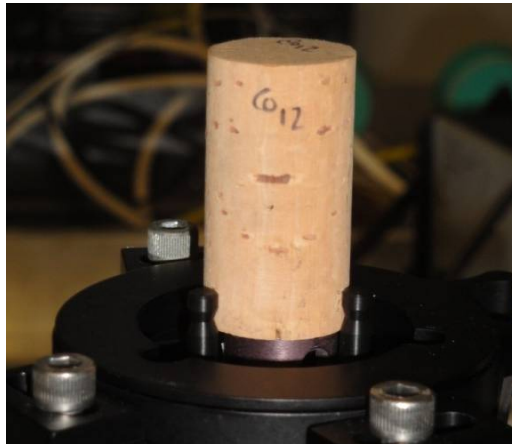
Figure 2.4 Photograph of a cork sample on a rotating holder.
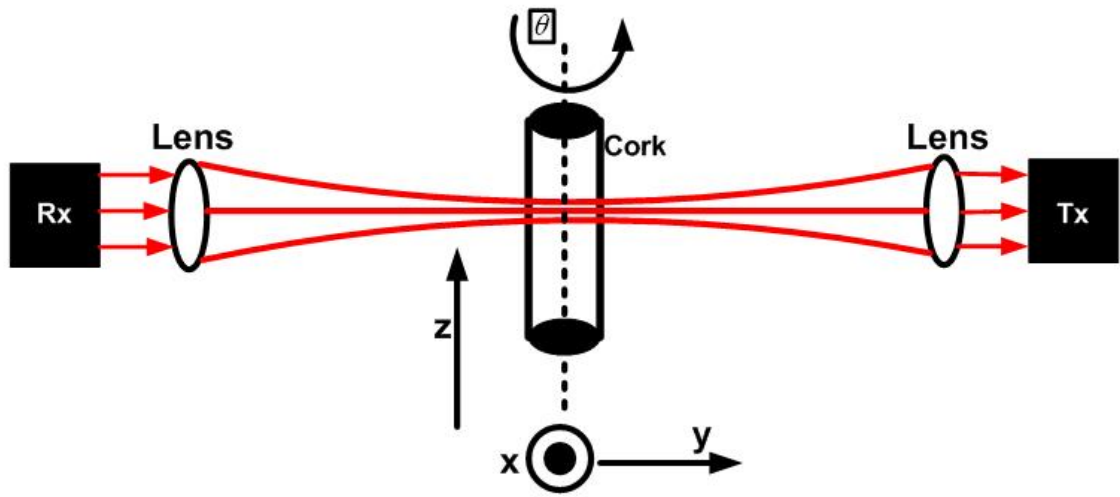
Figure 2.5 Schematic of the side view of the experimental set-up.
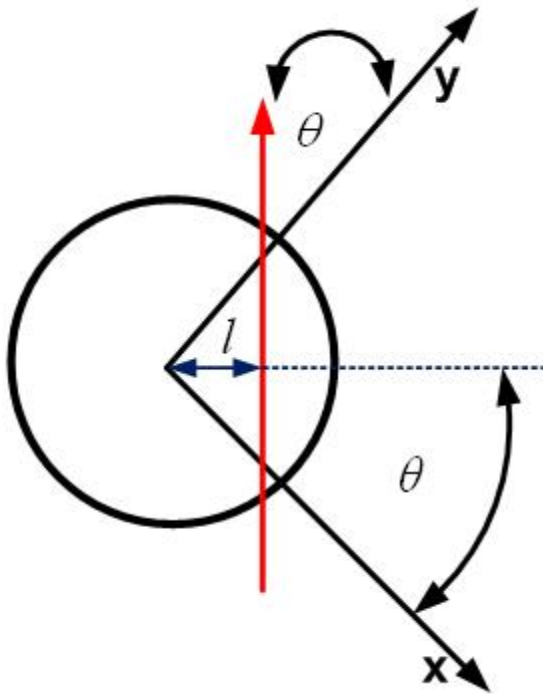
Figure 2.6 Schematic of the top section of the cork shows angle θ, distance l and propagation of THz ray.

For a complete 3D tomography image reconstruction, one need to acquire a transmission scan of the sample in the way shown in Figure 2.5. In Figure 2.5, the side view of the schematic is shown; the sample is placed at the focal point of the two silicon lenses so that the THz beam which is emitted from the transmitter (Tx) is focused in the region of the sample and enters the receiver (Rx) as a parallel beam after passing through the sample. The (x,y,z) axes are shown in the Figure 2.5, where the vertical line passing through center of the sample is the axis of rotation and the center of the coordinate system is located at the middle of the sample on the axis of rotation. A photograph of a cork sample on a holder is shown below Figure 2.4. The top view of the sample with rotation angles with (x, y) is shown in Figure 2.6. The red line is the direction of the THz beam in both figures. For simplicity, these figures neglect refraction of the THz beam as it passes through the sample. Referring to Figure 2.6, one can reconstruct the THz image in the x-y plane (at a fixed z position) by measuring the projection parameter $P_\theta(l)$ (Figure 2.1) for various l and θ values. The measured value $P_\theta(l)$ could be the attenuation of the THz radiation by the sample, the time delay of the THz pulse through the sample, or some other measureable quantity. In this work, attenuation is taken as the projection parameter $P_\theta(l)$. The average attenuation is measured between 0.1-0.2 THz frequency range to reconstruct images following radon transformation and filtered back-projection algorithm.

2.4 A review on Terahertz Computed Tomography (THz-CT)

After the advent of THz-CT, there has been considerable development in the field with instrumentation as well with the development of reconstruction algorithm. An excellent review article on methods of THz imaging can be found in the review article by S.Wang and X-C Zhang [16]. The authors have elaborately described different THz imaging modalities. A detail discussion about THz-CT, THz-DT, THz binary lens tomography and THz digital holography is discussed in that review article with some detailed mathematical discussion. In this chapter, selected aspects of THz-CT imaging are reviewed which were not included in the review by S.Wang and X-C Zhang [16].
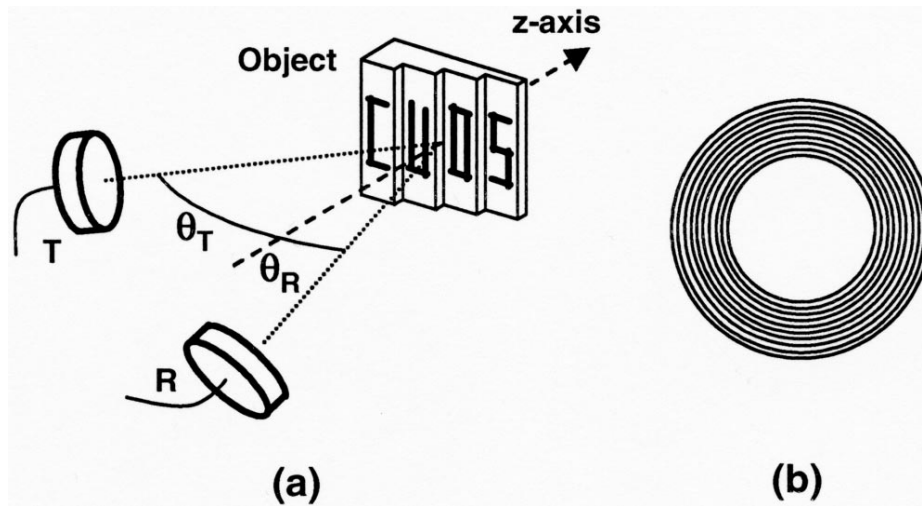
Figure 2.7 Experimental setup for time reversal imaging: (a) Reflection imaging configuration and (b) Annular synthetic aperture. The transmitter and receiver are labeled as ''*T*'' and ''*R*,'' respectively. [76]
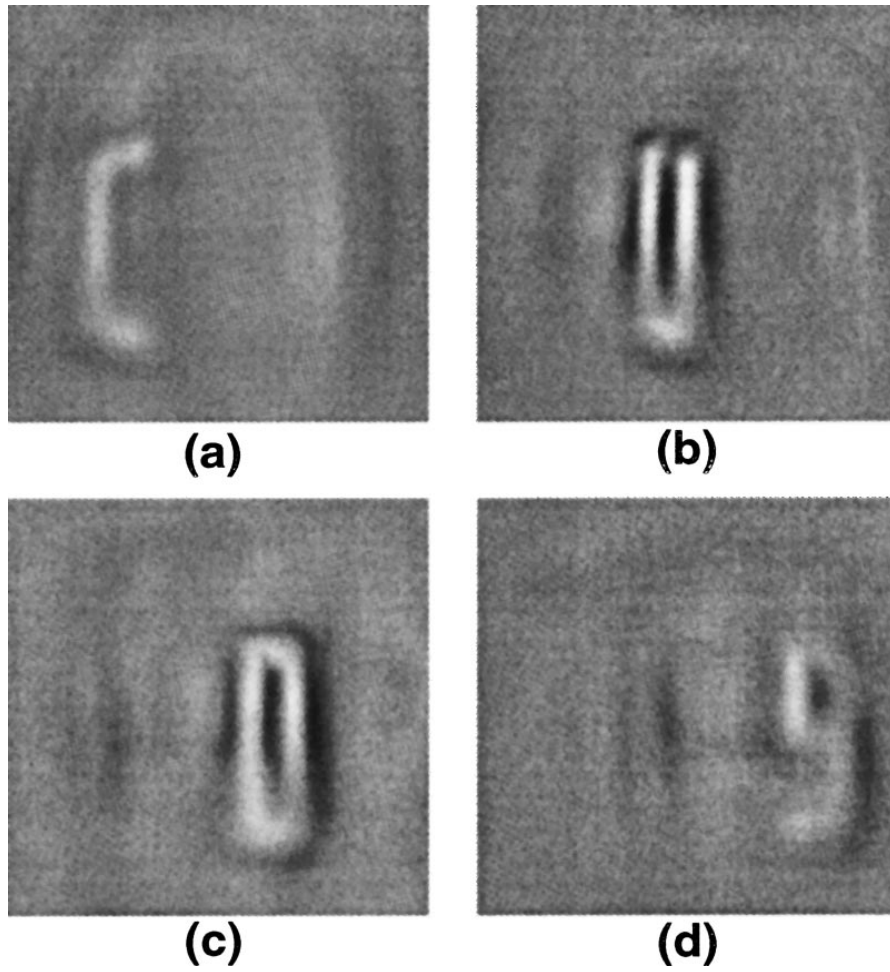
Figure 2.8 Reconstructed image planes for (a) ''C,'' (b) ''U,'' (c) ''O,'' and (d) ''S.'' [76]
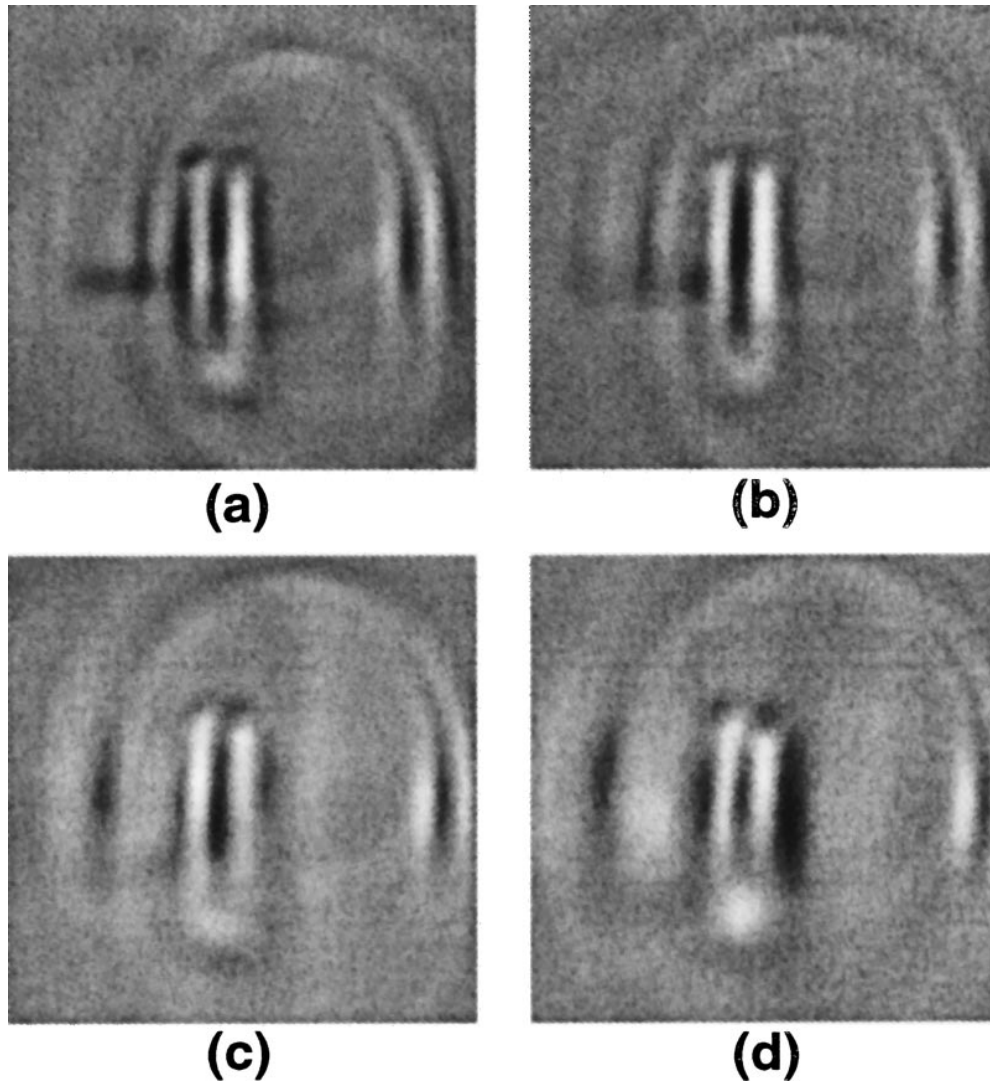
Figure 2.9 Reconstructed images of the letter ''U'' using a single ring with (a) NA=0.43, (b) NA=0.38, (c) NA=0.32, and (d) NA=0.27. NA stands for numerical aperture of the ring. [76]

T.Buma and T.B.Norris demonstrated 3D THz imaging using single cycle THz pulses [76]. Here authors demonstrated reflection mode imaging using single cycle THz pulses and applying time reversal reconstruction algorithm. The experimental set-up is shown in Figure 2.7 (a) and it consists of a fiber coupled transmitter and receiver module. The object to be scanned consists of aluminum foil letters spelling ''CUOS'' and it is attached to a high-density polyethylene substrate. Each letter is approximately 12 mm tall, 3 mm wide and with

a line width of 1-mm. The reconstructed images of letters "CUOS" are shown in Figure 2.8 (a,b,c and d). Figure 2.9 (a,b,c & d) show reconstructed images of the letter ''U'' from single rings with NA=0.43, 0.38, 0.32, and 0.27, respectively. The most striking features are the bright arcs sweeping across the images.

A.Brahm *et al.* demonstrated an all-electronic 3D computed THz tomography at operating frequencies of 230-320 GHz [77]. Authors used a plastic rod inside a foam tube (Figure 2.10). The scanning interval was 1 degree with a full 360-degree rotation. Visual image, sonogram and a reconstructed image of a slice are shown in Figure 2.10.
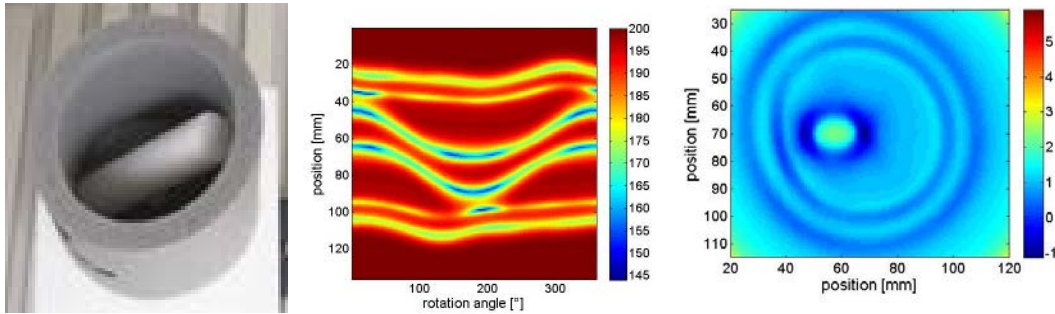
Figure 2.10 (Left) Sample of polymer foam with a plastic rod. (Middle) A Sinogram of a central sample layer. (Right) The reconstructed image of the Sinogram. Dark areas represent high absorption and define the edges of the sample. [77]

D.J.Roth *et al.* showed THz computed tomography of thermal protection system material [78]. Authors developed an axial computed tomography system for THz-TDS measurement.
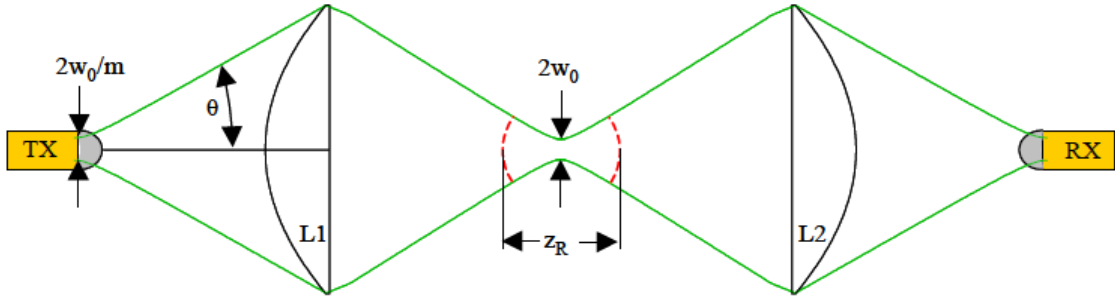
Figure 2.11 Sketch of confocal transmission CT-TD-THz transmitter receiver arrangement with lenses. [78]

A schematic of the CT-TD THz is shown in Figure 2.11. It consists of a Picometrix T-Ray 4000 control unit, TD-THz transmitter, receiver, lenses, T-Ray 4000 motion controller. Authors fabricated one sample 300 mm (Height) by 240 mm (Length) by 50.8 mm (Thickness) with flat bottom holes of different diameters in such a way that holes on each row has a constant diameter and holes on each column has constant depth. Another set of samples were prepared with voids in it as shown in Figure 2.12. Another sample consisted of SOFI corrugated foam sample with no apparent void but a lot of external texture. All samples were subjected to THz-CT scanning. The different THz-CT and X-Ray CT images are compared in the Figures 2.13 to 2.17.
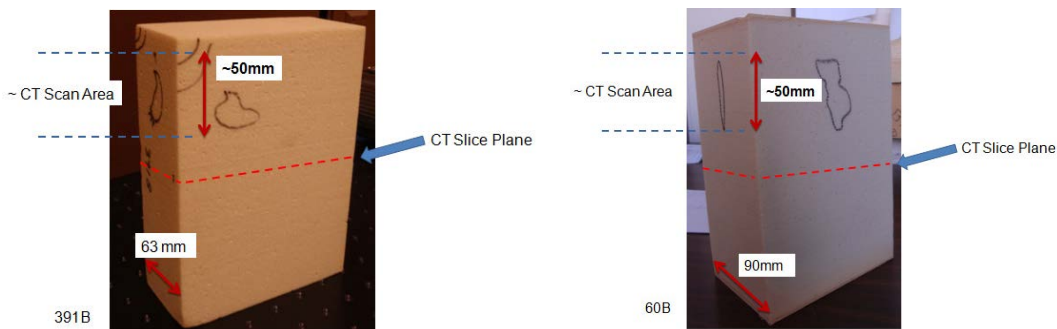
Figure 2.12 Samples with voids simulating naturally occurring voids. Black outlines show approximate position and morphology of the embedded void. [78]
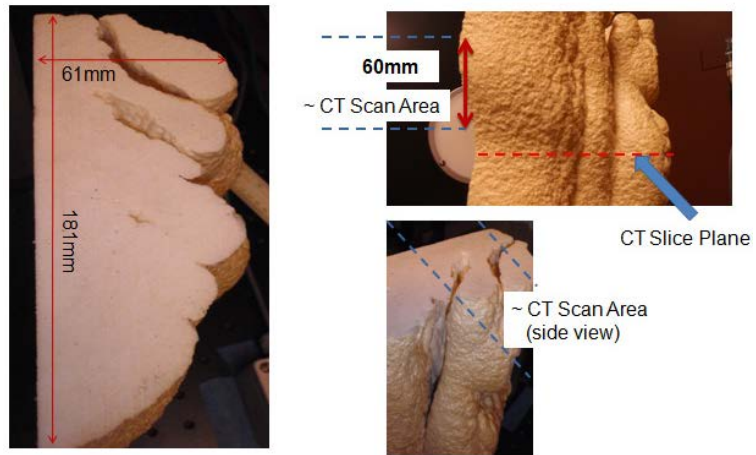
Figure 2.13 SOFI corrugated foam sample. [78]
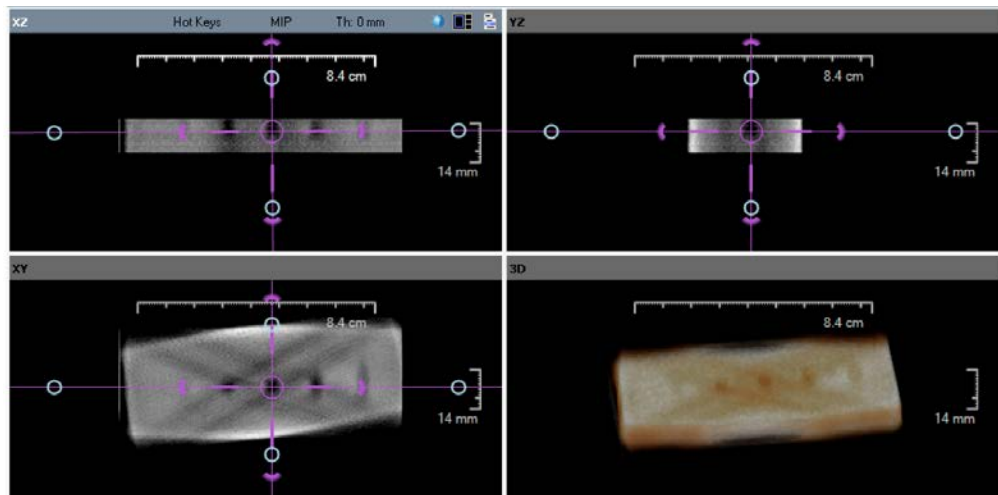
Figure 2.14 Top (XY), side views (XZ and YZ) and a semi-transparent volume rendering for a THz CT slice set for the row of flat bottom holes of diameter = 6.35 mm. X-like feature is CT reconstruction artifact. [78]
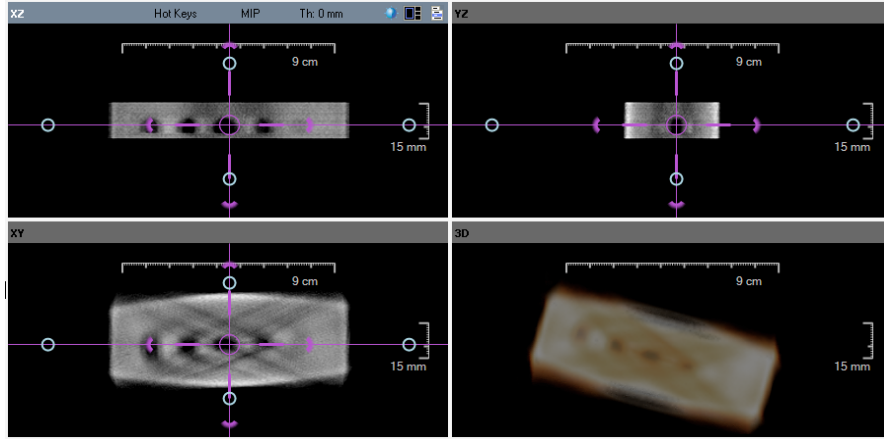
Figure 2.15 Top (XY), side views (XZ and YZ) and a semi-transparent volume rendering for a THz CT slice set for the row of flat bottom holes of diameter = 19.05 mm. X-like feature is CT reconstruction artifact. [78]
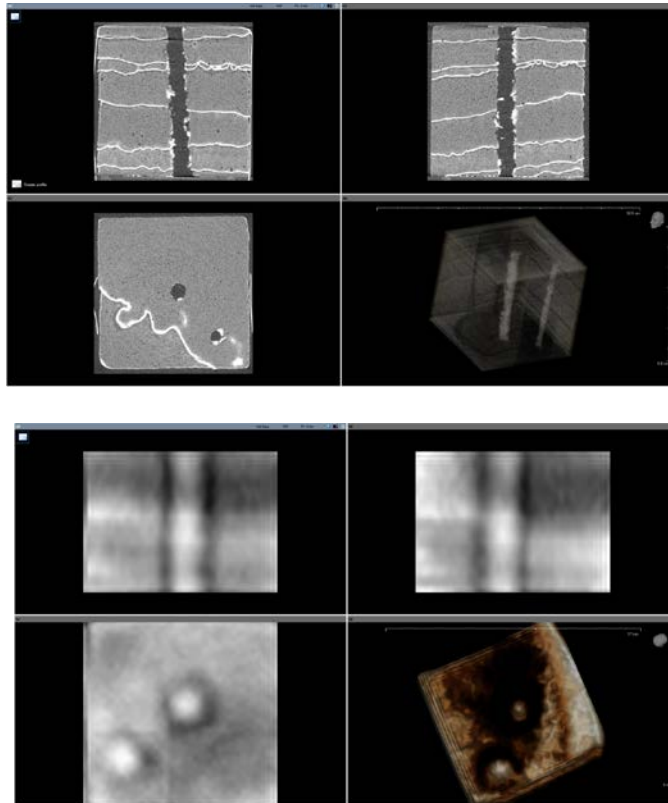
Figure 2.16 Top (XY), side views (XZ and YZ) and a semi-transparent volume rendering for a CT slice set for a section of the sample with drilled holes. [78]
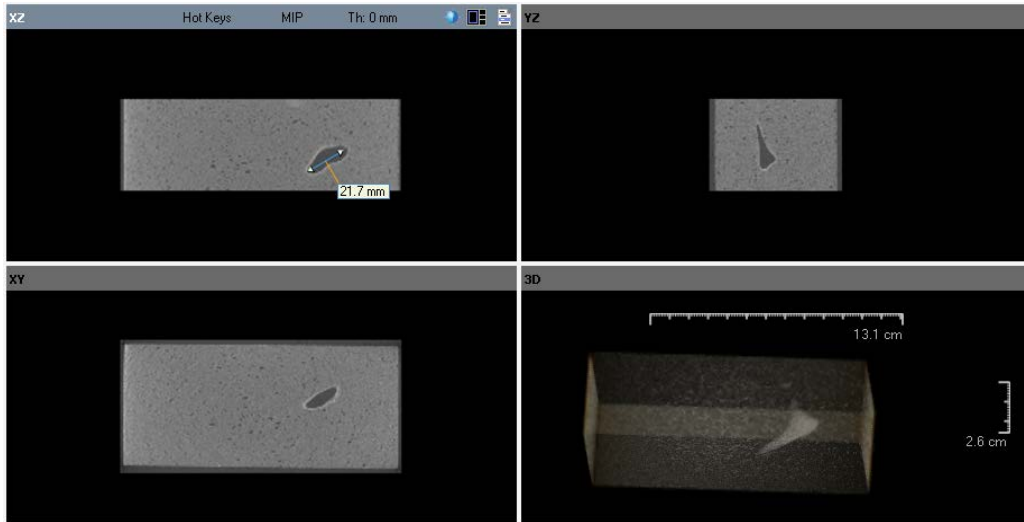
(a) X-Ray CT.
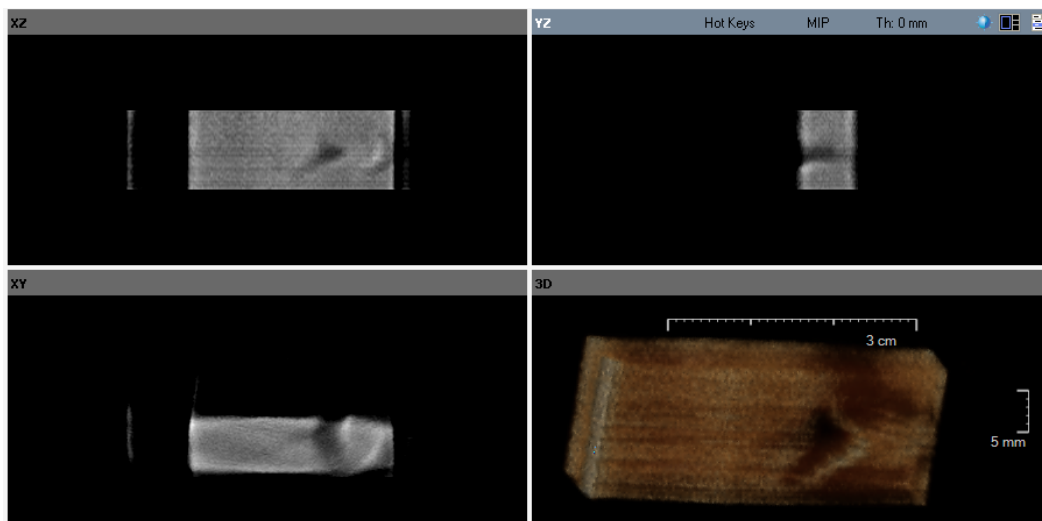
(b) THz CT.

Figure 2.17 Top (XY), side views (XZ and YZ) and a semi-transparent volume rendering for a CT slice set for a section of the sample 391B containing an embedded void. [78]

Wenfeng *et al.* recently, demonstrated continuous wave (cw) terahertz tomography with phase unwrapping [79]. A bulk of foam having 60 mm and 100 mm dimension and a U-

shaped groove of depth of 20 mm is used as the sample. Figure 2.18 (a) shows the experimental set-up and Figure 2.18 (b & c) shows the unwrapped phase map of the sample.

(a) (b) (c) (d)
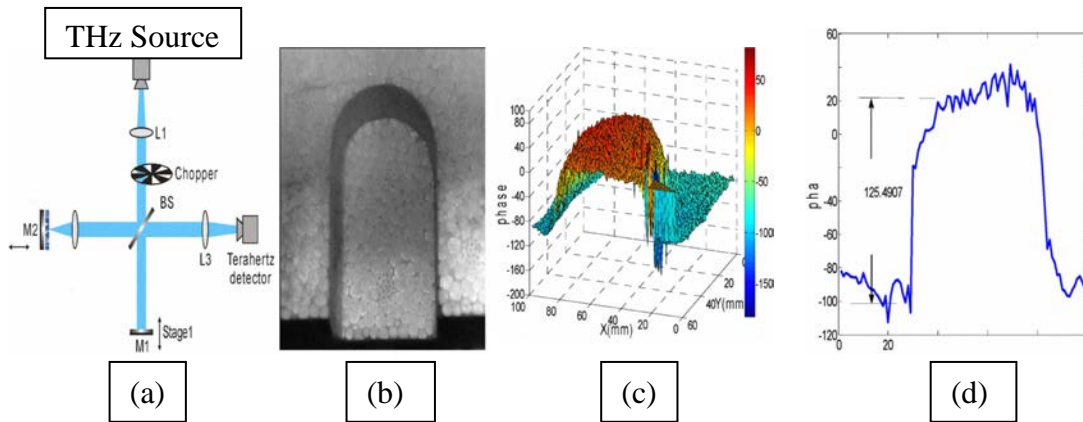
Figure 2.18 Experimental setup (a), LI, L2, L3, HOPE lenses; BS, silicon wafer; MI, M2, metallic mirrors; Stagel, Stage2, Stage3, computer- controlled linear stages. Picture of foam sample (b), unwrapped phase map restructured in 3D (c), and the curve of accurate phase abstracted from a line of the sample (d). [79]

(a) (b)
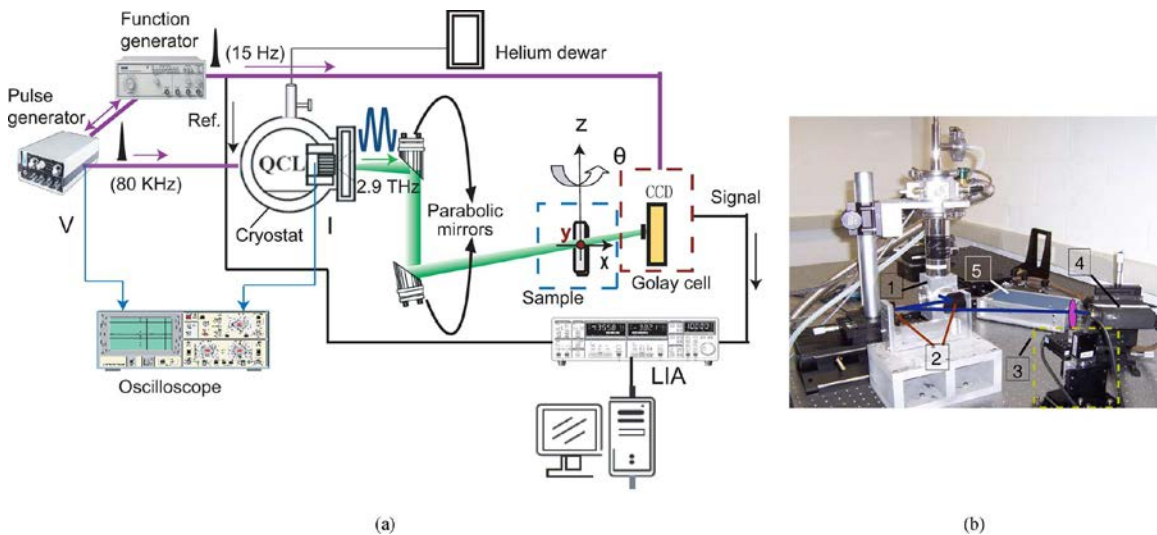
Figure 2.19 (a) Experimental apparatus for a terahertz QCL imaging system that is used to realize terahertz CT imaging. In practice, the sample is placed on a rotational stage for multiple view angles, which is mounted on a *xyz* linear stage to (continued to next page)

perform 3-D scanning. (b) The photograph of a part of the terahertz QCL imaging system. The numbers in the text-boxes from 1 to 5 indicate, respectively, a QCL that is mounted on the cold finger of a continuous-flow helium-cooled cryostat, a pair of parabolic mirrors, the rotational stage mounted on an *xyz* translational stage, a Golay cell detector, and a detector controller. [80]

(a)   (b)   (c)
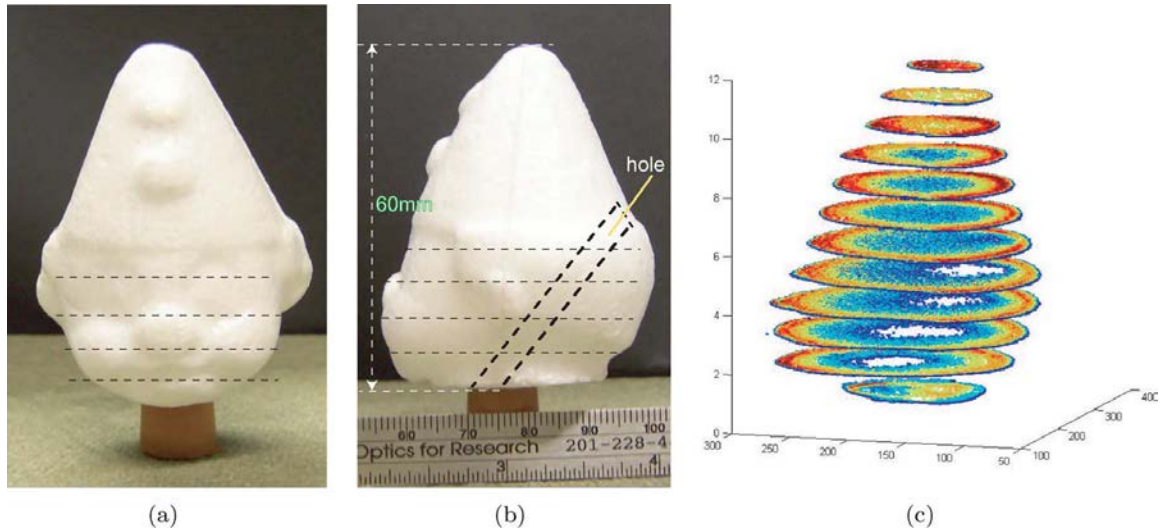
Figure 2.20 (a) The photograph of a nested structure of a polystyrene clown's head with hole inside. (b) The photograph of the side face of the polystyrene clown's head. (c) The reconstructed slices are stacked to recover the nested structure of the target object with a hole inside. The lines in (a) and (b) indicate the current four sliced heights for LCT in the hole area of interest. [80]

Xiaoxia *et al.* demonstrated 3D-THz-CT using a quantum cascade laser (QCL) [80]. The experimental set-up used is shown in Figure 2.19. Figure 2.20 (a & b) shows the visual images of a nested structure of polystyrene clown's head with hole inside and Figure 2.20 (c) is the reconstructed image of the same. The image was generated in 12 different slices with a 5 mm interval.
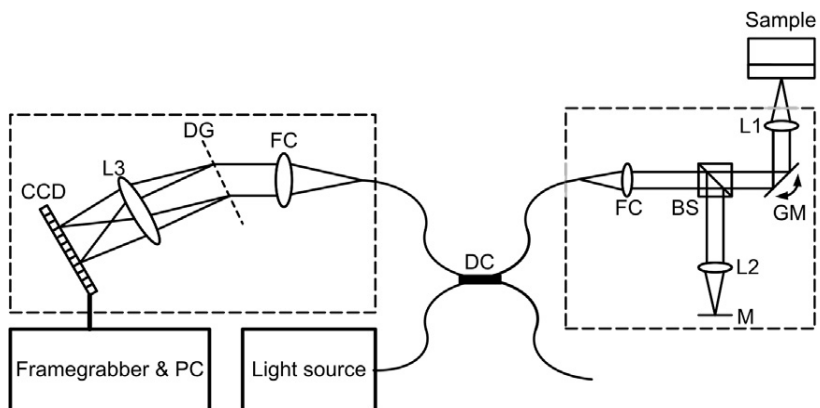
Figure 2.21 Schematic of the spectral-domain OCT system. The dashed boxes represent portable and independent modules. DC – directional coupler; FC – fiber coupler; BS – beamsplitter; (G)M – (galvanometer) mirror; LX – lens; DG – diffraction grating. [81]
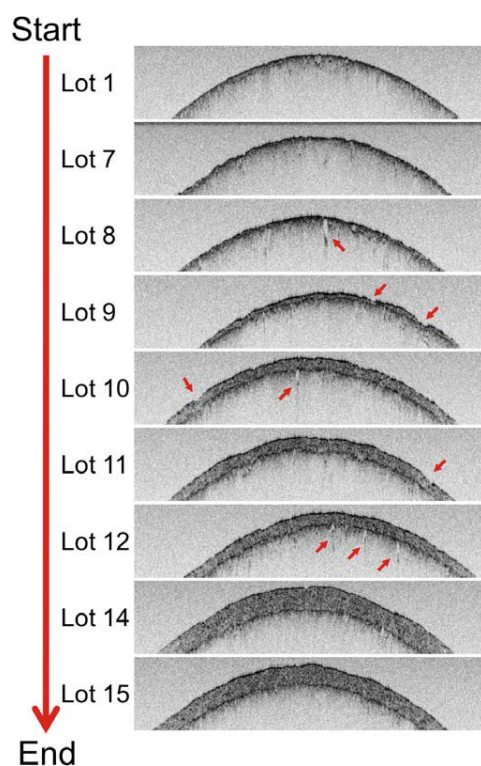
Figure 2.22 SD-OCT B-Scan images of tablets from different stages of the coating process. The image size is (4.3x0.36) mm^2 (in air) with a resolution of 4.3 μm and <4 μm in lateral and axial direction, respectively. [81]
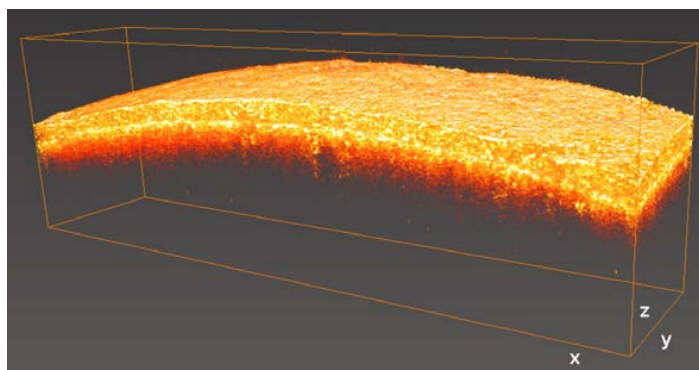
Figure 2.23 3D reconstruction of the coating from a tablet of Lot 12. Image size: x–y–z: (5 x 0.96 x 0.5) mm^3. [81]

D.M.Koller *et al.* studied non-destructive analysis of tablet coatings by optical coherence tomography [81]. Schematic diagram of the experimental set-up is shown in Figure 2.21. Figure 2.22 shows the OCT images of tablets (top-bottom) according to the progress of the coating process. Lot 1 is a non-coated tablet and lot 15 is a fully coated tablet. Figure 2.23 shows the 3D reconstructed image of a tablet from lot 12.

Vlasenko Maxim *et al.* [82] demonstrated tomography using high-power terahertz free electron laser. Experimental set-up and two tomographic images at different wavelengths are shown in Figure 2.24. In this experiment, a monochromatic free electron laser, which generates 100-ps pulse of continuous radiation having a repetition rate of 5.6 MHz, was used.
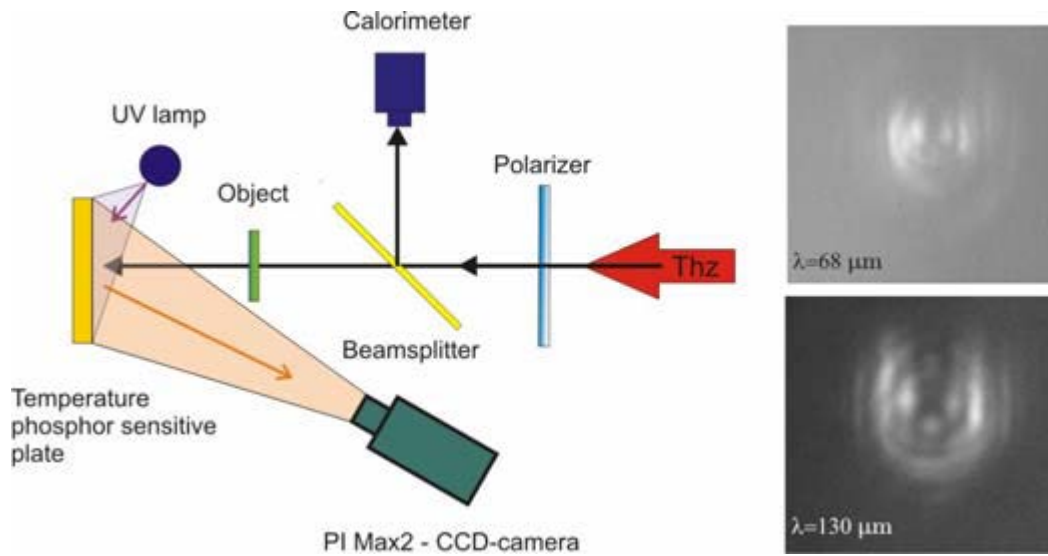
Figure 2.24 Schematic of experimental set-up and experimental results. [82]

$$n(z) = n \exp(-z/D^*)$$
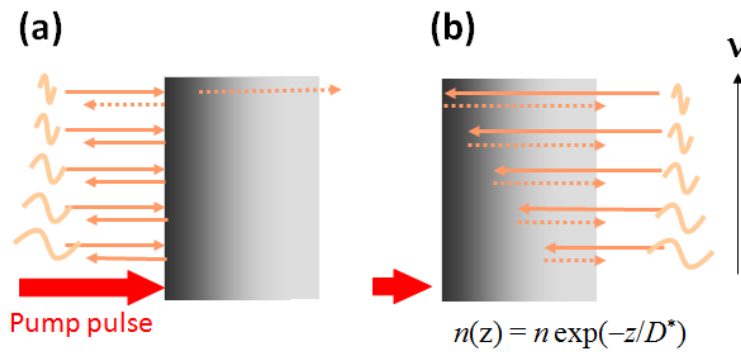
Figure 2.25 Schematic of (a) co-propagation and (b) counter-propagation geometries. Vertical axis shows the frequency of the THz probe pulse. [83]
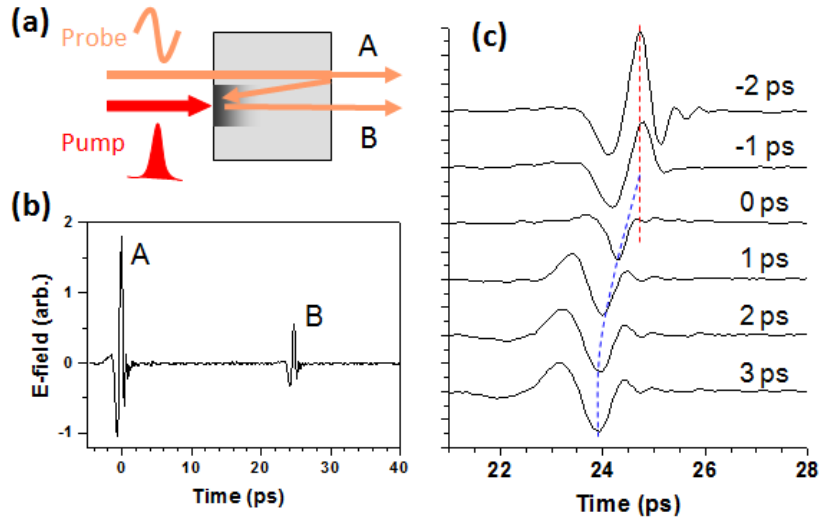
Figure 2.26 (a) Schematic of the pulse propagation and detection in the authors method. (b) Example of the THz waveform transmitted from the Si wafer. (c) Pump-probe delay time dependence of Pulse B when the Si wafer was excited by the optical pump with the energy density of 360 µJ/cm2. Insert values show the pump-probe delay times. Dashed lines indicate the equivalent phase position of the reflected pulses. [83]

Masaaki *et al.* [83] proposed THz tomography of photo-induced carriers based on optical-pump THz-probe reflection spectroscopy with the counter-propagated pump and probe pulses. Authors introduced a co-propagating geometry in the optical pump THz probe reflection spectroscopy. In this method, when the frequency of the THz wave is close to the plasma frequency of the photo excited surface of the material, the THz wave goes through the surface and interact with the material and when it reflects back from the other surface, it provides valuable information about the carrier dynamics. Figure 2.25 shows both co-propagation and counter propagation geometry. Figure 2.26 (a) shows the schematic diagram of the method, authors adopted for counter propagation geometry. At first, the input surface is irradiated with both THz pulse and optical pulse. The later generates free carriers near the surface. After reaching the back surface, the THz pulse splits into two parts, one the direct pulse A and the other internal reflection pulse B. Pulse B again is reflected from the input

surface and is detected at the output after pulse A at the opposite surface. Figure 2.26 (b) shows the THz pulse used by the authors. Figure 2.26 (c) shows the pump-probe delay time dependence of the THz waveform transmitted excited by the optical pump with an energy density of 360 $\mu J/cm^2$. The delay time of 0 ps corresponds to the time that the reflected THz pulse (Pulse B) overlaps the pump pulse at the input surface.

Qi Li *et al.* demonstrated THz-CT using CW gas laser operated at 2.25 THz [67]. Figure 2.27 shows the experimental set-up for the THz CW-CT. Figure 2.28 shows the visual images of the sample at different directions and Figure 2.29 shows the reconstructed images of the same sample by BFP, SART and MSART algorithm, respectively. Details of the mathematical procedure of the algorithms are discussed in the paper.
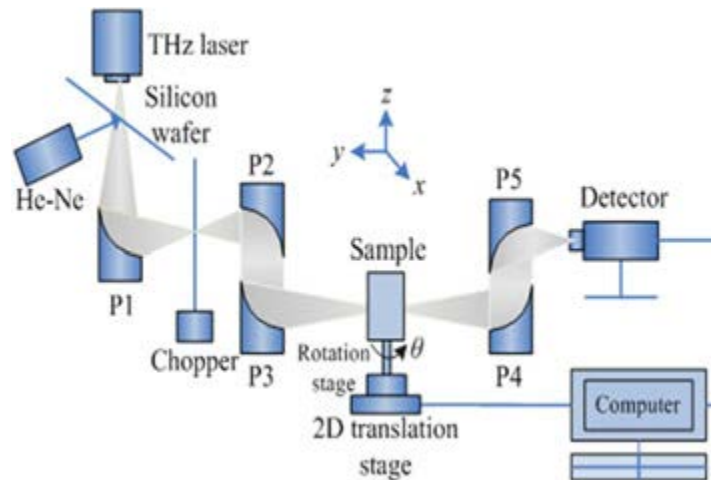
Figure 2.27 Experimental set-up of CW THz-CT. [67]

Figure 2.28 Photographs of the sample used for THz-CT reconstruction (in four different directions). [67]
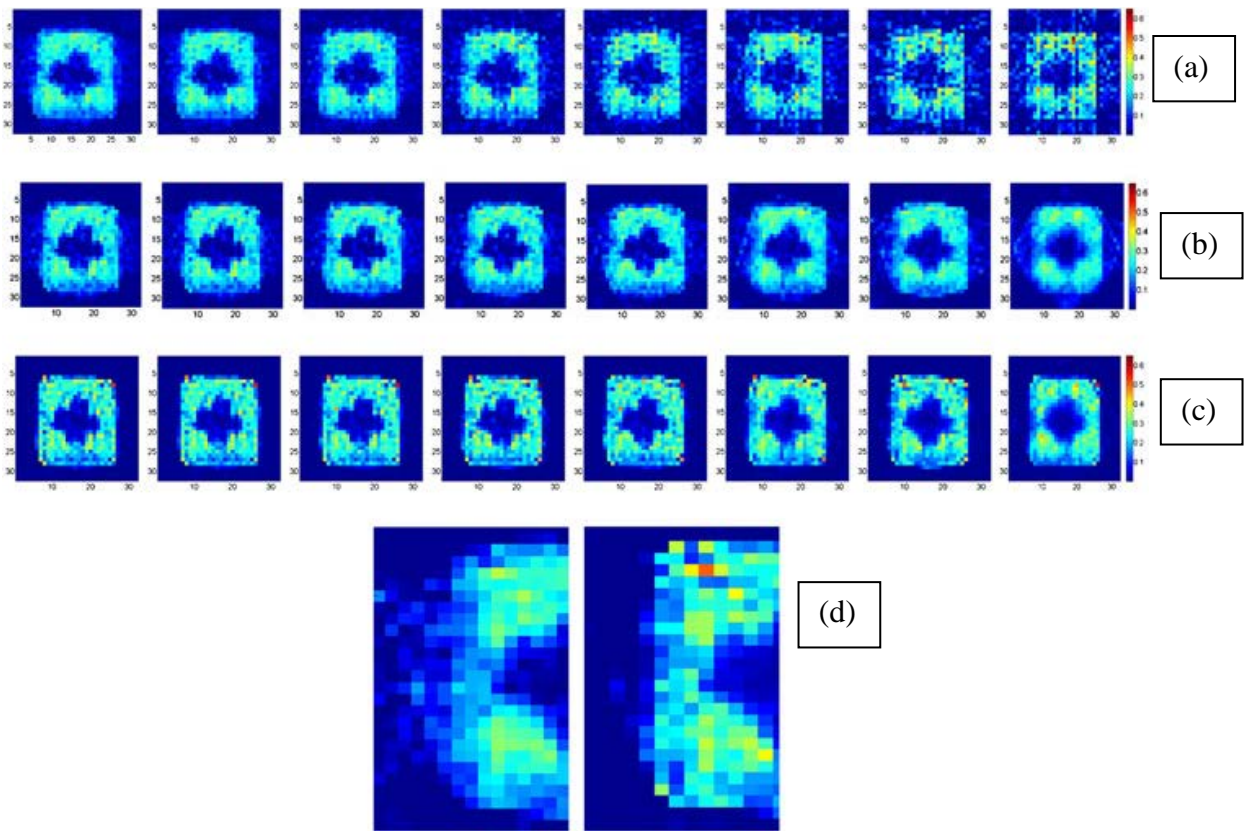
Figure 2.29 Reconstructed images using: (a)BFP (ramp filter), (b)SART, (c)MSART and (d) local images of SART and MSART as N 09. Images (a,b,c) from (Continued next page) left to right correspond to the following number of rotations N=90, N=45, N=30, N=18, N=15, N=10, N=9 and N=6 respectively. [67]

Lee *et al.* demonstrated THz optical coherence tomography based on quantum cascade lasers [84]. The quantum cascade lasers (QCLs) used operated in the frequency

range between 2.08-2.4 THz. Details of the figures and description of the experimental results are given in the next page.
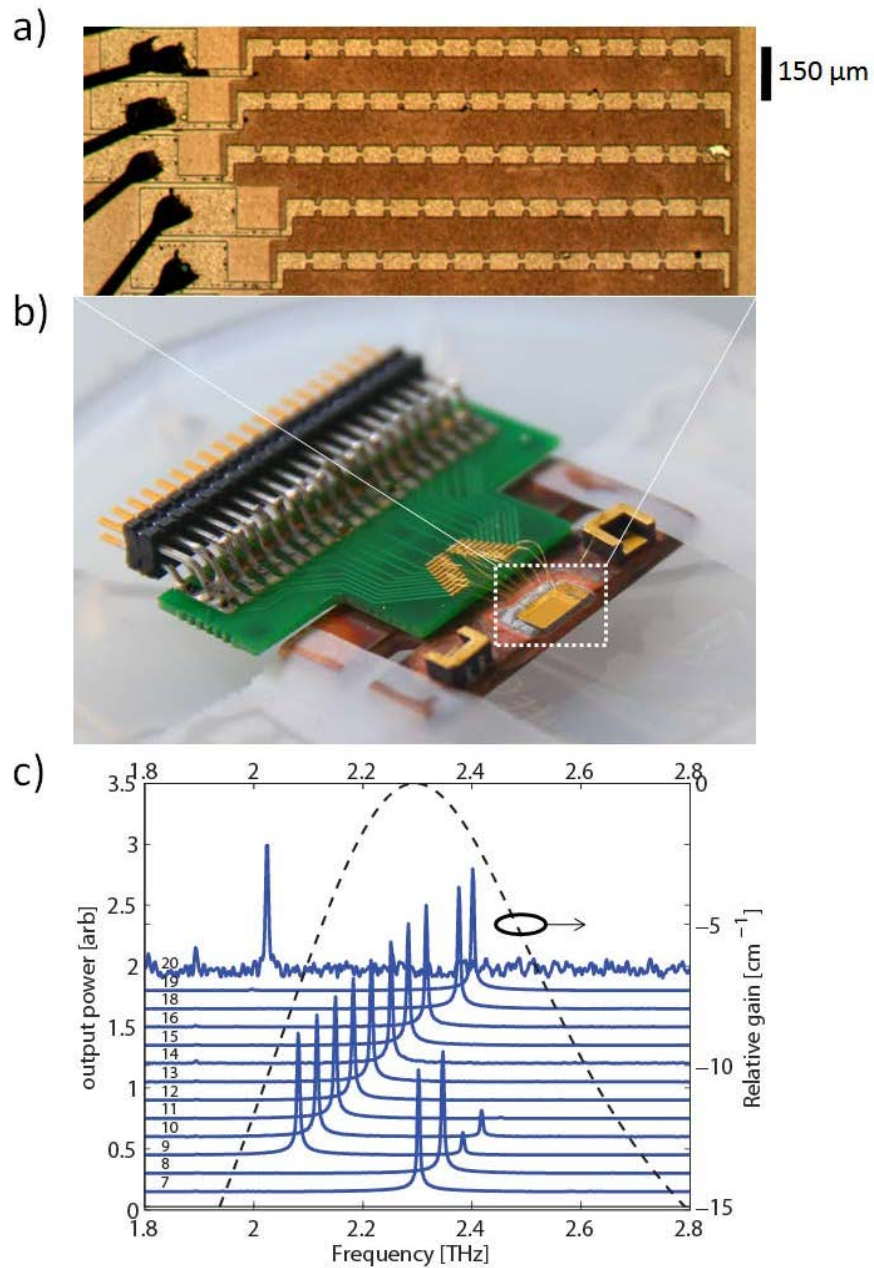
Figure 2.30 (a) Enlarged image of the 21-element 3rd order distributed feedback grating QCL array with system packaged in part (b). (c) shows spectra of QCLs in array (devices numbered at left) showing frequency separation~30 GHz. Devices 9 through 19 show frequency coverage of 320 GHz. Dashed line indicates measured gain bandwidth of the QCL active region. [84]
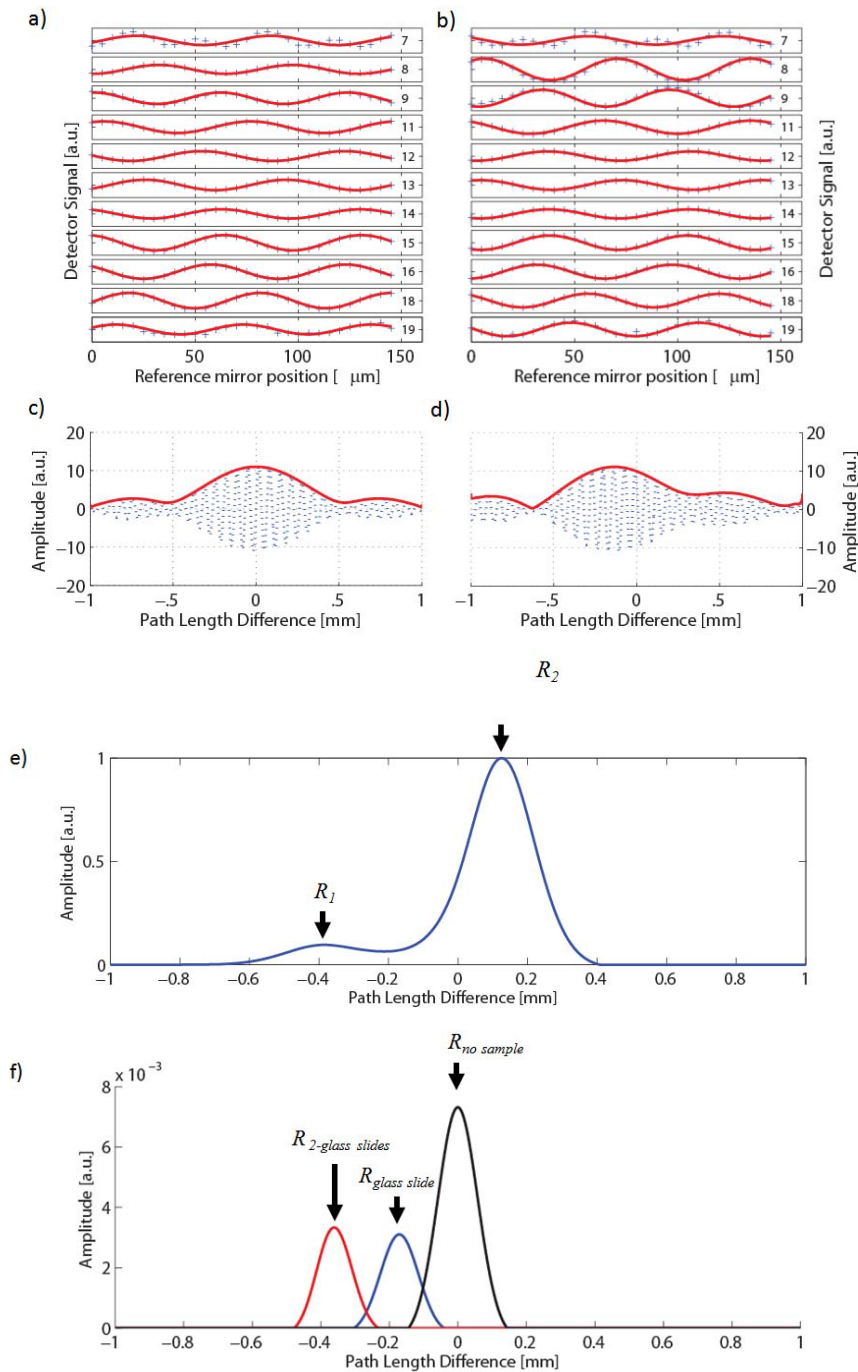
Figure 2.31 (a) shows interference signals (blue '+') and numerical fit (red solid trace) for various QCL devices as a function of position of the reference mirror. (b) Shows the same interference signals with a 380-μm thick dielectric sample inserted. (c) and (d) show the summation of normalized measured signals (blue dashed trace, envelope in red solid trace) without and with the sample, respectively. (e) shows the de-convolved signal using (c) as the kernel for the signal. (d) A large mirror/dielectric interface (arrow) and smaller dielectric/air interface (arrow) are apparent. (f) Shows the de-convolved results (Continued to next page)

for three separate scans: without a sample (*i.e.*, a mirror, black trace); with a 180-µm thick slide cover (blue) ; and with two 180-µm thick slide covers (red). The results correctly predict the axial depth of the interfaces, as well as the lower reflectivity of the glass slides. [84]

Maryelle *et al.* investigated THz-3D-CT of dried human bones [85]. The authors generated THz-3D-CT images of lumbar vertebra, a coxal bone, and a skull and made direct comparison with X-Ray 3D-CT images. Although THz has lower resolution than X-Ray but it was evident from their measurement that THz-3D-CT images can actually distinguish between compact bones and spongy bones. Figure 2.32, Figure 2.33 and Figure 2.34 are the comparison of the images of different bones reported by the authors. Radiograph is the X-Ray 3D tomographic image.
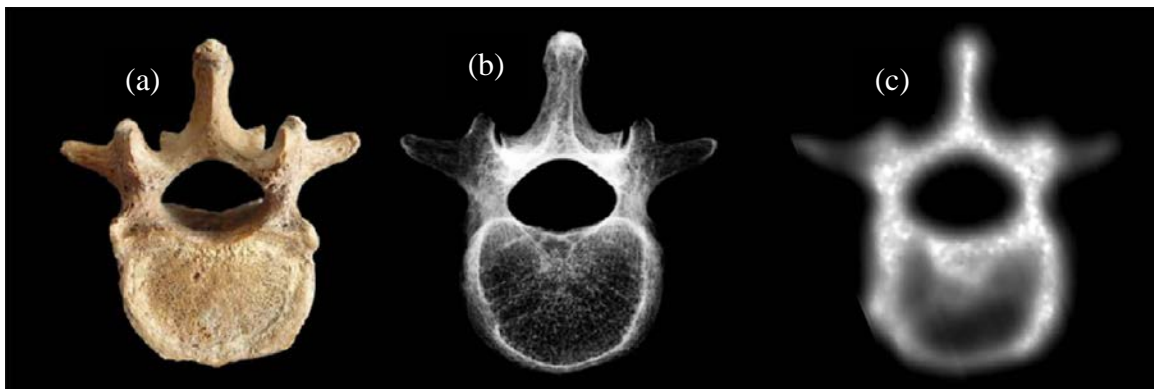
Figure 2.32 Human lumbar vertebra (superior view). (a) Photograph. (b) Radiograph. (c) THz imaging. [85]
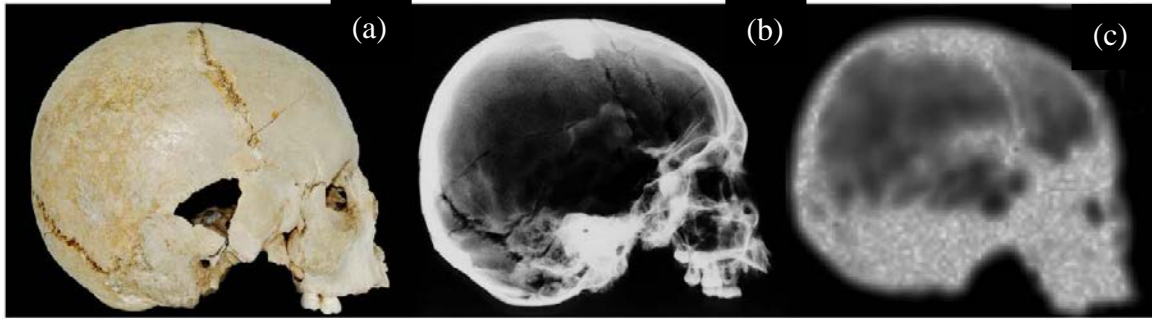
Figure 2.33 Human skull (right lateral view). (a) Photograph. (b) Radiograph. (c) THz imaging. The red arrows indicate the location of the coronal suture. [85]
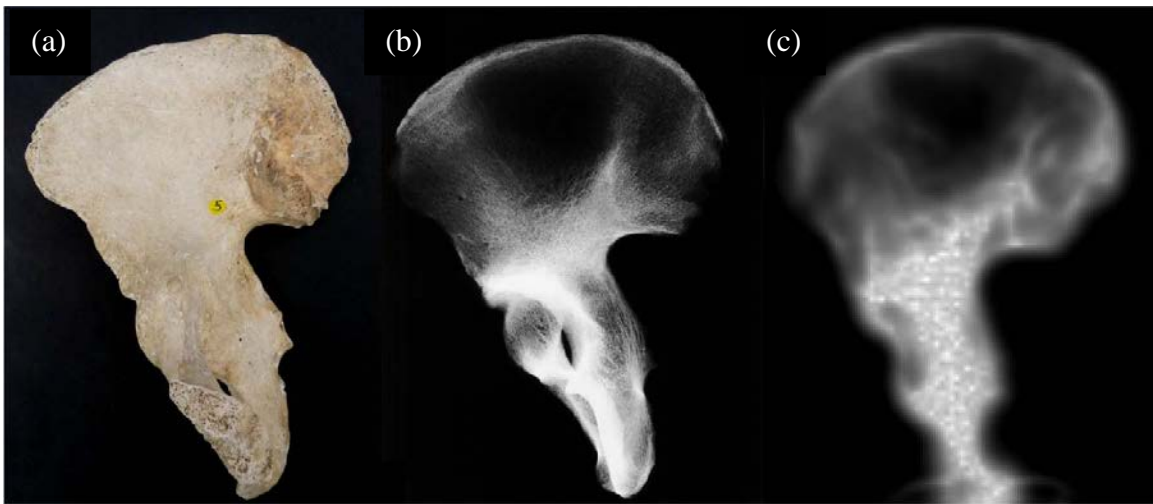
Figure 2.34 Right human coxal bone. (a) Photograph. (b) Radiograph. (c) THz imaging. [85]

All the examples above are the THz-CT reconstructed images of materials having lower refractive index (foams, low-density plastic, dried bones etc) and thus the refraction is not that serious when T-Ray travels through them. But when THz rays travels through high density plastic (refractive index of 1.54), the THz- beam refracts heavily inside the material and as a result steering of beam occurs which gives anomalous attenuation and thus contributes boundary effect phenomena in a major way. The motivation of this dissertation is

to eliminate that boundary effect phenomenon by considering Fresnel reflection and beam steering.

CHAPTER 3

BOUNDARY EFFECT PHENOMENA AND DEVELOPMENT OF ALGORITHM

3.1   Introduction

Despite the common approach of both X-Ray and THz computed tomography, there are some major distinctions in applying computed tomography in the two different spectral regions. Due to the longer wavelength of THz radiation, the effects of diffraction are much more prevalent than with X-Ray radiation. X-Ray, due to its nature, travels through the target material in almost straight lines without much refraction as shown in Figure 3.1 (a). Due to the refractive index change at material boundaries, THz waves are susceptible to refraction as well as loss of signal due to Fresnel reflection from boundaries as shown in Figure 3.1 (b). Due to the enhanced loss of THz power at a boundary due to both Fresnel reflection losses as well as refractive losses, reconstructed THz–CT images exhibit enhanced attenuation at the boundaries and a distortion of the boundary shapes. It is called a boundary effect phenomena. Because of this boundary effect, when a THz-CT image is generated by the Radon transformation, one can notice enhanced attenuation at the boundary of any reconstructed image. Examples of the boundary effect can be seen in many papers on THz CT imaging [16, 18, 64, 69, 71, 86, 87]. Only in the case of a low refractive index contrast material can the refractive and reflective effects be ignored in the image reconstruction [32].

For NDE of materials for which the internal structure is not uniform, the boundary effect can mask the subtle but important contrast in a sample's internal structure. In the previous study mentioned of internal defects in natural cork [69], pulsed THz-CT was used to reconstruct the cork's internal structure. However, the strong boundary artifact

inhibits resolution of the mass density variations, cracks, voids, and channels of the cork

structure. For natural cork, it is the internal structure which is thought to determine the

gas diffusion properties of natural cork which are essential for the functionality of natural

cork as barrier to gas and liquid diffusion [88, 89]. The application of THz-CT to natural

cork will be discussed in Section 4.4.
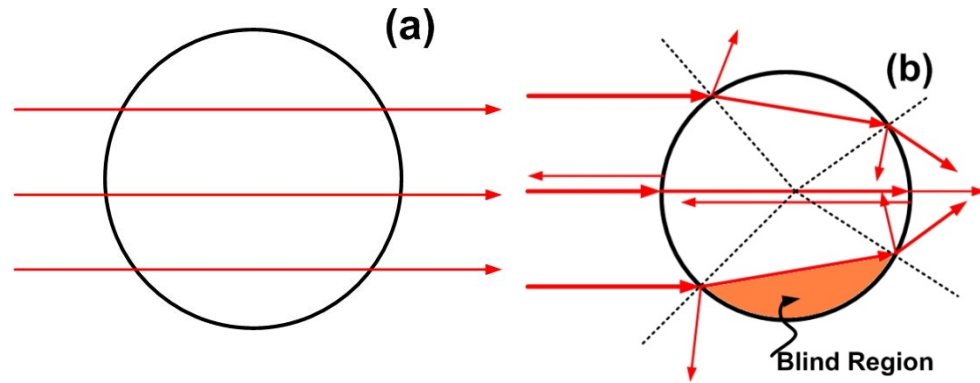
Figure 3.1 (a) Transmission of X-Rays through circular cross section of cork or plastic. (b) Transmission of THz beam through circular cross section of cork or plastic.
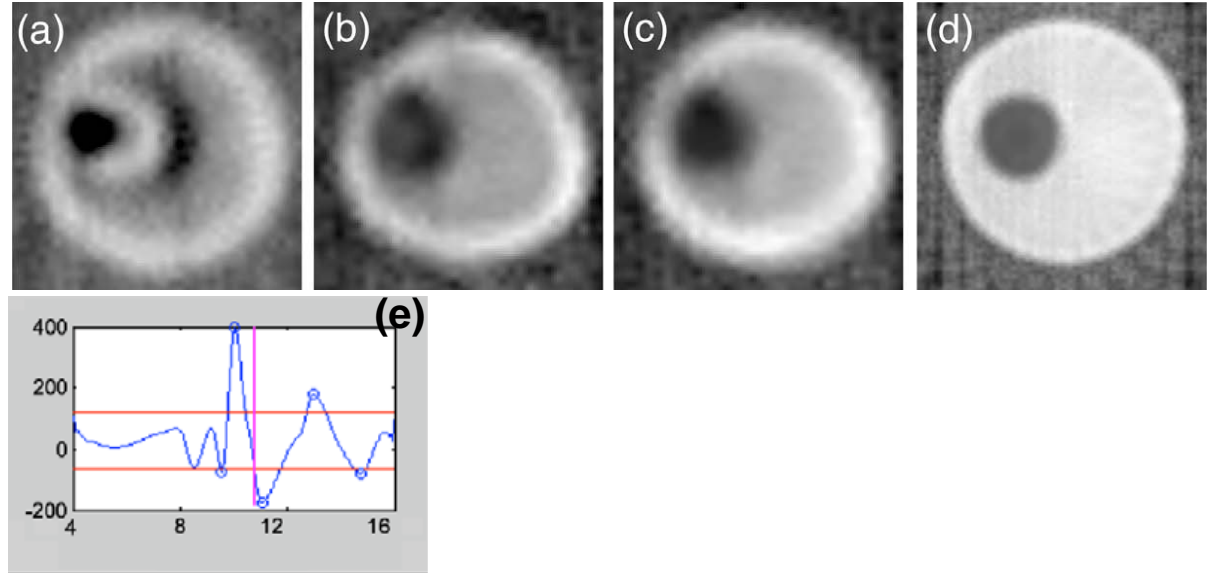
Figure 3.2 Ten millimeters diameter Teflon cylinder with off-axis 3.4 mm cylindrical hole: (a) amplitude cross-section from the THz main pulse amplitude, (b) time cross-section from the THz main pulse time delay, (c) time cross-section from the multi-peak averaging, and (d) time cross-section from theoretical values (thickness variations of the target). (e) THz waveform for $x = -1.4$ mm with thresholds (horizontal red lines) and calculated mean time delay (vertical purple line). [90]

Clearly, the vastly different spatial scales of x-rays and Terahertz radiation suggest that the reconstruction methodologies which are routinely employed in the x-ray range may not be optimal in the THz range. For example, incorporating the Gaussian beam properties of THz radiation in the image reconstruction process improves the quality of the reconstructed images [91]. A small number of papers have studied the boundary artifact phenomenon and have tried to remove it by different methodologies. E. Abraham *et al.* introduced a multi-peak averaging method to eliminate boundary effect due to refraction losses of the THz beam inside the material [90]. As the THz beam propagates through the material, it suffers refraction inside the material and thus produces multiple peaks - instead of a single peak - when it passes through a material [90] as

shown in Figure 3.2 (e). In this work, time delay from a particular peak is used to generate tomographic images. However, the presence of multiple peaks makes it difficult to choose the correct peak for time delay measurement. By averaging several of the peaks and considering the time delay of that averaged peak, the boundary effect is reduced. In applying this technique to 3D THz-CT images of a Teflon (refractive index 1.37) cylinder with a hole on it, the effect of the boundaries is reduced, but the boundaries are still visible in the reconstructed image [90] as shown in Figure 3.2 (a,b,c & d). In this chapter, it will be shown that, by correcting for the two most dominant phenomena (*i.e.,* steering of the THz beam and Fresnel reflection) prior to image reconstruction, the boundary effect can be essentially eliminated.

While an accurate reconstruction of an object with arbitrary shape and composition by THz CT is problematic due to the refraction artifacts, THz CT can still be an effective NDE tool if the general shape of an object under test is known. If one knows the shape and refractive index of a 'standardized' object, in principle the effects of Fresnel reflection and refraction could be removed from CT projection data prior to applying an inverse Radon transformation to reconstruct the image. By removing the boundary artifacts, the discrimination of internal structure of a test object compared to the ideal 'standardized' object could be greatly improved. For the specific example of NDE of cylindrically shaped natural cork stoppers, the outer size and shape of each sample is essentially the same. Removing the boundary artifacts enables a more detailed reconstruction of each sample's internal structure, which is very critical to the functionary of the stoppers with regards to their gas and liquid diffusion properties.

In this chapter, a methodology of removing boundary artifacts in THz CT imaging for cylindrically shaped objects is introduced. The mathematical algorithm for correcting CT projections prior to image reconstruction is described. The algorithm corrects for the loss of THz power due to Fresnel reflection at the boundary as well as the steering of the THz beam through the sample due to refraction. Most importantly, the loss of THz power through the collection optics of the THz detection system is corrected.

While the longer-term goal is to apply the developed algorithms to NDE of cylindrical cork stoppers, the non-homogeneous internal structure of cork and significant sample-to-sample variations clearly precludes natural cork as a model material for the development of correction algorithms. In order to study the boundary effect and develop algorithms for removing them from THz-CT reconstructed images, several cylindrically shaped plastic Plexiglas rods (real refractive index 1.54) are used as target material. Cylindrically shaped plastic rods provide a uniform, homogeneous material for development of boundary correction algorithms. Four identical plastic rods were chosen for the study. One of them is kept intact. In two of the samples, a uniform cylindrical shape hole (1mm and 5mm) is drilled near the geometric center of the cylinder. In the fourth sample, a cylindrically shaped hole is drilled near the periphery of the sample.

The Plexiglas rod samples are scanned in transmission using a Picometrix T-Ray 2000 system. Details of the experimental set-up have been discussed Section 2.3. For the tomographic scanning, samples are attached to a rotation stage such that the geometric center of the cylinder is nominally collinear with the rotation axis of the stage. Each sample is rotated in 2-degree intervals from zero to 360 degree (up to 180 rotations) relative to its original position. Full tomographic scanning is obtained by vertically

(resolution 1mm) and horizontally (0.5mm resolution) scanning a sample at each rotational position.

From the THz time-domain spectra, the average attenuation between 0.1-0.2THz at each scan position is calculated. For each horizontal slice through circular cross-section of the cylinder at a fixed rotational angle, the array of attenuation data represents a projection[75, 92] through the sample. A typical projection for a solid Plexiglas rod is shown in Figure 3.3 (a). By measuring the projection array at each rotation angle, a 2D reconstruction of the slice can be generated using MATLAB's built in function for Radon transformation with filtered-back propagation. A typical reconstructed slice using the measured (uncorrected) projection arrays is shown in Figure 3.3 (b). A complete 3D reconstruction is achieved by stacking the reconstructed slices at each vertical position.
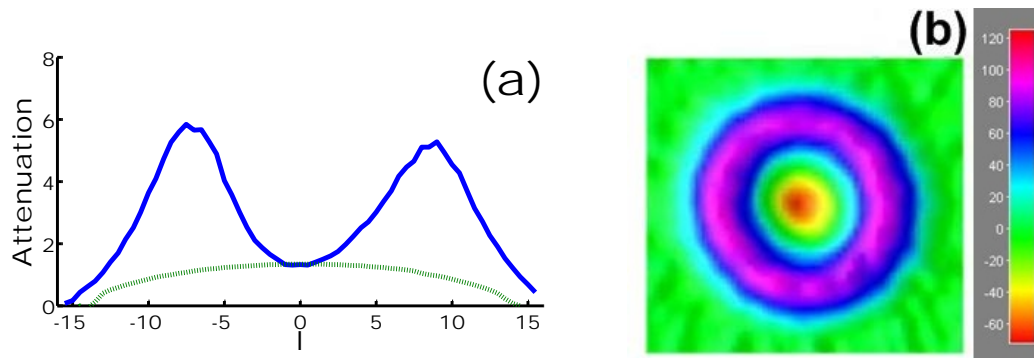
Figure 3.3 (a) Plot of experimentally measured average THz attenuation (solid) between 0.1-0.2THz and ideal theoretical attenuation (dashed) of a solid, uniform Plexiglas rod with no defect. (b) Reconstructed pulsed THz-CT image of a horizontal slice through Plexiglas rod.
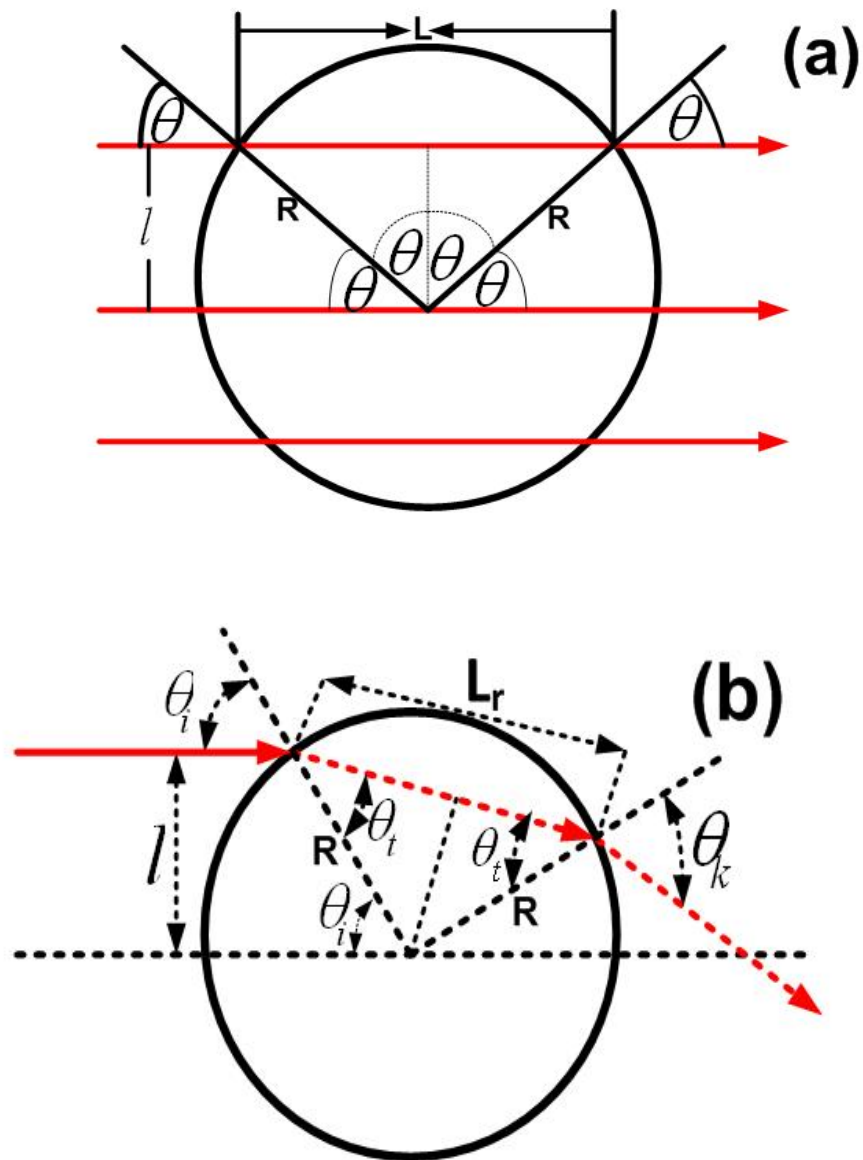
Figure 3.4 (a) Transmission of THz beam with no bending inside the material. (b) Transmission of THz beam with bending inside the material.

Figure 3.3 (a) shows a typical plot of the experimentally measured and ideal attenuation projection through a solid Plexiglas rod measured at 0.15 THz. The ideal projection data is calculated using measured values for the real refractive index and the

absorption coefficient of a homogenous sample. These values can be measured by propagating the THz beam through the diameter of the sample and analyzing the resulting frequency dependent phase and magnitude. The ideal projection assumes that the THz beam propagates straight through the sample as illustrated in Figure 3.4 (a).

For this ideal projection, the attenuation should depend only on the material's attenuation coefficient α_0 and the path length through the sample. The path through the sample depends on the offset distance l relative to the geometric of the circular cross-section.

$$A_{th}(l) = \alpha_o L(l) = \alpha_o 2R\sqrt{1 - l^2 / R^2} \quad . \tag{3.1}$$

According to Equation (3.1), the center position corresponding to $l = 0$ should exhibit the maximum attenuation with increasing attenuation as the offset parameter l increases away from the center diameter. However, in reality, the measured attenuation (Figure 3.3 (a)) is a minimum at the center position and increases as one moves away from the center axis with increasing l.

The experimentally measured attenuation projection includes Fresnel reflection losses from the boundaries as well as refraction of the beam (Figure 3.4 (b)). Note that the minimum measured attenuation in the sample (Figure 3.3 (a)) occurs when the THz beam propagates through the diameter of the sample. As the offset parameter l increases, the attenuation also increases. This increased attenuation is not due to a real attenuation of the material but rather results primarily from Fresnel reflection losses at the boundary as well as bending of the THz beam inside the Plexiglas rod. As will be illustrated below, the cylindrically shaped rod acts as a focusing element in the THz beam path. The presence of this focusing element steers the THz beam from its optimal path through the

remaining THz optical components resulting in an anomalously large attenuation since the deflected THz beam is no longer optimally focused on the THz detector. Clearly, the Fresnel losses and beam steering become increasingly severe as the THz beam propagates closer to the periphery of the sample. Consequently, the reconstructed 2D tomographic image of a horizontal slice through the rod shows an enhanced attenuation at the boundaries of the rod (Figure 3.3 (b)). Ideally, the reconstructed attenuation coefficient should be uniform throughout the material.

In this dissertation, an algorithm is developed that eliminates the effect of the Fresnel reflection and beam steering, so that the anomalous attenuation shown in the reconstructed image (Figure 3.3 (b)) can be removed. Essentially the goal is to develop algorithms to correct the measured attenuation curve of Figure 3.3 (a) to more closely approximate the theoretically predicted attenuation projection prior to reconstructing the image using Radon transformations.

3.2   Theoretical formulation of Fresnel losses

As a starting point, consider the refraction of a THz beam as it propagates through the circular cross-section of the rod as illustrated in Figure 3.1 (b). There are two obvious effects of refraction: (a) power reflection losses as the THz beam both enters and exits the sample (b) a change in the path length of the THz beam inside of the sample. Figure 3.4 (a) and Figure 3.4 (b) shows a pictorial depiction of THz beam transmitting through circular cross section of a cylindrical rod. In Figure 3.4 (a), bending of beam due to refraction is not considered but in Figure 3.4 (b), bending of beam is considered. From Figure 3.4 (b), the distance that the THz beam travels inside the material upon refraction clearly is not same as if the beam were to travel in a straight line. Using Snell's law of

refraction $n_a \sin \theta_i = n_p \sin \theta_p$ and the geometry of Figure 3.4 (b), it is straightforward to show that the length that the THz beam travels inside of the sample upon refraction is $L_r = 2R\sqrt{1 - n_a^2 l^2 / n_p^2 R^2}$, where n_a and n_p are refractive indices of air and plastic, respectively. Again from Figure 3.4 (a), the length that the THz beam travels inside the sample neglecting refraction is $L = 2\sqrt{R^2 - l^2}$. Considering the refractive indices of Plexiglas and air as 1.54 and 1 respectively an estimate could be given between L and L_r. If the ray travels at a distance $l = \dfrac{R}{2}$ from the center axis, $L = 1.73R$ and $L_r = 1.89R$. Therefore, a THz ray travels almost 10% more path length if bending of beam due to refraction is included.

The Fresnel reflection losses can be included using the power reflection coefficient [93],

$$
R = \left(\frac{n_t \cos \theta_i - n_i \cos \theta_t}{n_i \cos \theta_t + n_t \cos \theta_i} \right)^2 . \tag{3.2}
$$

Where n_i, n_t, θ_i and θ_t are refractive index of the incident medium, refractive index of the transmitted medium, incidence and transmitted angle, respectively and $\sin \theta = l / R$. For the experimental configuration mentioned by the authors, the polarization of the incident THz wave is parallel to the plane of incidence. Applying both Snell's law and Equation (3.2) to both the air-plastic and plastic-air interfaces gives the following reflection losses at the two boundaries,

$$R_{ap}(l) = \left(\frac{n_p \sqrt{1 - l^2 / R^2} - n_a \sqrt{1 - n_a{}^2 l^2 / n_p{}^2 R^2}}{n_a \sqrt{1 - n_a{}^2 l^2 / n_p{}^2 R^2} + n_p \sqrt{1 - l^2 / R^2}} \right)^2 \qquad (3.3)$$

and

$$R_{pa}(l) = \left(\frac{n_a \sqrt{1 - n_a{}^2 l^2 / n_p{}^2 R^2} - n_p \sqrt{1 - l^2 / R^2}}{n_p \sqrt{1 - l^2 / R^2} + n_a \sqrt{1 - n_a{}^2 l^2 / n_p{}^2 R^2}} \right)^2 \qquad (3.4)$$
.

The total transmission of a THz beam through the sample can be written as,

$$T(l) = (1 - R_{ap}) \exp(-\alpha L_r)(1 - R_{pa}) \qquad (3.5)$$

Where α is the power attenuation coefficient for the plastic. The first term of Equation (3.5) represents the power loss when the THz beam refracts as it enters the sample. The second term represents the attenuation loss of the THz beam propagating through the sample, while the third term represents the reflective power loss as the sample exits the sample. It should be noted that this loss term could be 100% if the THz beam is totally internally reflected at the plastic-air interface. Let us consider a beam travelling through the material at a distance $l = R / 2$ through the material. Considering the linear attenuation coefficient (α) as 0.0311/mm and R as 14mm, the transmission of the THz beam through the material can be written as 0.4144 and 0.4708 with and without

Fresnel loss, respectively. Therefore, the loss of the transmitted beam due to Fresnel reflection is typically around 14%.

3.3   Beam steering losses

While the increase in sample path length and Fresnel losses increase the attenuation from what one would expect for an un-deviated beam, the magnitude of these losses are too small to explain the rapid increase in attenuation observed in Figure 3.3 (a) as the offset (parameter l in Figure 3.3) of the THz beam relative to the geometric center of the cylindrical rod is increased. In the absence of the sample, the lenses and other optical components of the THz system are aligned to optimize the THz power from the THz transmitter to the detector. Clearly, the presence of any sample in the beam path becomes part of the optical system since refraction of the THz beam by the sample will steer the THz beam from its optimal path to the detector. As illustrated in Figure 3.5, when the cylindrical sample is off center in the THz optical system, the resulting beam steering will reduce the measured THz transmission.   A detail illustration of beam steering is depicted in Figure 3.5 (a, b, c & d). Figure 3.5 (a) shows all the beams are collimated and adjusted in such a way, that all the THz rays emerging from the transmitter are collected by the detector for optimal detection of THz power. Figure 3.5 (b) shows a cylindrical shaped object that is placed at the optical axis of the system in such way that the center of the cylindrical object coincides with the optical axis of the optical system. The cylindrical object acts as a lens and thus beam steering occurs resulting in some of the extreme rays missing the detector. Figure 3.5 (c) shows a situation where the cylindrical object is off centered. In this case, the center of the cylindrical object is placed above the optical axis of the system. Significant beam steering occurs in this case and very minimal amount of

THz beam hits the detector. A similar situation is illustrated in Figure 3.5 (d) where the center of the cylindrical object is placed below the optical axis of the system. Significant beam steering is observed in this case. Therefore, it is a fact that if the object moves away from the optical axis of the system, beam steering increases, less THz radiation hits the detector, and thus the measured attenuation increases.

This loss of beam due to beam steering contributes also to the anomalously high local attenuation coefficient in the final reconstructed CT image. To eliminate the steering effect in the said algorithm, one needs to theoretically predict the steering of beam through the THz optical components. In order to predict the effects of beam steering on the THz-CT system, a ray-tracing software program BEAM4 (https://www.stellarsoftware.com/) is used to model the optical system. A table of the optical components, their spatial locations, physical sizes which were used for the ray-tracing calculation are listed in Table 3.1. Using the geometric ray tracing software, a fan of rays is defined which emerges from the source. Their progression is traced through the optical components. The fan of rays simulates the THz beam as it propagates through the optical system. By counting the percentage of the rays, which propagate through the optical system to the detector as a function of the offset parameter l, one can estimate the transmission T_{st} of THz radiation. It is assumed that when $l = 0$, corresponding to optimal optical alignment, the transmission is 100%.

Table 3.1: Specifications of Optical Components for Ray-Tracing Calculation

Components	Distance from the source (mm)	Diameter (mm)	Refractive Index	Curvature of the Surface
Source	0	0.1		
First Lens	S1=76.2	38.5	1.5	0.05194/mm
Second Lens	S2=215.1	38.5	1.5	0.05194/mm
Scanned Object	S3=292.1	28	1.1	0.07142/mm
Third Lens	S4=368.3	38.5	1.5	0.05194/mm
Forth Lens	S5=571.5	38.5	1.5	0.05194/mm
Detector	S6=647.7	0.1		
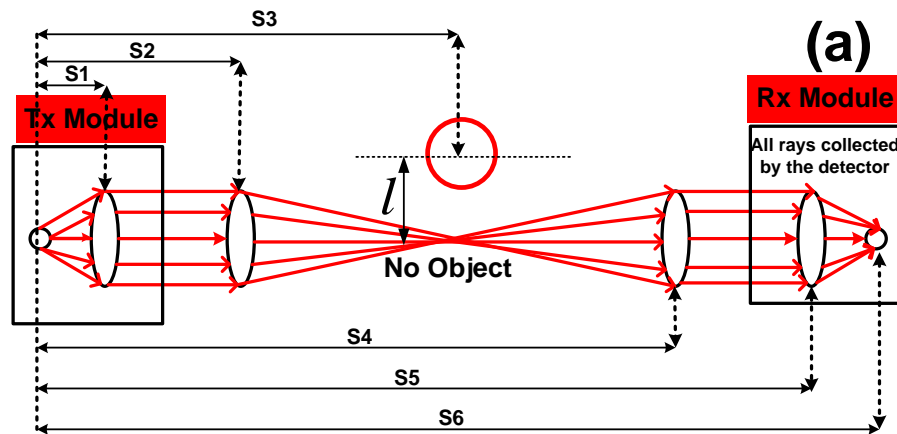
Figure 3.5 (a) Illustration of optimal propagation of the THz radiation through the collimating and focusing lenses in the absence of a sample.
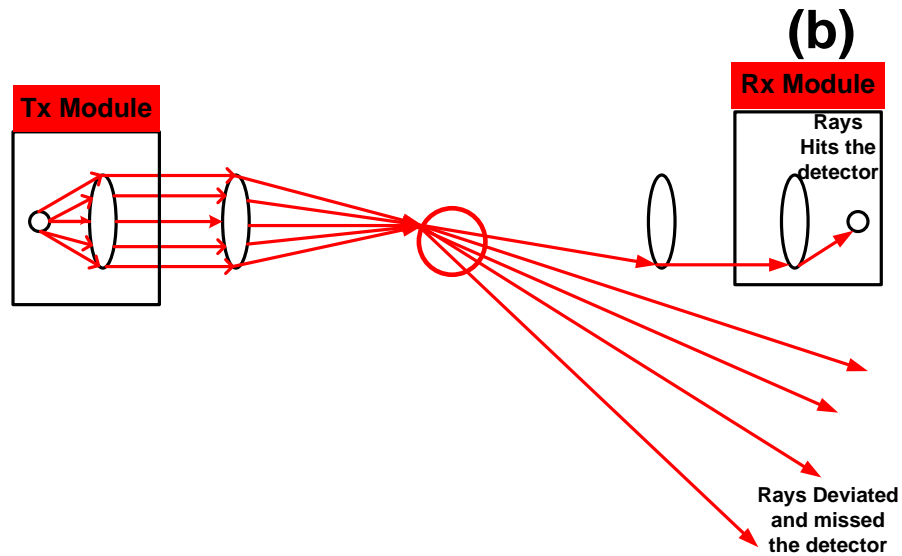
Figure 3.5 (b) Illustration of the beam steering of the THz radiation due to the refractive effects of the sample as an optical component in the system, when the sample is centered with optical axis of the system.
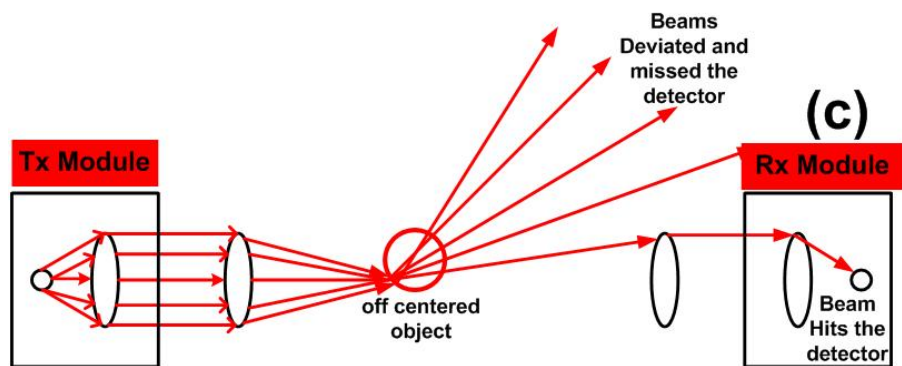
Figure 3.5 (c) Illustration of the beam steering of the THz radiation due to the refractive effects of the sample as an optical component in the system, when the sample is off centered (towards left when viewed on the direction of THz beam) with optical axis of the system.
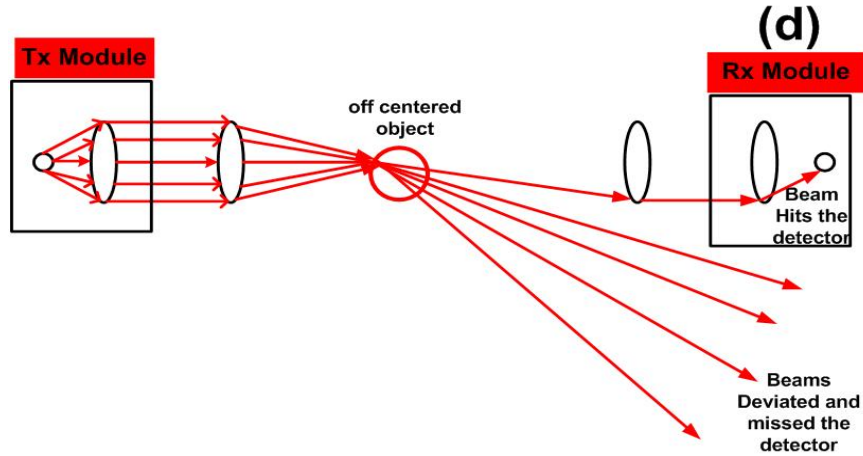
Figure 3.5 (d) Illustration of the beam steering of the THz radiation due to the refractive effects of the sample as an optical component in the system, when the sample is off centered (towards right when viewed on the direction of THz beam) with optical axis of the system.
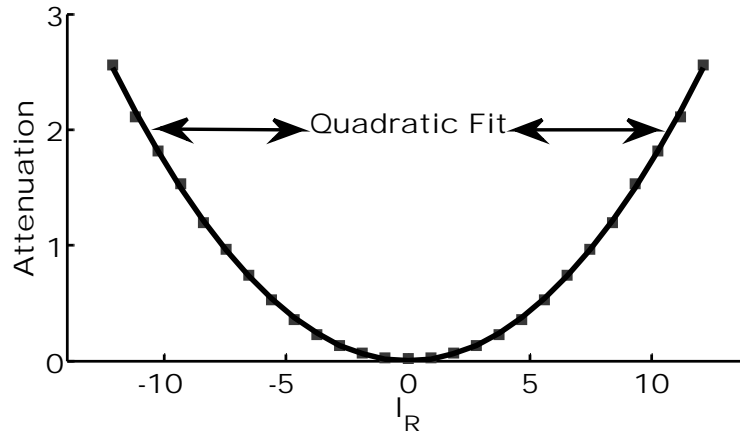
Figure 3.6 Predicted attenuation from ray-tracing simulation data (dotted grey curve) and quadratic fit (solid black curve). The fit is determined by $-\ln(T_{st}(l)) = al^2 + bl + c$ where a is 2.94. The values for b and c are on the order of 10^{-16} and can be regarded as zero respectively.

Figure 3.6 is the plot of the BEAM4 attenuation calculated as $A(l) = -\ln(T_{st}(l))$

where T_{st} is the transmission. For $|l| > 14$ mm (2R=28 mm), the attenuation is zero since

the sample is not in the path of the THz beam. Note that as $|l|$ increases above zero, the predicted attenuation due to beam steering $A_{st}(l)$ continues to increase monotonically. The maximum attenuation is capped at roughly 4.6 because this is the typical maximum attenuation, which can be measured due to the signal-to-noise limitations of the THz spectroscopy system is used. In practice, the attenuation due to steering becomes infinite for large values of $|l|$ due to extreme beam deviations as well as total-internal reflection of the THz beam at the sample-air exiting interface. In order to define a correction term due to beam steering, the central portion of the simulated attenuation is fitted to a quadratic polynomial given by $\ln(T_{st}(l)) = al^2 + bl + c$ where a, b, and c are constants determined by the best fit to the data of Figure 3.6.

The effects of beam steering can be included into Equation (3.5) using an additional factor $T_{st}(l)$ which accounts for the effective transmission of the THz-CT system in the presence of beam steering,

$$T(l) = T_{st}(l) \exp(-\alpha L_r) \left(1 - R_{pa}\right)\left(1 - R_{ap}\right)$$ (3.6)

where the left-hand side of Equation (3.6) is the measured THz transmission. Solving this equation for the parameter of interest α gives,

$$\alpha L_r = -\ln(T(l)) + \ln(T_{st}(l)) + \ln\left(1 - R_{pa}\right) + \ln\left(1 - R_{ap}\right).$$ (3.7)

Equation (3.7) illustrates the three correction terms that are applied to the measured THz attenuation prior to reconstructing the THz-CT image using a Radon transformation. The

last two correct the measured transmission for Fresnel losses at the air-sample interfaces. The second term corrects for beam steering. Figure 3.8 (a) shows a comparison of the measured THz attenuation $-\ln[T(l)]$ with beam steering correction term $\ln[T_{st}(l)]$. The correction term has been offset vertically in the plot in order to compare the shapes of the two curves. Note that the similarity in the two curves strongly suggests that the beam steering correction is much larger than the corrections due to Fresnel reflections.

3.4 Corrections for finite beam size

While the central dip in the measured attenuation of Figure 3.8 (a) can be explained because of beam steering and Fresnel reflection, the shape of the measured attenuation near the boundaries of sample result from the finite beam size of the probing THz beam. For large values of $|l| > 28$, sample is not in the THz beam path and the measured THz transmission (attenuation) is high (low). As the sample is scanned horizontally, the edge of the sample partially blocks the THz beam leading to an increase in measured attenuation. Due to the large angle of incidence near the edges of the sample, the beam steering is severe as none of the light, which enters the sample, is able to propagate through the sample to the detector. The attenuation near the edges of the sample, therefore, can be modeled assuming that the edge of the sample partially blocks the THz beam. Assuming that the THz beam propagates in the z direction as a Gaussian beam with a spot size of a_o at the focus, the local intensity of the THz beam is given by [94],

$$I(x, y) = I_o \exp(-2(x^2 + y^2)/a_o^2) \qquad (3.8)$$

where $I_0 = \dfrac{2P_0}{\pi a_0{}^2}$ and P_0 is the total power of the beam at any cross section. The total power of THz radiation which gets blocked by the sample edge can be calculated by integrating Equation (3.8) over the transverse directions as illustrated in Figure 3.7.
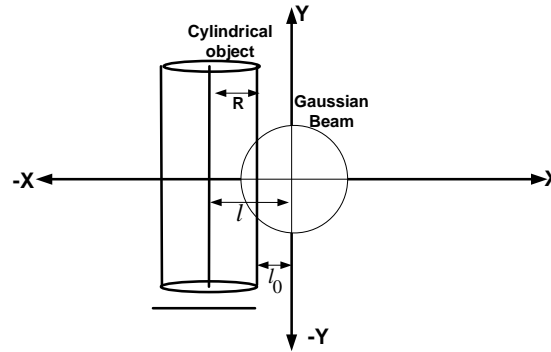
Figure 3.7 A cyllindrical object approaching a Gaussian beam which is propagating perpendicular to the page.

The measured transmittance near the sample's right edge (corresponding to positive values of l should be,

$$T_{edge}(l_R) = \sqrt{\frac{2}{\pi}}\frac{1}{a_0} \int_{-R(l_R-1)}^{\infty} \exp(-2x^2/a_0{}^2)dx \qquad (3.9)$$

where l respresents the horizontal (ie. x) location of the sample's edge from the centre of the beam. After integrating Equation (3.9) and taking the negative of natural log on the right side of the expression, one can derive the attenuation near the sample right edge as,

$$A_{edge}(l_R) = -\log_e\left[\frac{1}{2} + \frac{1}{2}erf\left(\frac{\sqrt{2}R}{a_0}(l_R - 1)\right)\right] \qquad (3.10)$$

For the left edge (negative values of l_R), the equation is the same except the limits of integration range from negative infinity to $-R(l_R + 1)$.

In summary, the correction algorithm is applied as follows:

- For each projection slice, Equation (3.10) is used to determine the location of the left and right edges of the cylinder relative to the center of rotation of the sample.

- Based on the maximum detectable attenuation (typically ~4.6) , the range of l values for which the measured attenuation is not instrument limited is determined.

- The correction terms of Equation (3.7) is applied to that range of l parameters.

- The ideal form of Equation (3.1) is used to fill in projection array data as a function of l in the "blind" region from the sample's to the boundary of the valid corrected data.

- Repeatation of each projection slice is done for rotation angles of the sample.

In Figure 3.8 (a), a typical plot of Equation (3.10) is shown for the left and right edges. From a best fit to the experimental data, one can extract the l locations of the left and right edges of the sample. The spot size of the beam was determined by comparing the plot of Equation (3.10) with the experimental attenuation.
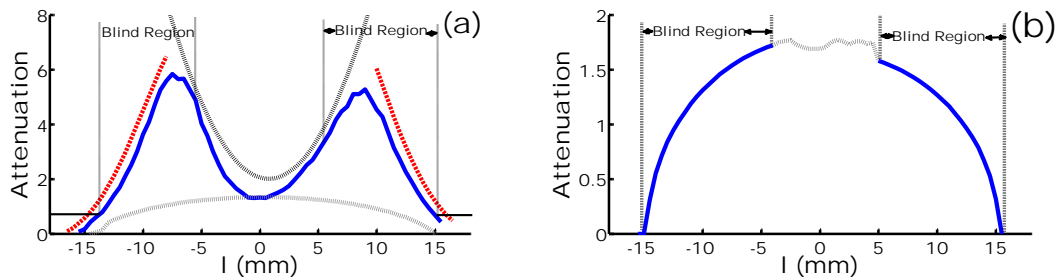
Figure 3.8 (a) Plot of experimentally measured attenuation (solid line), beam steering correction (dashed line) and predicted attenuation due the samples edge blocking the THz beam (dotted line). (b) Corrected attenuation from Equation (3.7) using the beam steering correction term determined from ray tracing and Equation (3.10) to determine the edges of the sample.

As part of the correction algorithm, one must account for the fact that the rotational axis for the tomography scans does not exactly coincide with the geometric

axis of the cylindrical rod. Consequently, the first step in the correction algorithm is to use Equation (3.10) to determine the left and right boundaries of the rod. Once these boundaries are determined, the offset between the rotational and geometric axes can be used to apply correction terms of Equation (3.7) for both Fresnel reflection losses and beam steering. For the cylindrically shaped samples, accurately determining the geometric center of the sample is essential particularly when applying the beam steering correction.

While the beam steering and Fresnel correction factors can be used to correct the middle portion of the projection data, the THz-TDS system's maximum limit to the measured attenuation as well as the severe beam steering when the THz beam passes near the edges of the rod means that the measured attenuation for $|l| > 17$ in Figure 3.8 (a) is an artifact and not related to the attenuation of the sample material. Therefore, in order to correct the attenuation projection data near the edges of the sample, one must assume a functional form for the data in this range and match the experimental data to the measured values in the region, which are valid. Since the cylindrical rods are supposed to be homogenous and uniform, the expected functional form for the attenuation projection array should ideally (in the absence of refraction) be due only to the attenuation coefficient α of the material and the length of material through which the THz beam propagates,

$$A_{th}(l) = \alpha \; L(l) = \alpha \; 2R\sqrt{1 - l^2 / R^2} \; .$$

(3.11)

At the physical edge corresponding to $l = R$, the attenuation through the material should have a limiting value of zero. Since the radius of the rod is known, the only free parameter in Equation 3.11 is the attenuation coefficient α. This value is determined by matching the corrected value of the measured attenuation at the largest value of l for which the measured data is valid. Figure 3.8 (b) illustrates a comparison between the ideally measured attenuation and the corrected attenuation for horizontal projection data through the Plexiglas sample for a fixed rotation angle.

The calculated refractive index and attenuation coefficient for THz ray of the plastic rod are 1.54 and 0.311/mm respectively. A close look at the experimental curve shows that the experimentally measured attenuation exceeds the experimental limit of detection from about $\left|l\right| \geq 5$ mm on each side of the center $l = 0$ position. Figure 3.8 (a) and Figure 3.8 (b) shows the experimental curve and model attenuation curve both for a plastic with no defects at a particular vertical position and at a particular angle. The theoretical (Equation 3.11) curve was used beyond $\left|l\right| > 4$ mm from the center position of the corrected curve, on both sides of the curve. From -4 mm to +4 mm, correction algorithm was used (Equation 3.7). It is important to know the geometrical center of rotation to generate the tomographic image and to successfully generate the corrected curve at each angle. The l value was determined on both sides $(-X_L$ and $X_R)$ of the Gaussian fit at an attenuation of 0.6931 and middle position was found by $\dfrac{-X_L + X_R}{2}$ on the straight line connecting those two points. That middle position is treated as the geometric center of the object under study. It was observed that the geometric center found were not exactly at zero position, rather it is shifted either towards left or towards

right depending on how closely the geometric center of the sample matched the rotational axis of the sample during experiments. Figure 3.3 (a) shows a plot of the experimental attenuation *versus l* value. The region beyond $|l| > 5$ is called a blind region because the reconstructed image in this region shows huge attenuation (Figure 3.3 (b)) because of the beam steering effect of the THz beam and thus no real information about the internal structure of the object can be obtained.
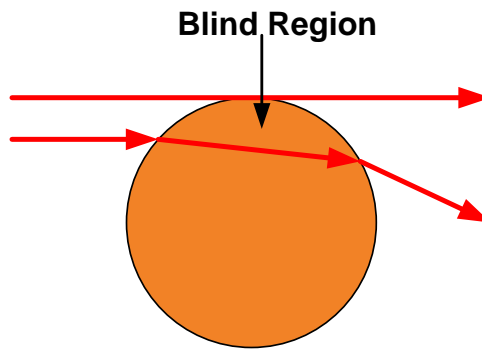
Figure 3.9 Pictorial description of blind region.

Figure 3.9 shows a pictorial description of the blind region. Since THz beam has a finite beam size, when it passes through the edge of the sample, part of the THz beam does not enter to the sample but part of it does enter to the sample. The portion of the beam, which enters to the sample, suffers huge beam steering and is not detected. Consequently, that region around the edge of the sample does not show proper attenuation through the material when subjected to THz radiation. Any defect on that region is also not properly diagnosable.

3.5 Application of correction Algorithm to the plastic rods (plexiglas)

The algorithm mentioned in previous chapter is applied to Plexiglas with no defect on it and with defects at the center and at the edge. Three different cylindrical shaped Plexiglas samples from the same stock material were prepared. On two of them, holes were drilled near the center region having different dimensions. One hole was made about 1mm in diameter and another hole was made about 5mm in diameter. The third Plexiglas was drilled with a 5mm hole near the sample's edge. The reason behind this procedure is to test the developed algorithm in different regions. It is also important to test this algorithm in the blind region (near the edge).
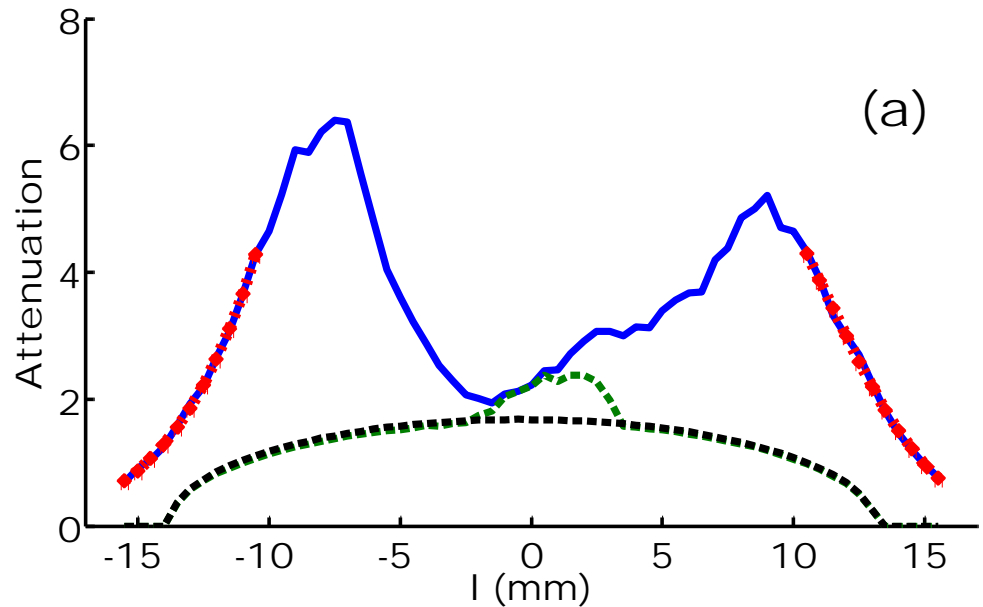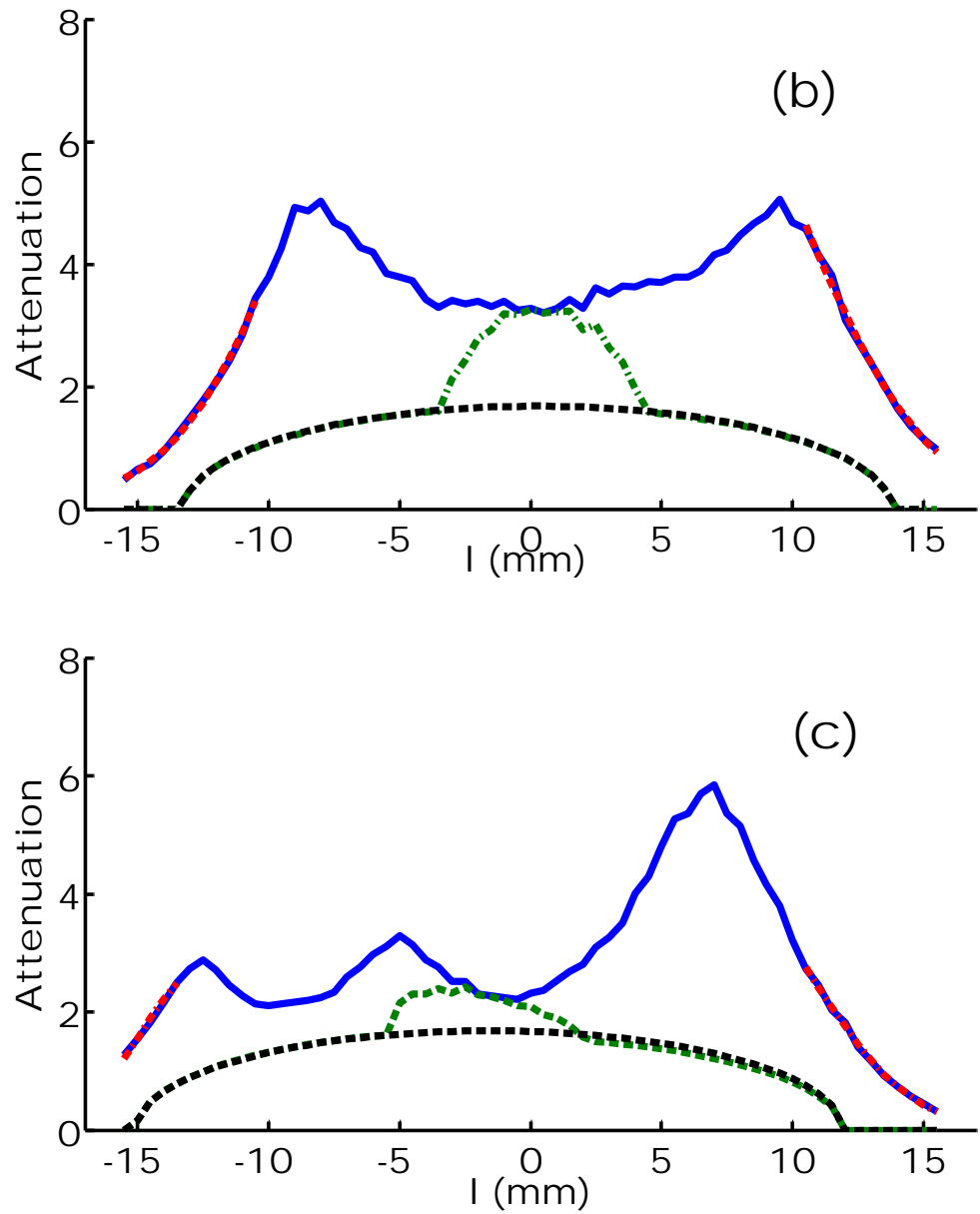
Figure 3.10 Experimentally measured (solid line), corrected (dashed) attenuation projection data along with model absorption curve at a fixed rotation angle for three Plexiglas sample with (a) A 1mm hole near its geometric center. (b) A 5mm hole near the center. (c) A 5mm hole near the edge.
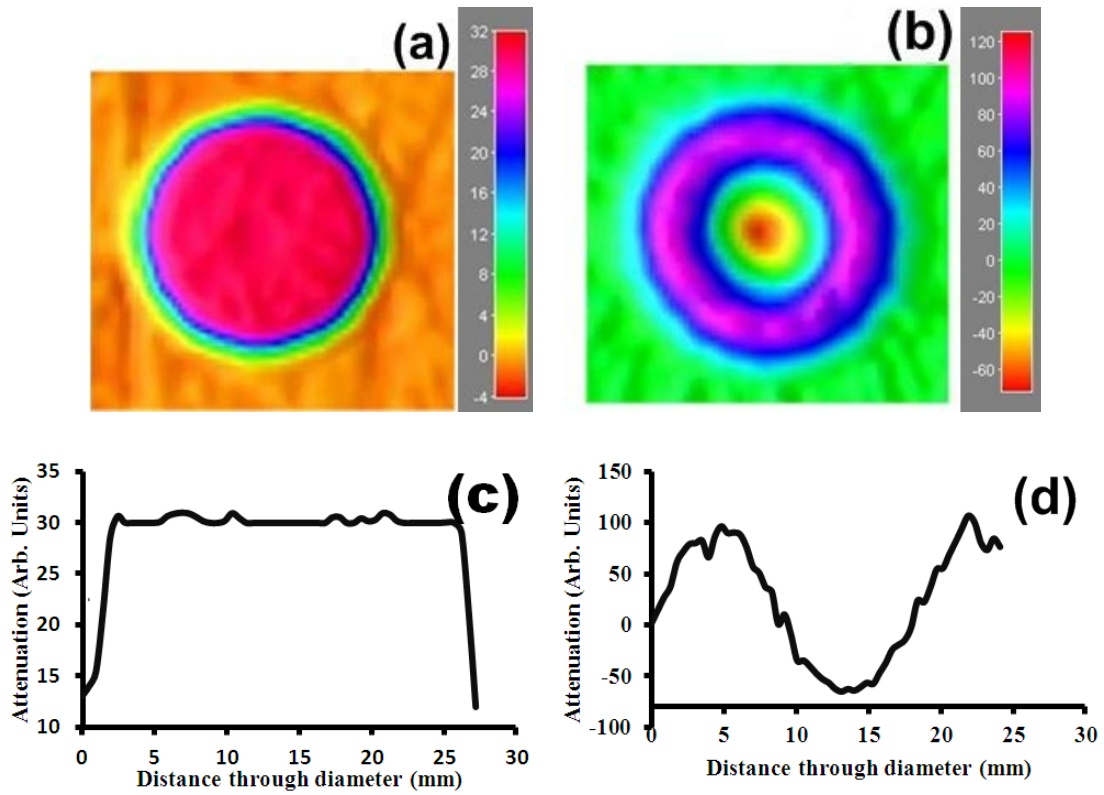
Figure 3.11 Reconstructed 2D tomographic images of the Plexiglas with no defect with (a) and without (b) correction algorithm applied (The scale in horizontal direction is in 0.5mm interval). Corresponding plot profiles of the images taken through the diameters are indicated in (c) correction applied and (d) no correction applied. (The scale in horizontal direction is in 1 mm interval).
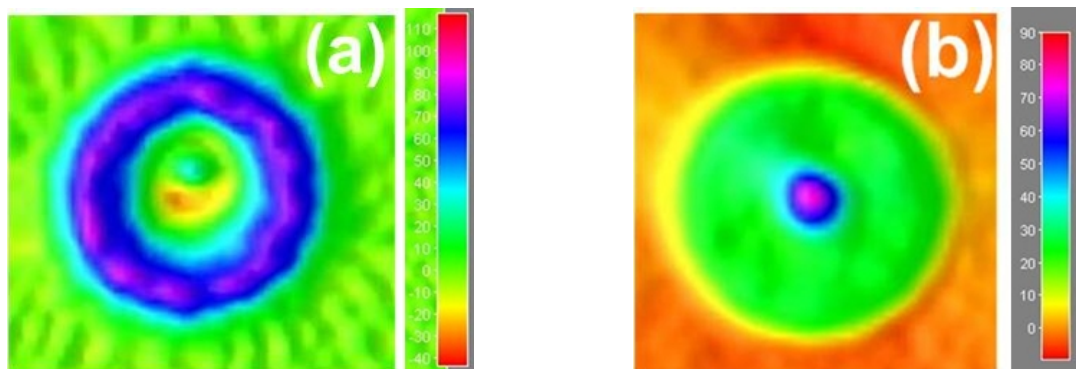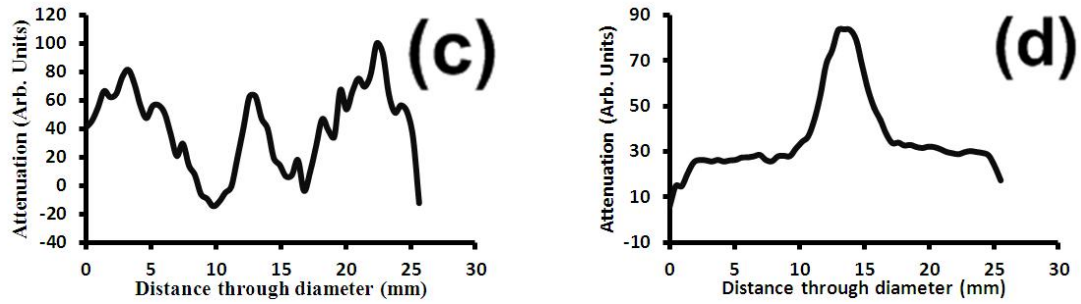
Figure 3.12 Reconstructed 2D tomographic images of the Plexiglas with a 1mm hole near the center without (a) and with (b) correction algorithm applied (The scale in horizontal direction is in 1 mm interval). Corresponding plot profiles of the images taken through the diameters are indicated in (c) no correction applied and (d) correction applied. (The scale in horizontal direction is in 1 mm interval).
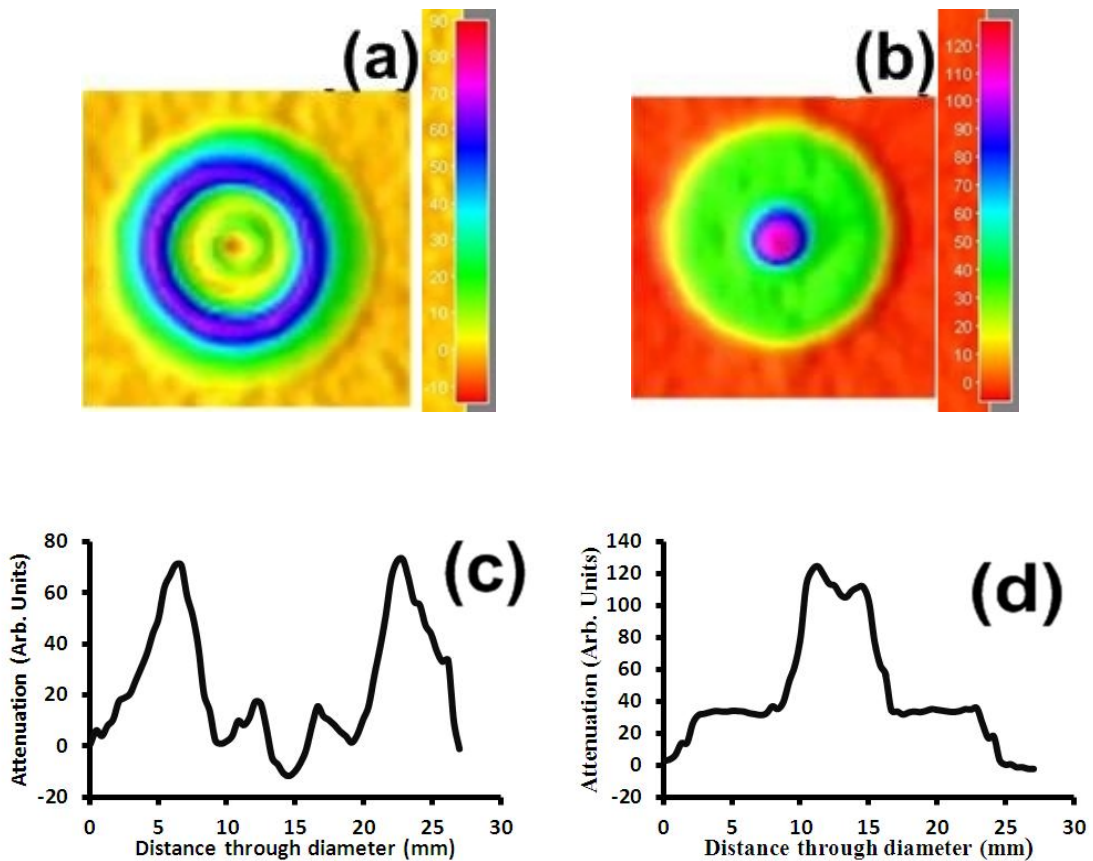
Figure 3.13 Reconstructed 2D tomographic images of the plastic rod with a 5mm hole near the center without (a) and with (b) correction algorithm (Continued to next page) applied (The scale in horizontal direction is in 1 mm interval). Corresponding plot

profiles of the images taken through the diameters are indicated in (c) no correction applied and (d) correction applied. (The scale in horizontal direction is in 1 mm interval).
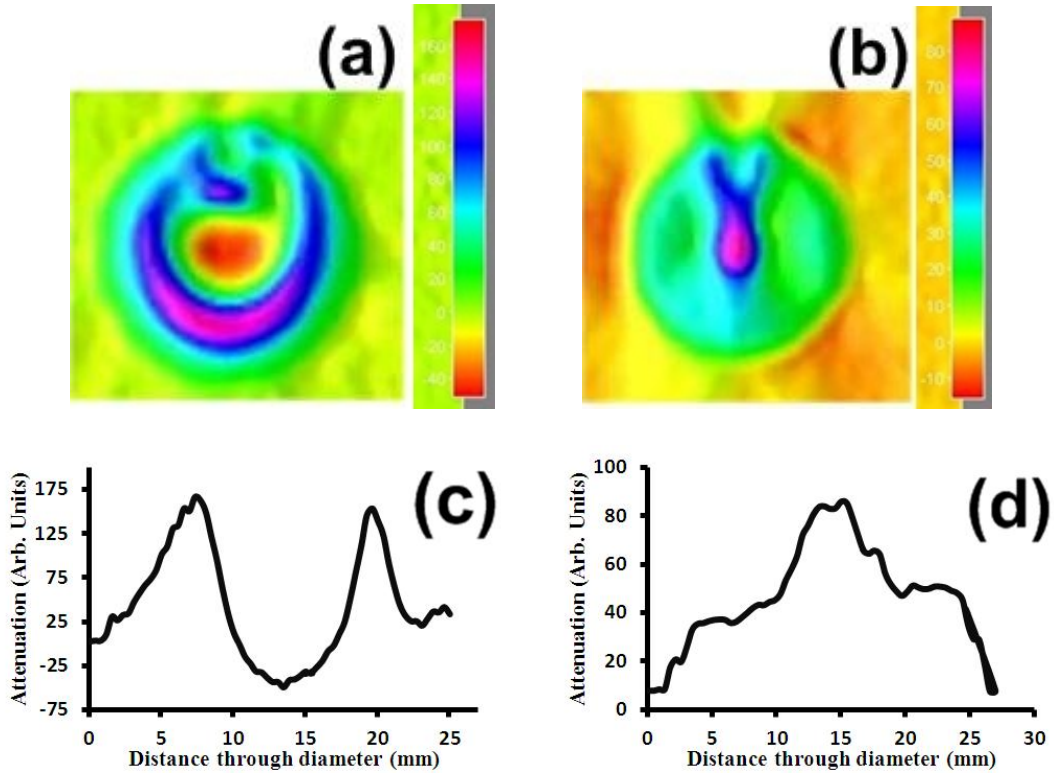
Figure 3.14 Reconstructed 2D tomographic images of the plexiglases with a 5mm hole near the edge of the sample without (a) and with (b) correction algorithm applied (The scale in horizontal direction is in 1 mm interval). Corresponding plot profile of the images taken through the diameters are indicated in (c) no correction applied and (d) correction applied. (The scale in horizontal direction is in 1 mm interval).

Figure 3.10 (a), Figure 3.10 (b) & Figure 3.10 (c) are the curves of typical THz attenuation projection data for Plexiglas rods having a 1mm hole near the geometric center, a 5mm hole near the geometric center, and a 5mm hole near the edge, respectively. In each plot, the uncorrected and corrected projection data are plotted. For each sample, the 'blind' region's ideal attenuation curve is matched to the corrected

attenuation data at $|l| = 4$ mm. Figure 3.11 to Figure 3.14 shows the reconstructed 2D CT images and plot profile of those Plexiglas rods both with and without the correction algorithm applied. Figure 3.11 (a) and Figure 3.14 (b) show the 2D reconstructed images of a slice of the plastic rod with no defect on it with and without the application of the correction algorithm respectively. In Figure 3.11 (b) an enhanced boundary is seen but in Figure 3.11 (a), those boundaries are well removed. Figure 3.11 (c) and Figure 3.11 (d) show the corresponding plot profiles taken through the diameters of Figure 3.11 (a) and Figure 3.11 (b), respectively. Figure 3.12 (a) and Figure 3.12 (b) shows the 2D reconstructed images of a slice of the plastic rod with a 1mm hole near the center without and with the application of the correction algorithm respectively. In Figure 3.12 (a) the enhanced boundary effect due to refraction dominates the reconstructed image so that the hole in the middle is obscured. The defect is clearly visible in Figure 3.12 (b) near the center region. Figure 3.12 (c) and Figure 3.12 (d) show the plot profiles of Figure 3.12 (a) and Figure 3.12 (b), respectively. In Figure 3.12 (c), three huge absorption peaks are visible, one near the center and two near the edges. The center one is because of the hole but the peaks near the edges result primarily due to the beam steering effect. Figure 3.12 (d) shows no such huge peaks near the edge. The reconstructed attenuation is constant, as it should be, except near the defect. From examination of all these plots and images, it is clearly visible that the new algorithm is able to eliminate the boundary effect and reconstruct a defective hole near the geometric center of the rod.

The reconstructed hole size looks much bigger than the actual size of the hole. It is because the hole itself acts as a lens for the THz beam and THz beam steers away around the hole and the result is more attenuation and thus shows bigger hole. The

images shown in Figure 3.13 (a, b, c & d) are the 2D THz-CT reconstructed images and plot profiles of a rod with a 5mm hole at the center region. As with the 1mm hole images, the uncorrected image of Figure 3.13 (a) shows an enhanced boundary such that the defect at the center is not obvious. Figure 3.13 (b) shows 2D reconstructed THz-CT of a slice of this same cylindrical rod after the correction algorithm is applied. The defect at the center is clearly visible along with the elimination of the boundaries. Figure 3.13 (c) and Figure 3.13 (d) are the plot profiles of the same plastic cylindrical rod without and with the application of the correction algorithm respectively. After applying the correction algorithm to the experimental data, the boundary effect resulting from beam steering and Fresnel reflection losses are removed from the image and an attenuation peak is seen at the center resembling the bigger hole. The size of the reconstructed hole is almost comparable to the true size of the hole. Figure 3.14 (a, b, c & d) are the 2D reconstructed images and plot profiles of a plastic rod having a 5mm diameter hole almost near to the edge of the rod.

It has been discussed earlier that due to the steering of the THz-beam near the edges, it is very difficult to see any defects in those 'blind' regions. The reconstructed images are shown in Figure 3.14 (a, b, c & d). Figure 3.14 (a) is the uncorrected CT image. As with the other samples, evidence of some structure near the boundary is clearly present, but masked due to the boundary effect. When the correction algorithm is applied, presence of a defect is clearly visible, and the boundary effect is removed. However, the exact shape and location of the defect is not accurately reconstructed. Looking at the plot profiles it is also difficult to distinguish any hole near the boundary but an anomaly in the shape of the outer region (Figure 3.14 (c)) reveals something is present. However, Figure

3.14 (d) clearly depicts no boundary effect except some extra widening of the curve near the right side of the boundary, which is different from Figure 3.13 (d) and Figure 3.14 (d). Overall, one can conclude that if the defects were near the interior of the sample, then the defects would be reconstructed in the corrected image. However, if the defects are in the boundary (blind) region, the reconstructed images can visualize the presence of a defect, but not its exact location and size.

CHAPTER 4

NON-DESTRUCTIVE EVALUATION (NDE)

OF CORK BY TERAHERTZ IMAGING

4.1 Introduction

Natural cork is acquired from the Cork Oak (Quercus suber) which grows predominately in Portugal and other countries surrounding the Mediterranean Sea. It is utilized in a variety of products including cork stoppers for wine and other beverages. As an enclosure for liquids, it has the desirable properties of being largely impermeable to liquids and gases, as well as compressible [95]. With natural cork as well polymers and pharmaceuticals, the permeability or diffusion of liquids and gases is an important issue [88, 89, 96, 97]. As an example, the performance of controlled delivery pharmaceutical products is determined partially by the diffusion of solvents into their polymeric coatings. Likewise, the characterization of water diffusion in wood plastic composites, due to their use in construction applications, is essential. Natural corks are widely used as a wine stopper in wine industry. It is very important to monitor diffusion of gasses especially oxygen through natural cork samples used as a wine stopper [89, 98-101]. Diffusion of oxygen through natural cork used as a wine stopper could spoil wine, as oxygen converts wine to vinegar [102-105]. The diffusion of liquids and gases in natural corks is anisotropic [95] in the radial, axial and tangential directions.

The radial direction corresponds to the direction of the radial growth of the Cork Oak tree. The axial direction is parallel to the tree's axis. The transverse direction corresponds to the direction along the circumference of the tree's diameter. The anisotropy in diffusion is attributed to several effects. For example, it is well-known [95,

106] that the diffusion coefficient in the radial growth direction is larger than that of the other two directions due to the presence of lenticular channels (pores) that run parallel to the radial growth direction which aid water and gases diffusion through the cork. In addition, one would expect the presence of cracks, voids, and defects to increase the diffusion. The presence of these potentially highly anisotropic features in the cork implies a highly variable *local* diffusion rate for both liquids and gases. Therefore, the motivation for using THz imaging for non-destructive evaluation of corks is to probe the inner structure of the cork for lenticels, cracks, and imperfections, which determine the local diffusion rate. 3-D THz-CT imaging is essential since the full 3-D interior structure must be analyzed.

4.2   Cork biology and production

The cork used as a wine stopper is produced from the bark of the cork oak tree (Quercus suber L) [66]. According to the plant anatomy, cork is a tissue and separates the living cells inside the plant from the outside environment. Cork is a cellular material with closed cells because it has a regular structure of closed cells. In the 16th century cork was observed and described by Robert Hooke [66]. Because of the biological origin of the cork, it is formed by the secondary meristem phellogen in the outer bark of trees as part of the periderm [47]. Cork is widely used as a wine bottle stopper, insulating and surfacing product etc. The structure, chemical composition and properties of natural cork have thoroughly been studied and written in a well-articulated way by Pereira [66]. Upon looking at the structure of the cork, it has been noticed that, it has thin walled cells forming hexagonal prism and are stacked base to base in regular rows without intercellular voids. During the growth of these cells and tissues, there could be periodic

variation of cell size and density. The properties of the cork related to the cellular structure and the quality of a cork is widely determined by its structural contents.
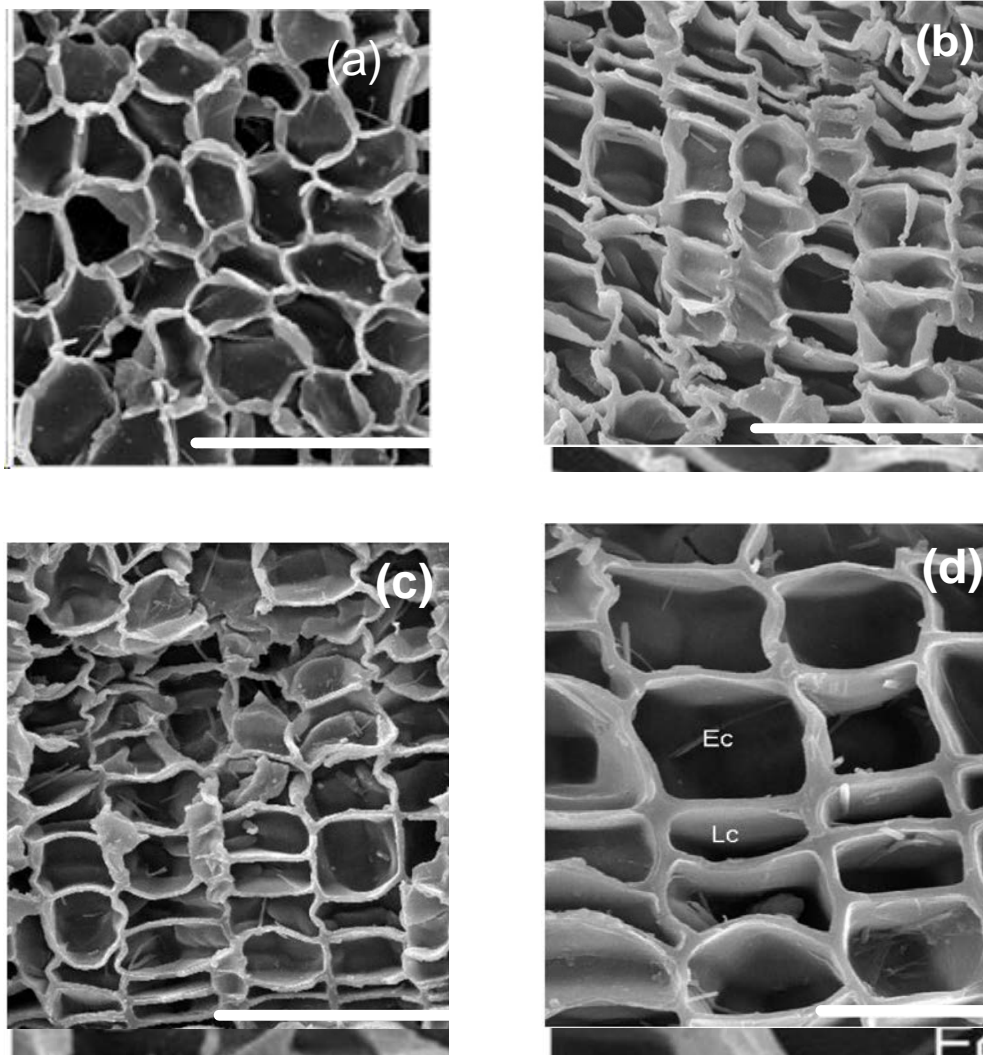
Figure 4.1 (a) SEM of cork from the bark of Q cerris var.cerris (tangential section). (b) SEM of cork from the bark of Q cerris var.cerris (transverse section). (c) SEM of cork from the bark of Q cerris var.cerris (radial section). (d) SEM of cork from the bark of Q cerris var.cerris showing a ring organization with alternating layer of early cork (E_c) and latecork (L_c). Scale bar for Figure 4.1 (a, b, & c) is 100 µm. Scale bar for Figure 4.1 (d) is 30 µm. [107]

In the above Figure 4.1 (a, b & c) the structures of the cork by scanning electron microscope (SEM) are shown in three principal sections. In those figures, the cells are arranged without gaps or intercellular voids. As shown in Figure 4.1 (a), the cells are arranged in honeycomb-type structures, appearing as polygons. The transverse as shown in Figure 4.1(b) and radial as shown in Figure 4.1 (c) sections look similar because the individual cells are approximately rectangular. The layered ring structure of cork cells is shown in Figure 4.1(d). This layered ring structure is divided into two portions known as early cork cells and late cork cells. Early cork cells are larger but late cork cells are smaller in dimension. Early cork cells are formed in the first period of growth and late cork cells are formed at the end of the previous growing season [107].
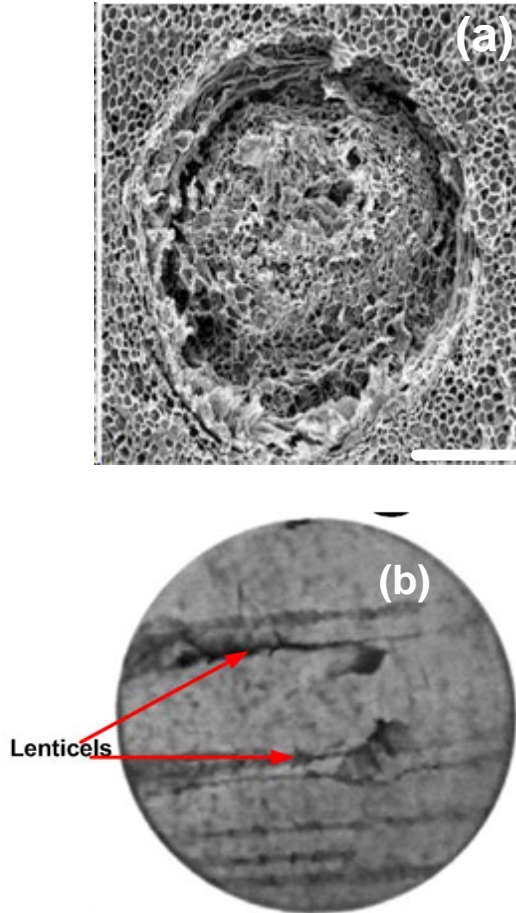
Figure 4.2 (a) SEM picture of the tangential section of the cork from the bark of Q, cerris Var. cerris is showing one lenticular pore. (Scale 300 µm). [107] (b) cross section of a wine cork showing a lenticel in the radial growth direction.

The natural cork is not structurally homogeneous but has structural defect inside it. One of the defects is shown in Figure 4.2 (a). Figure 4.2 (a) shows a lenticular discontinuity (also known as lenticular channel) in the tangential section of a cork tissue. These lenticular channels are prevalent in wine cork stoppers along the circular cross-section of the stopper (Figure 4.2 (b)).

4.3   THz imaging of natural cork – prior studies

Terahertz radiation is non-ionizing and it does not harm or destroy living organelles or tissues. Because of its nature, THz radiation is widely used as a non-destructive evaluation tool to inspect or characterize different materials without causing any damage. The long-term objective of this work is to study internal structural defects and other surface defects on the surface or inside the cork samples, though three-dimensional THz computed tomography. Cork samples were acquired from Amorim Corporation in Portugal. Amorim produces roughly 25% of the world's cork and roughly 3-4 billion corks per year. The samples provided have been classified according to quality via the industry standards for visible inspection. Simply stated, the quality of a wine cork is graded based on the number, size, and depth of cracks, voids, and lenticels that are visible on the cork surface (Figure 4.3).

Recently, THz radiation has been used to study non-destructive evaluation of natural cork [108]. In their work, the authors studied the internal structure of natural cork samples using THz radiation. In the case of natural cork, the large volume of the cork cell lumen (Figure 4.4) and relatively low humidity enables the material to be compressible, yet exhibit high THz transmission.
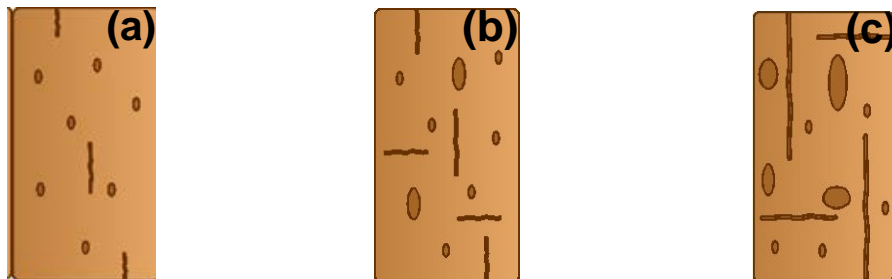
Figure 4.3 (a) Cork Type A. (b) Cork Type B. (c) Cork Type C.
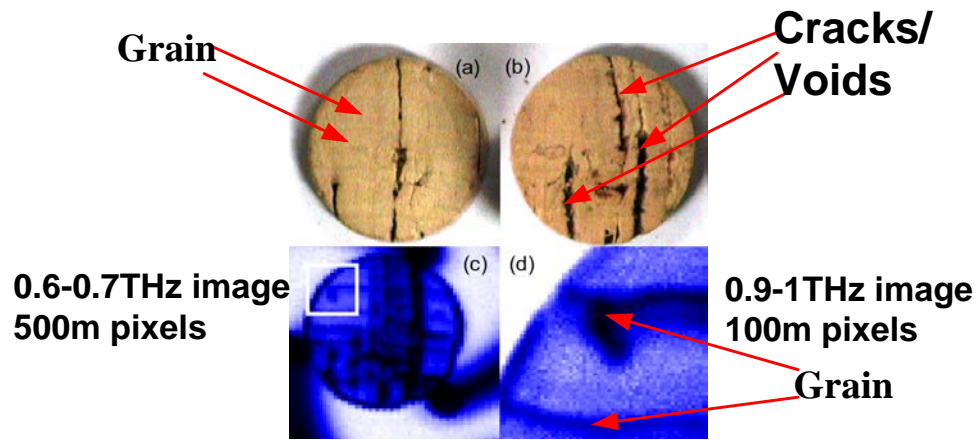
Figure 4.4 THz reveals hidden cracks/voids/and defects due to scattering of THz radiation.[108]
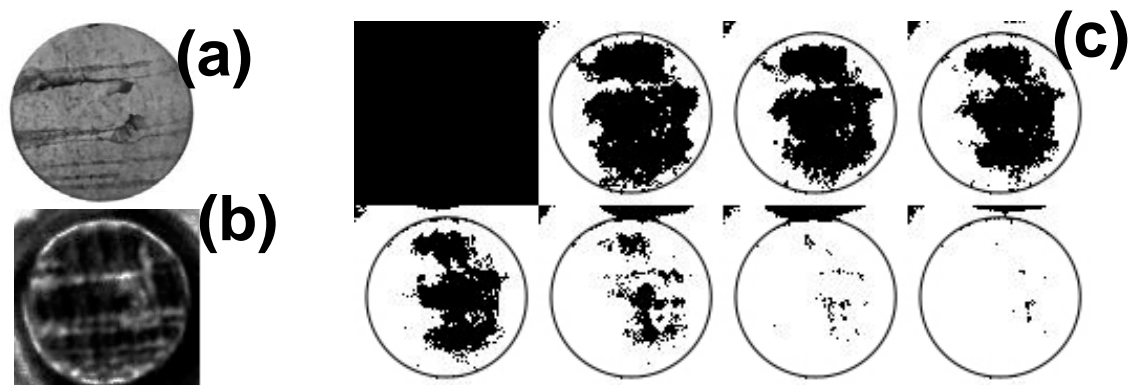
Figure 4.5 Diffusion of Water follows lenticular channels and voids in natural cork. (a) Visible image of a 4mm thick slice of cork from a wine stopper. (b) THz attenuation image through the cork slice. (c) Map of the diffusion front of water through the cork slice as a function of time. Note that the diffusion is dominated by the lenticular channels and voids in the sample. [88]
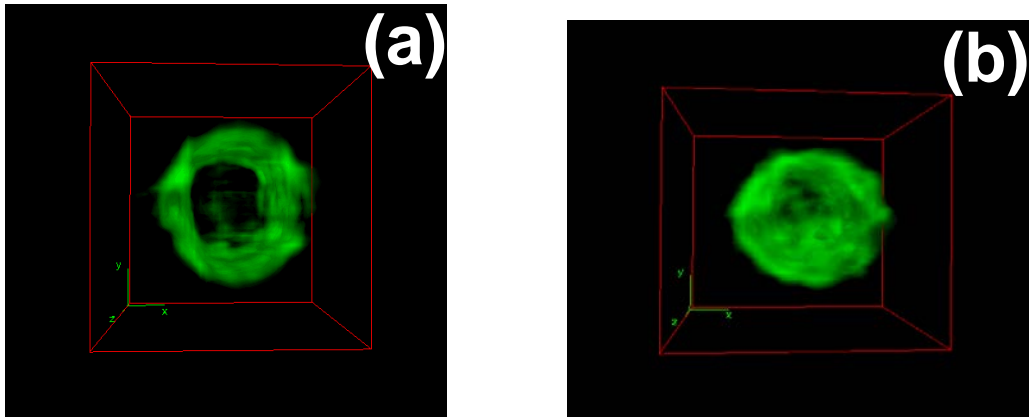
Figure 4.6 Comparison of THz 3D CT images between (a) transparent cork (less defective) and (b) opaque cork (highly defective).

Cork Defect
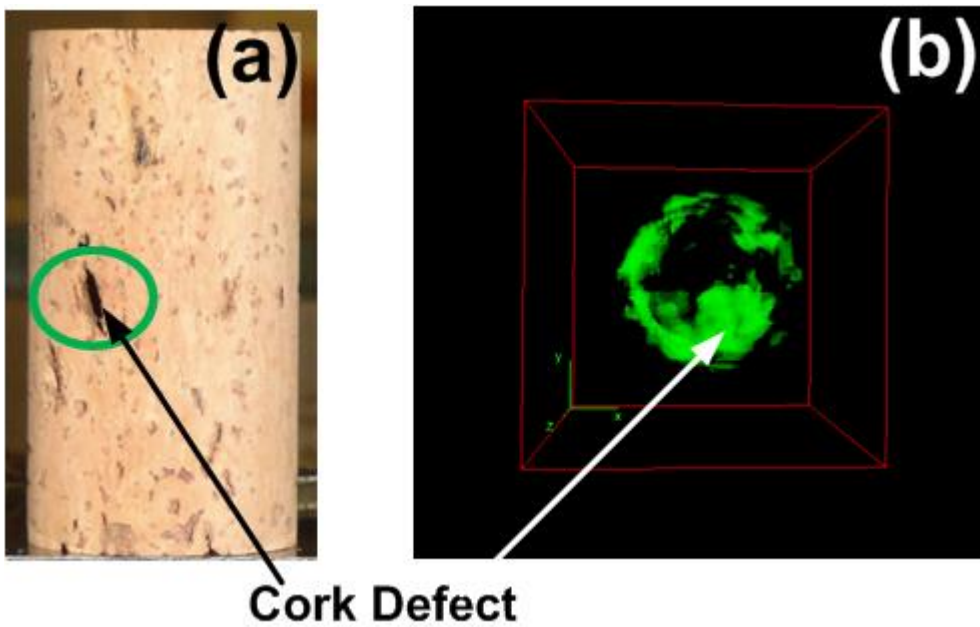
Figure 4.7 (a) Visual image of a cork showing a large defect on the surface. (b) THz 3D CT image of the same cork revealing the large internal defect.

Pulsed THz-CT has been used to study [108] the internal structure of natural cork. Figure 4.4 (a & b) shows visual images of natural cork slice (4mm thickness) with

various defects. Cracks and voids are clearly visible. Hor *et al.* produced images of those cork sample by THz radiation [108] and authors have clearly demonstrated the ability of THz imaging to detect the existence of defects Figure 4.4 (c & d). From the THz image cracks and voids are clearly visible as well as the grains of the cork sample. The presence of defects such as cracks and voids as well as the presence of lenticels should strongly affect the diffusion of gasses and liquids. Teti *et al.* studied the diffusion of water through natural by THz imaging [88] as shown in Figure 4.5. Authors studied both visible and THz images of dry natural cork. As water diffuses into the cork, the THz attenuation significantly increases thereby enabling a visual mapping of the diffusion front. It has been noticed that the diffusion coefficient depends on the presence of crack, voids, lenticels etc in the cork sample and thus those defects could potentially increase diffusion rate inside the cork sample.

Some of the early THz-CT images studied of wine corks [69] are shown in Figure 4.6 and Figure 4.7. Figure 4.6 (a) and Figure 4.6 (b) are reconstructed images of a highly transparent and highly absorptive cork, respectively. Both images are shown looking longitudinally (through the axis) through the cylindrical wine cork shape. Note the presence of the boundary effect in Figure 4.6 (a) dominates the image and masks the internal structure of the cork.

Figure 4.7 (b) shows a reconstructed 3D image of a cork, which has a known defect on its outer surface. Figure 4.7 (a) is the visual image of a cork and on its surface there is evidence of a void (hole) in the interior cork structure. Figure 4.7 (b) is the 3D reconstructed image of the same cork by THz-CT. While the presence of a void is evident in the image, the boundary effect obscures the structural details.

4.4 THz Computed Tomography (THz-CT)

of natural cork with correction Algorithms

THz-CT projection data is acquired as described in section 2.2. During the course of CT scanning, the cork rotates in 2-degree intervals with a total 90 rotations (*i.e.,* 180 degree). The scanning interval for l is 0.5mm while the scanning interval in the z direction is 1 mm. A LABVIEW code was written to control the rotation of a computerized stage and interface to the T-Ray 2000 software. Figure 4.8 (e) is the plot of experimental attenuation of the THz radiation, theoretically calculated attenuation and model attenuation of a natural cork sample with an insect hole which was created perpendicular to the page. For plastic rods (Section 3.5) the merging of the model attenuation with the theoretically calculated attenuation was made at $l=4$ mm on both sides of the center position. However, in case of cork, the merging was done beyond $l=7.5$ mm on both sides of the center position. The reason behind this is the higher refractive index of the plastic (1.54) compared to that of cork (1.1). Because of the higher refractive index of the plastic, the THz beam refracts more than it does inside the cork. In addition, because of increased bending inside the plastic, the 'blind' region predominates more for the plastic than it does for cork. As discussed earlier, in the 'blind' region, the beam steering effect is so severe that any rays which propagate through these sections of the sample for a range of angular rotations never reach the detector. For cork, because of its lower refractive index, this blind region is smaller than for plastic, *i.e.*, THz beam steers less in cork than in plastic rod. Figure 4.8 (a, b, c & d) are the 2D reconstructed images of THz-

CT and plot profiles of a natural cork having a wormhole inside it. Figure 4.8 (a) shows a clear boundary surrounding the cork (blue & green color) when no correction is applied. When the correction algorithm is applied, the enhanced boundary is removed. The long straight blue region in Figure 4.8 (b) shows the presence of lenticels, which is not visible in Figure 4.8 (a) and the pink region near the center represent the presence of a hole. Figure 4.8 (c) is the plot profile of the same cork but with no correction algorithm applied to it. Two big boundaries are visible in both sides of the center region (near the edge) but after applying the correction algorithm to the experimental data, the boundary effect is completely gone as shown in Figure 4.8 (d) and also the presence of some short of defect is visible (bigger peaks), which are actually the worm hole and lenticel. Therefore, the correction algorithm developed has also been tested in natural cork. Its application suppresses the boundary effect enabling better visualization of the internal structure.
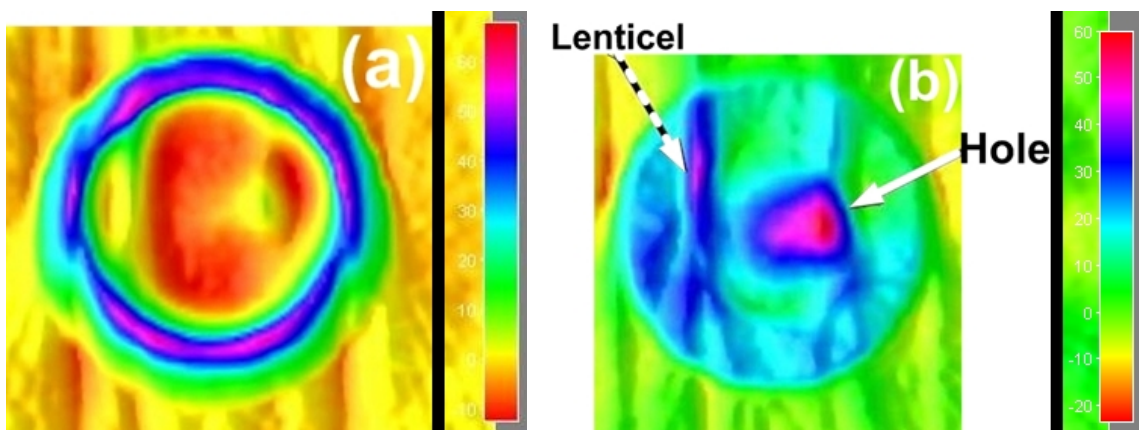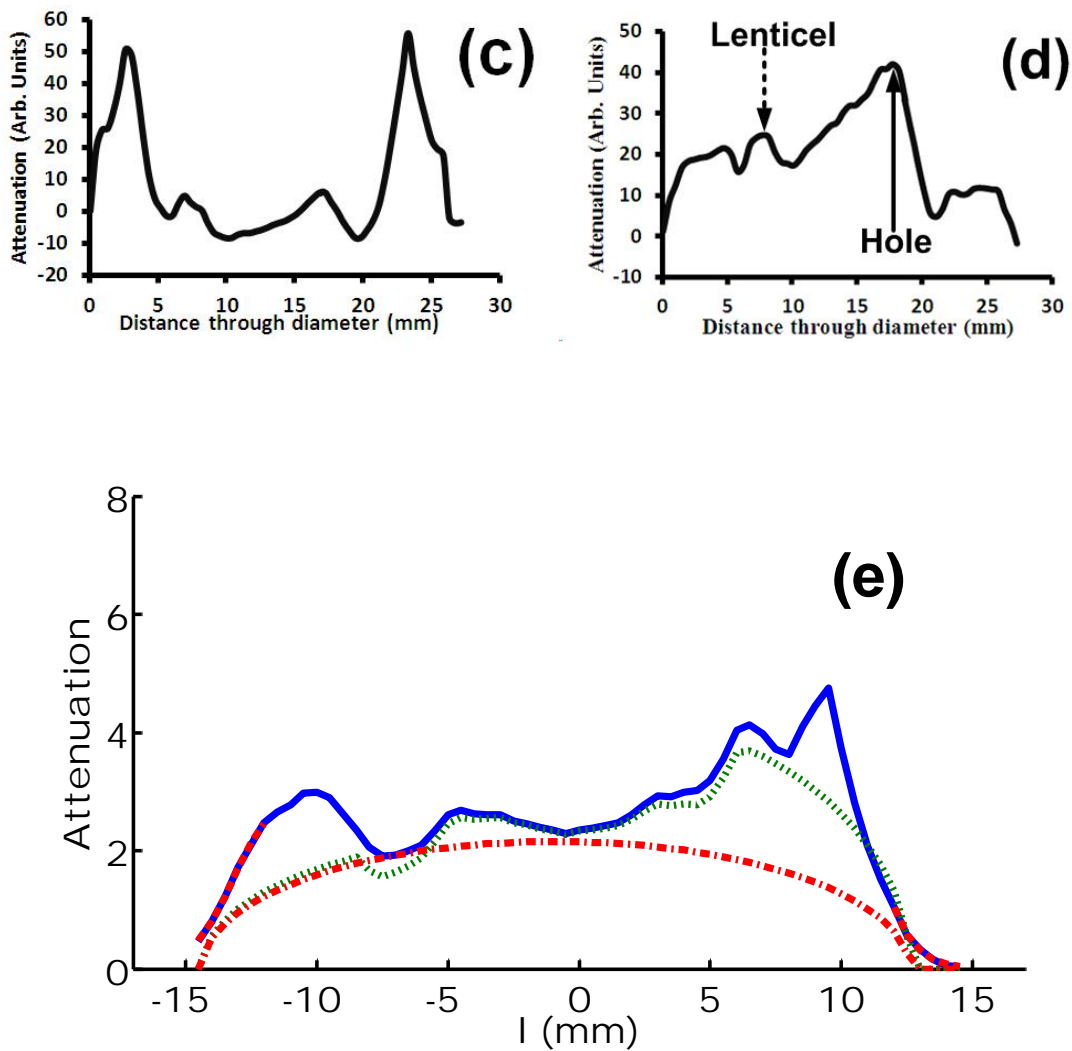
Figure 4.8 Reconstructed 2D tomographic images of a natural cork without (a) and with (b) correction algorithm applied. Corresponding plot profile of the images taken through the diameters are indicated in (c) no correction applied and (d) correction applied. (e) Experimentally measured (solid line), corrected (dashed) attenuation projection data along with model absorption curve at a fixed rotation angle of the natural cork sample.
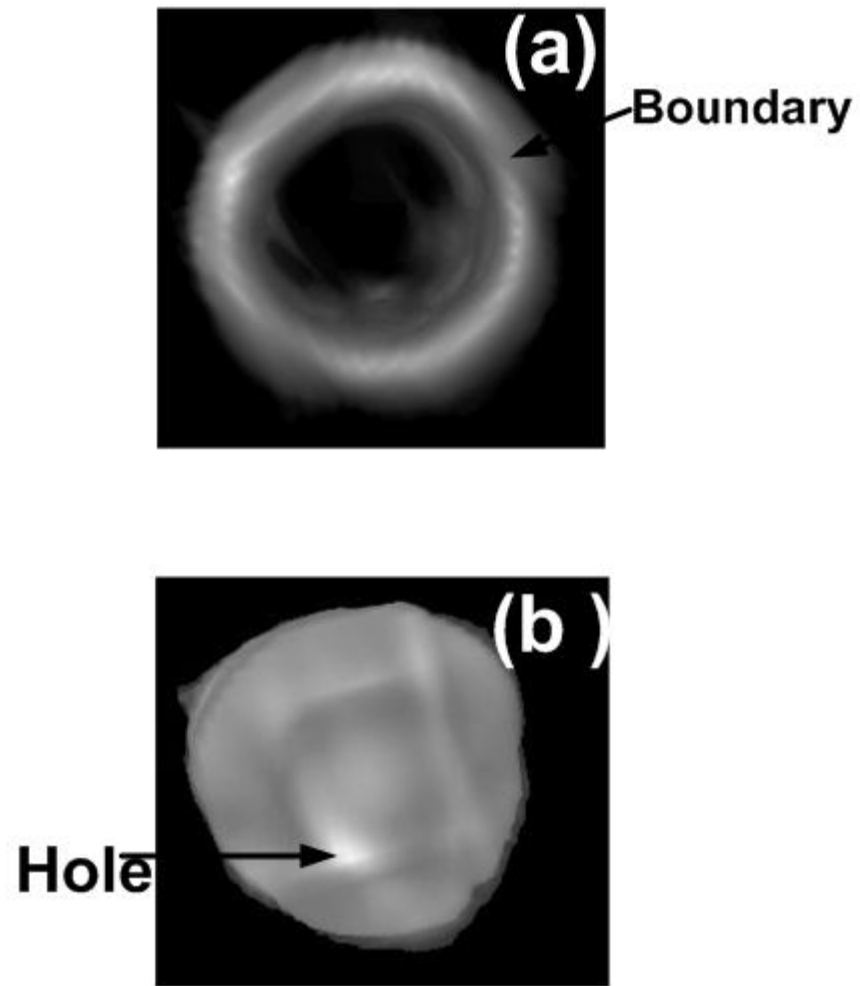
Figure 4.9 Complete 3D THz tomographic image of natural cork (a) without correction algorithm applied and (b) with correction algorithm applied.
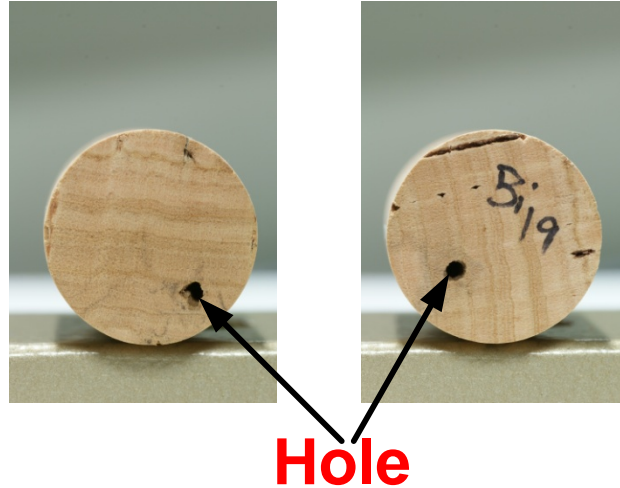
Figure 4.10 Visual image of the natural cork shows hole.

Figure 4.9 (a & b) are the 3D tomographic THz-CT images of the natural cork without and with the application of the correction algorithm developed at an averaged frequency between 0.1-0.2 THz. It is clear from those two images that the boundary has been removed when the correction algorithm is applied. Also the cork has a hole (as shown in Figure 4.10) which is completely unrecognizable in Figure 4.9 (a). However, when the correction algorithm is applied, the presence of the hole can be recognized in one of the end in the reconstructed image as shown in Figure 4.9 (b).

4.5   Conclusions and future work

The refraction of THz radiation as it propagates through a sample is a fundamental limitation for THz computed tomography and the boundary effect which arises because of the Fresnel reflection and beam steering is a fundamental issue in THz-CT. The boundary phenomenon is a fundamental problem for all THz-CT and the work described in this dissertation is very novel and fundamental in this regard.

In order to develop correction algorithms for the removal of the boundary effect phenomena, cylindrical Plexiglas rods were studied using THz-CT scanning. Due to the enhanced loss of the THz power at a boundary because of both Fresnel reflection losses as well as refractive losses, reconstructed THz–CT images exhibit enhanced attenuation at the boundaries and a distortion of the boundary shapes. The predominate effect of the enhanced attenuation is beam steering of the THz beam from its optimally aligned path to the detector. Essentially, the sample under study acts as an optical component in the THZ-CT system, which steers the beam in different directions depending on it position relative to the THz beam. This steering of beam is the main contributor to the anomalously large attenuation in the boundaries of the reconstructed images. Prior attempts (Abraham *et al.*) to correct the boundary artifacts were marginally successful.

In this dissertation, a methodology of removing boundary artifacts in THz CT imaging for cylindrically shaped objects is introduced. A mathematical algorithm for correcting CT projections prior to image reconstruction is described. The algorithm corrects for the loss of THz power due to Fresnel reflection at the boundary as well as the steering of the THz beam through the sample due to refraction. Most importantly, the loss of THz power through the collection of optics of the THz detection system is modeled. In

this dissertation, the developed algorithm eliminates the effect of the Fresnel reflection and beam steering, so that the anomalous attenuation in the reconstructed image can be removed. Essentially, the goal is to develop algorithms to correct the measured attenuation prior to Radon transformations.

The algorithm for the elimination of the boundary effect arises in pulsed THz-CT is tested successfully for cylindrical shaped objects (in this case with Plexiglas and cork). It is proven that the boundary effect can be eliminated for cylindrical shaped object. With the boundary effect removed, the internal structure of a material, including any defects inside the material, are more easily visualized using the algorithms developed in this dissertation.

It has been observed that the algorithm works well if there is any defect near the center region, but it does fail to generate clear image if the defects are in the blind region of the object. While the reconstruction of a defect in the blind region is not perfect, compared to an uncorrected image, one can clearly observe the presence of some structural imperfection in the sample.

In applying THz-CT to non-destructive evaluation of natural cork stoppers, the strong boundary artifact makes resolution of the mass density variations, cracks, voids, and channels of the cork structure difficult to discern. For natural cork, it is the internal structure, which is thought to determine the gas diffusion properties of natural cork, which are essential for the functionality of natural cork as barrier to gas and liquid diffusion.

Although the algorithm developed in this dissertation is quite successful in removing the boundary artifacts, there are limitations. It has been observed that the

region near the edge of example is 'blind' to the probing THz radiation due to strong refractive effects as well as the the finite spot size of the THz beam. Consequently, defects of structure, which are present in the blind region near the samples edge, are difficult to distinguish. While the correction algorithm developed in this dissertation makes the presence of defects near the edge easier to visualize, the reconstruction shape and location of the defects is not accurately reconstructed with the correction algorithm.

Again, another big limitation of this algorithm is, the correction algorithms as developed in this dissertation could only be applied to cylindrically shaped objects and not any other arbitrary shaped objects. However, if one knew a-priori the outer shape of a sample as well as the 'normal' attenuation and refractive index properties of the samples composition, in principle one could calculate using ray-tracing software the correction term of Equation 3.7 for beam steering. While the determination of the beam-steering correction term might be too onerous for an random object, if THz-CT images were required for non-destructive evaluation of a large number of objects each with the same composition and spatial dimensions, one could conceptually determine the beam-steering correction term for a standard 'model' object and use the corrected THz-CT images to visual defects from the 'standardized' object. As an example, wine corks are typically all cylindrical in shape with a standard diameter and length. While the outside shapes of the billions of corks produced annually are all nominally the same, their performance – which is determined by the internal structure of the cork – varies from sample to sample. For that example, application of the correction algorithms for non-destructive evaluation of defects in an otherwise uniform cork might be viable.

There are some obvious future research directions, which could improve this algorithm. Clearly, it is very important to develop the algorithm further to incorporate the region near the edge (blind region), so that defects near those regions, (blind region) could be clearly visible if the algorithm was applied. One option is to modify the Radon transformation approach to include non-parallel projection arrays.

REFERENCES

1. [cited 2013 04/25/2013]; Available from: http://lts.fzu.cz/img/en/spectrum_b.gif.

2. C. Jansen, S. Wietzke, O. Peters, M. Scheller, N. Vieweg, M. Salhi, N. Krumbholz, C. Jördens, T. Hochrein, and M. Koch, *Terahertz imaging: applications and perspectives.* Applied Optics, 2010. **49**(19): pp. E48-E57.

3. H. Louise, Effects of film coating thickness and drug layer uniformity on in vitro drug release from sustained-release coated pellets: A case study using terahertz pulsed imaging. International Journal of Pharmaceutics, 2009. **382**: pp. 151-159.

4. J. F. Federici, B. Schulkin, F. Huang, D. Gary, R. Barat, F. Oliveira, and D. Zimdars, *THz imaging and sensing for security applications—explosives, weapons and drugs* Semiconductor Science and Technology, 2005. **20**(7): pp. S266-S280.

5. J. F. Federici, *Detection of explosives by Terahertz Imaging*. 1 ed. Counter-Terrorism Detection Techniques of Explosives2007: Elsevier.

6. H. S. Chua, Terahertz time-domain spectroscopy of wheat grain, in Joint 29th international conference on Infrared and Millimeter waves and 12th international conference on Terahertz electronics2004, IEEE: Karlsruhe, Germany. pp. 399-400.

7. H. S. Chua, J. Obradovic, A. D. Haigh, P. C. Upadhya, O. Hirsch, D. Crawley, A. A. P. Gibson, L. F. Gladden, and E. H. Linfield. *Terahertz time-domain spectroscopy of crushed wheat grain*. in *Microwave Symposium Digest, 2005 IEEE MTT-S International*. 2005. Long Beach, CA: IEEE.

8. S. Hadjiloucas, L. S. Karatzas, and J. W. Bowen, *Measurements of leaf water content using terahertz radiation.* Microwave Theory and Techniques, IEEE Transactions on, 1999. **47**(2): pp. 142-149.

9. S. Hadjiloucas, R. K. H. Galvão, and J. W. Bowen, *Analysis of spectroscopic measurements of leaf water content at terahertz frequencies using linear transforms.* Jourrnal of Optical Society of America A, 2002. **19**(12): pp. 2495-2509.

10. C. Jördens, M. Scheller, M. Breitenstein, D. Selmar, and M. Koch, *Evaluation of leaf water status by means of permittivity at terahertz frequencies.* Journal of Biological Physics, 2009. **35**(3): pp. 255-264.

11. M. Reid and R. Fedosejevs, *Terahertz birefringence and attenuation properties of wood and paper.* Applied Optics, 2006. **45**(12): pp. 2766-2772.

12. J. Balakrishnan, B. M. Fischer, and D. Abbott, Sensing the hygroscopicity of polymer and copolymer materials using terahertz time-domain spectroscopy. Applied Optics, 2009. **48**(12): pp. 2262-2266.

13. C. Jördensa, S. Wietzkea, M. Schellera, and M. Koch, Investigation of the water absorption in polyamide and wood plastic composite by terahertz time-domain spectroscopy. Polymer Testing, 2009. **29**(2): pp. 209-215.

14. B. B. Hu and M. C. Nuss, *Imaging with terahertz waves.* Optics Letters, 1995. **20**(16): pp. 1716-1718.

15. D. Mittleman, *T-Ray Imaging.* IEEE Journal of selected optics in quantum electronics, 1996. **2**(3): pp. 679-692.

16. S. Wang and X-C. Zhang, *Pulsed terahertz tomography.* Journal of Physics D: Applied Physics 2004. **37**(4): pp. R1-R36.

17. D. M. Mittleman, *Sensing with Terahertz Radiation* 1ed. Springer series in Optical Sciencees. Vol. 85. 2002: Springer.

18. W. L. Chan, J. Deibel, and D. M. Mittleman, *Imaging with terahertz radiation.* Reports on Progress in Physics, 2007. **70**: pp. 1325-1379.

19. *T-Ray 2000 Manual*, Picometrix Inc.

20. J. V. Rudd and D. M. Mittleman, *Influence of substrate-lens design in terahertz time-domain spectroscopy.* Journal of Opticcal Society of America B, 2002. **19**(2): pp. 319-329.

21. S. L. Dexheimer, *Terahertz Spectroscopy: Principles and Applications (Optical Science and Engineering).* 1 ed. Terahertz Spectroscopy: Principles and Applications (Optical Science and Engineering)2007: CRC Press. 360.

22. D. M. Mittleman, M. Gupta, R. Neelamani, R. G. Baraniuk, J. V. Rudd, and M. Koch, *Recent advances in terahertz imaging.* Applied Physics B, 1999. **68**: pp. 1085-1094.

23. R. A. Cheville, R. W. McGowan, and D. Grischkowsky, *Late-time target response measured with terahertz impulse imaging.* IEEE Transactions on Antennas and Propagation, 1997. **45**(10): pp. 1518-1524.

24. V. P. Wallace, D. A. Arnone, R. M. Woodward, and R. J. Pye. Biomedical applications of terahertz pulse imaging. in Engineering in Medicine and

Biology, 2002. 24th Annual Conference and the Annual Fall Meeting of the Biomedical Engineering Society EMBS/BMES Conference, 2002. Proceedings of the Second Joint. 2002.

25. T. Loffler, T. Bauer, K. Siebert, H. Roskos, A. Fitzgerald, and A. Czasch, *Terahertz dark-field imaging of biomedical tissue.* Optics Express, 2001. **9**(12): pp. 616-621.

26. N. Karpowicz, H. Zhong, J. Xu, K-I. Lin, J-S. Hwang, and X-C. Zhang, *Non-destructive sub-THz CW imaging* in *Proceedings of SPIE - The International Society for Optical Engineering* 2005, SPIE: San Jose, CA. pp. 132-142.

27. S. Barbieri, J. Alton, S. S. Dhillon, H. E. Beere, M. Evans, E. H. Linfield, A. G. Davies, D. A. Ritchie, R. Köhler, A. Tredicucci, and F. Beltram, *Continuous-wave operation of terahertz quantum-cascade lasers.* IEEE Journal of Quantum Electronics, 2003. **39**(4): pp. 586-591.

28. A. Redo, N. Karpowicz, and X-C. Zhang. Sensing and imaging with continuous-wave terahertz systems in Review of Progress in Quantitative Nondestructive. 2006. Brunswick: AIP Conference Proceedings.

29. Q. Song, Y. Zhao, A. Redo-Sanchez, C. Zhang, and X. Liu, *Fast continuous terahertz wave imaging system for security.* Optics Communications, 2009. **282**(10): pp. 2019-2022.

30. S. Bauerschmidt, S. Preu, S. Malzer, G. H. Döhler, L. J. Wang, H. Lu, and A. C. Gossard, Continuous wave terahertz emitter arrays for spectroscopy and imaging applications, in Proceedings of SPIE - The International Society for Optical Engineering 2010, SPIE Proceedings.

31. P. Bing, J. Yao, D. Xu, X. Xu, and Z. Li, High quality continuous-wave imaging at 2.53 THz, in Proceedings of SPIE - The International Society for Optical Engineering 2010, SPIE: Beijing, China.

32. Q. Li, Q. Yin, R. Yao, S. Ding, and Q. Wang, *Continuous-wave terahertz scanning image resolution analysis and restoration.* Optical Engineering, 2010. **49**(3): p. 037007.

33. A. Nahata, J. T. Yardley, and T. F. Heinz, Coherent electro-optic detection of continuous-wave terahertz radiation, in 13th Annual Meeting. IEEE Lasers and Electro-Optics Society 2000: Rio Grande. pp. 37-38.

34. E. Budiarto, S. Jeong, J. Son, J. Margolies, and J. Boker, High power terahertz radiation at 1kHz repetition rate in Proceedings of the 1995 8th Annual Meeting of the IEEE Lasers and Electro-Optics Society 1995: San Francisco, CA, USA. pp. 220-221.

35. S. Verghese, *Highly tunable fiber-coupled photomixers with coherent terahertz output power.* IEEE Transactions on Microwave Theory and Techniques, 1997. **45**(8): pp. 1301-1309.

36. B. Kapilevich, Y. Pinhasi, M. Anisimov, R. Arusi, B. Litvak, and D. Hardon, Single pixel THz detector for remote imaging in IEEE International Conference on Microwaves, Communications, Antennas and Electronics Systems2009: Tel Aviv. pp. 1-4.

37. J. F. Whitaker, F. Gao, and Y. Liu, Terahertz bandwidth pulses for coherent time-domain spectroscopy in Proceedings of SPIE - The International Society for Optical Engineering1994: Los Angeles, CA, USA. pp. 168-177.

38. E. Budiarto, N. W. Pu, S. Jeong, and J. Bokor, *Near-field propagation of terahertz pulses from a large-aperture antenna.* Optics Letters, 1998. **23**(3): pp. 213-215.

39. P. G. Huggard, C. J. Shaw, J. A. Cluff, and S. R. Andrews, *Polarization-dependent efficiency of photoconducting THz transmitters and receivers.* Applied Physics Letters, 1992. **72**(17): pp. 2069-2071.

40. J. V. Rudd, D. Zimdars, and M. Warmuth, Compact, fiber-pigtailed, terahertz imaging system in Proceedings of SPIE - The International Society for Optical Engineering2000: San Jose, CA, USA. pp. 27-35.

41. L. Yifei, J. C. Amarildo, Vieira, M. Samuel, Goldwasser, and R. H. Peter, *Rapidly Tunable Millimeter-Wave Optical Transmitter for lidarhadar.* IEEE Transactions on Microwave Theory and Techniques, 2001. **49**(10 II): pp. 2048-2054.

42. J. W. Shi, S. W. Chu, M. C. Tien, C. K. Sun, Y. J. Chiu, and J. E. Bowers, *Edge-coupled membrane terahertz photonic transmitters based on metal-semiconductor-metal traveling-wave photodetectors.* Applied Physics Letters, 2002. **81**(27): pp. 5108-5110.

43. S. Coleman and D. Grischkowsky, *Parallel plate THz transmitter.* Applied Physics Letters, 2004. **84**(5): pp. 654-656.

44. R. Mendis, C. Sydlo, J. Sigmund, M. Feiginov, P. Meissner, and H. L. Hartnagel, *Coherent generation and detection of continuous terahertz waves using two photomixers driven by laser diodes.* International Journal of Infrared and Millimeter Waves, 2005. **26**(2): pp. 201-207.

45. T. F. Kao, H. H. Chang, L. J. Chen, J. Y. Lu, A. S. Liu, Y. C. Yu, R. B. Wu, W. S. Liu, J. I. Chyi, and C. K. Sun, *Frequency tunability of terahertz photonic transmitters.* Applied Physics Letters, 2006. **88**(9).

46. L. J. Chen, T. F. Kao, J. Y. Lu, and C. K. Sun, A simple terahertz spectrometer based on a low-reflectivity Fabry-Perot interferometer using Fourier transform spectroscopy. Optics Express, 2006. **14**(9): pp. 3840-3846.

47. D. O. Caplan, *Laser communication transmitter and receiver design.* Journal of Optical and Fiber Communications Research, 2007. **4**(4): pp. 225-362.

48. M. Van Exter, C. Fattinger, and D. Grischkowsky, *High-brightness terahertz beams characterized with an ultrafast detector.* Applied Physics Letters, 1989. **55**(4): pp. 337-339.

49. Y. C. Stephen and M. Y. Liu, *Nanoscale tera-hertz metal-semiconductor-metal photodetectors.* IEEE Journal of Quantum Electronics, 1992. **28**(10): pp. 2358-2368.

50. S. Y. Chou, Y. Liu, and P. B. Fischer, Tera-hertz GaAs metal-semiconductor-metal photodetectors with 25 nm finger spacing and finger width. Applied Physics Letters, 1992. **61**(4): pp. 477-479.

51. I. Wilke, W. Herrmann, and F. K. Kneubühl, *Integrated nanostrip dipole antennas for coherent 30 THz infrared radiation.* Applied Physics B: Lasers and Optics, 1994. **58**(2): pp. 87-95.

52. A. Rice, Y. Jin, X.F. Ma, X-C. Zhang, D. Bliss, J. Larkin, and M. Alexander, *Terahertz optical rectification from* 〈110〉 *zinc-blende crystals.* Applied Physics Letters, 1994. **64**(11): pp. 1324-1326.

53. Q. Wu, M. Litz, and X-C. Zhang, *Broadband detection capability of ZnTe electro-optic field detectors.* Applied Physics Letters, 1996. **68**(21): pp. 2924-2926.

54. L. Vicarelli, M. S. Vitiello, D. Coquillat, A. Lombardo, A. C. Ferrari, W. Knap, M. Polini, V. Pellegrini, and A. Tredicucci, *Graphene field-effect transistors as room-temperature terahertz detectors.* Nature Materials, 2012. **11**(10): pp. 865-871.

55. M. Tani, K. Sakai, and H. Mimura, *Ultrafast photoconductive detectors based on semi-insulating GaAs and InP.* Japanese Journal of Applied Physics, 1997. **36**(9): pp. L1175-L1178.

56. Y. Cai, I. Brener, J. Lopata, J. Wynn, L. Pfeiffer, and J. F. Federici, *Design and performance of singular electric field terahertz photoconducting antennas.* Applied Physics Letters, 1997. **71**(15): pp. 2076-2078.

57. P. Gu, M. Tani, K. Sakai, and T. R. Yang, Detection of terahertz radiation from longitudinal optical phonon-plasmon coupling modes in InSb film using an

ultrabroadband photoconductive antenna. Applied Physics Letters, 2000. **77**(12): pp. 1798-1800.

58. O. Mitrofanov, I. Brener, M. C. Wanke, R. R. Ruel, J. D. Wynn, A. J. Bruce, and J. F. Federici, Thin terahertz detectors and emitters based on low-temperature-grown GaAs on sapphire, in Pacific Rim Conference on Lasers and Electro-Optics2000: San Francisco, CA, USA. pp. 528-529.

59. O. Mitrofanov, R. Harel, R. Lee, L. Pfeiffer, L. N. West, J. Wynn, and J. F. Federici, *Study of single-cycle pulse propagation inside a terahertz near-field probe.* Applied Physics Letters, 2001. **78**(2): pp. 252-254.

60. H. C. Liu, C. Y. Song, A. J. SpringThorpe, and J. C. Cao, *Terahertz quantum-well photodetector.* Applied Physics Letters, 2004. **84**(20): pp. 4068-4070.

61. W. Knap, F. Teppe, Y. Meziani, N. Dyakonova, J. Lusakowski, F. Boeuf, T. Skotnicki, D. Maude, S. Rumyantsev, and M. S. Shur, *Plasma wave detection of sub-terahertz and terahertz radiation by silicon field-effect transistors.* Applied Physics Letters, 2004. **85**(4): pp. 675-677.

62. Z. Jiang and X-C. Zhang, *Electro-optic measurement of THz field pulses with a chirped optical beam.* Applied Physics Letters, 1998. **72**(16): pp. 1945-1947.

63. N. Karpowicz, H. Zhong, J. Xu, K. I. Lin, J. S. Hwang, and X-C. Zhang, *Comparison between pulsed terahertz time-domain imaging and continuous wave terahertz imaging.* Semiconductor Science and Technology, 2005. **20**(7): pp. S293-S299.

64. D. Mittleman, S. Hunsche, L. Boivin, and M. C. Nuss, *T-ray tomography.* Optics Letters, 1997. **22**(12): pp. 904-906.

65. A. W. M. Lee, Q. Qin, S. Kumar, B. S. Williams, Q. Hu, and J. L. Reno, *Real-time terahertz imaging over a standoff distance.* Applied Physics Letters, 2006. **89**(141125).

66. R. Cierniak, X-Ray Computed Tomography in Biomedical Engineering. 1st ed2011: Springer. 319.

67. Q. Li, Y. D. Li, D. Sheng-Hui, and W. Qi, *Terahertz Computed Tomography Using A Continuous-Wave Gas Laser.* Journal of Infrared, Millimeter, and Terahertz Waves, 2012. **33**(5): pp. 548-558.

68. E. Abraham, Y. Oghi, T. Araki, and T. Yasui, Continuous-wave terahertz tomography with phase unwrapping, in 2011 Conference on Lasers and Electro-Optics Europe and 12th European Quantum Electronics Conference, CLEO EUROPE/EQEC2011, IEEE: Munich, Germany. p. 1.

106

69. S. Mukherjee and J. F. Federici, Study of structural defects inside natural cork by pulsed terahertz tomography, in IRMMW-THz 2011 - 36th International Conference on Infrared, Millimeter, and Terahertz Waves 2011: Houston, Texas, USA. p. 85.

70. S. Zhong, Y-C. Shen, L. Ho, R. K. May, J. A. Zeitler, M. Evans, and P. Kleinebudde, Non-destructive quantification of pharmaceutical tablet coatings using terahertz pulsed imaging and optical coherence tomography. Optics and Lasers in Engineering, 2011. **49**(3): pp. 361-365.

71. B. Ferguson, S. Wang, D. Gray, D. Abbot, and X-C. Zhang, *T-ray computed tomography.* Optics Letters, 2002. **27**(15): pp. 1312-1314.

72. S. Wang, B. Ferguson, D. Abbott, and X-C. Zhang, *T-ray imaging and tomography.* Journal of Biological Physics, 2003. **29**(2-3): pp. 247-256.

73. A. Wei-Min-Lee, K. Tsung-Yu, D. Burghoff, Q. Hu, and J. Reno, *Terahertz tomography using quantum-cascade lasers.* Optics Letters, 2012. **37**(2): pp. 217-219.

74. J. Radon, Über die Bestimmung von Funktionen durch ihre Integralwerte längs gewisser Mannigfaltigkeiten. Sächsische Akademie der Wissenschaften zu Leipzig, 1917. **69**: pp. 262-277.

75. A. C. Kak and M. Slanley, *Principles of computerized Tomographic Imaging.* IEEE Press2001: Society for Industrial and Applied Mathematics. p.327.

76. T. Buma and T.B. Norris, *Time reversal three-dimensional imaging using single-cycle terahertz pulses.* Applied Physics Letters, 2004. **84**(12): pp. 2196-2198.

77. A. Brahm, M. Bauer, T. Hoyer, H. Quast, T. Loeffler, S. Riehemann, G. Notni, andA. Tunnermann, All-electronic 3D computed THz tomography, in Infrared, Millimeter and Terahertz Waves (IRMMW-THz), 2011 36th International Conference on2011, IEEE: Houston, TX. pp. 1-2.

78. D. J. Roth, S. B. Reyes-Rodriguez, D. A. Zimdars, R. W. Rauser, and W. W. Ussery, *Terahertz computed tomography of NASA thermal protection system foam materials.* Materials Evaluation, 2011. **69**(9): pp. 1090-1098.

79. W. Sun, X. Wanl, Y. Cui, and Y. Zhang, Continuous- wave Terahertz Tomography with Phase Unwrapping, in The European Conference on Lasers and Electro-Optics2011: Munich, Germany. p. 1.

80. X. Yin, B. Wai-Him, J. A. Zeitler, K. L. Nguyen, L. F. Gladden, and D. Abbott, *Local Computed Tomography Using a THz Quantum Cascade Laser.* Sensors Journal, IEEE, 2010. **10**(11): pp. 1718-1731.

81. D. M. Koller, G. Hannesschläger, M. Leitner, and J. G. Khinast, *Non-destructive analysis of tablet coatings with optical coherence tomography.* European journal of pharmaceutical sciences, 2011. **44**: pp. 142-148.

82. M. G. Vlasenko, V. V. Pickalov, D. G. Rodionov, and B. A. Knyazev, Tomography using a high-power terahertz free electron laser, in Infrared, Millimeter and Terahertz Waves (IRMMW-THz), 2011 36th International Conference2011: Houston, TX.

83. M. Tsubouchi, M. Nagai, and Y. Ohshima, Terahertz tomography of a photo-induced carrier based on pump-probe spectroscopy using counterpropagation geometry. Optics Letters, 2012. **37**(17): pp. 3528-3530.

84. A. W. M. Lee, K. Tsung-Yu, D. Burgoff, Q. Hu, and J. L. Reno. THz optical coherence tomography based on quantum cascade lasers. in Infrared, Millimeter and Terahertz Waves (IRMMW-THz), 2011 36th International Conference on. 2011. Houston, TX: IEEE.

85. M. Bessou, B. Chassagne, J. P. Caumes, C. Pradère, P. Maire, M. Tondusson, and E. Abraham, *Three-dimensional terahertz computed tomography of human bones.* Applied Optics, 2012. **51**(28): pp. 6738-6744.

86. B. Ferguson, S. Wang, D. Gray, D. Abbott, and X-C. Zhang., *Towards functional 3D T-ray imaging.* Physics in Medicine and Biology, 2002. **47**(21): pp. 3735-3742.

87. X-C. Zhang, *Three-dimensional terahertz wave imaging.* Philosophical Transactions of The Royal Society A, 2003. **362**: pp. 283-299.

88. A. J. Teti, D. E. Rodriguez, J. F. Federici, and C. Brisson, *Non-Destructive Measurement of Water Diffusion in Natural Cork Enclosures Using Terahertz Spectroscopy and Imaging.* Journal of Infrared Millimeter and THz Waves, 2011. **32**(4): pp. 513-527.

89. J. F. Federici, *Review of moisture and liquid detection and mapping using Terahertz imaging.* Journal of Infrared, Millimeter, and Terahertz Waves, 2012. **33**(2): pp. 97-126.

90. E. Abraham, A. Younus, C. Aguerre, P. Desbarats, and P. Mounaix, *Refraction losses in terahertz computed tomography.* Optics Communications 2010. **283**(10): pp. 2050-2055.

91. B. Recur, J. P. Guillet, I. Manek-Hönninger, J. C. Delagnes, W. Benharbone, P. Desbarats, J. P. Domenger, L. Canioni, and P. Mounaix, *Propagation Beam Consideration for 3D THz Computed Tomography.* Optics Express, 2012. **20**(6): pp. 5817-5829.

92. S. Wang and X.-C. Zhang, *Pulsed terahertz tomography.* Journal of Physics D: Applied Physics, 2004. **37**(4): pp. R1-R36.

93. E. Hecht, *Optics.* 4 ed2001: Addison Wesley. 680.

94. E. D. Hirleman and W. H. Stevenson, *Intensity distribution properties of a Gaussian laser beam focus.* Applied Optics, 1978. **17**(21).

95. H. Pereira, *Cork: Biology, Production and Uses.* 1 ed2007: Elsevier Science. 346.

96. L. Belair and S. Villaume, Losses of dissolved CO2 through the cork stopper during champagne aging: Toward a multiparameter modeling. Journal of Agricultural and Food Chemistry, 2011. **59**(8): pp. 4051-4056.

97. J. R. González-Adrados, F. González-Hernández, J. L. García De Ceca, M. J. Cáceres-Esteban, and M. C. García-Vallejo, *Wine absorption by cork stoppers.* Spanish Journal of Agricultural Research, 2008. **6**(4): pp. 645-649.

98. P. Lopes, C. Saucier, and Y. Glories, *Nondestructive colorimetric method to determine the oxygen diffusion rate through closures used in winemaking.* Journal of Agricultural and Food Chemistry, 2005. **53**(18): pp. 6967-6973.

99. L. Brotto, F. Battistutta, L. Tat, P. Comuzzo, and R. Zironi, *Modified nondestructive colorimetric method to evaluate the variability of oxygen diffusion rate through wine bottle closures.* Journal of Agricultural and Food Chemistry 2010. **58**(6): pp. 3567-3572.

100. P. Lopes, C. Saucier, P-L. Teissedre, and Y. Glories, *Main routes of oxygen ingress through different closures into wine bottles.* Journal of Agricultural and Food Chemistry, 2007. **55**(13): pp. 5167-5170.

101. P. Lopes, C. Saucier, P-L. Teissedre, and Y. Glories, *Impact of storage position on oxygen ingress through different closures into wine bottles.* Journal of Agricultural and Food Chemistry, 2006. **54**(18): pp. 6741-6746.

102. V. L. Singleton, E. Trousdale, and J. Zaya, *Oxidation of Wines. I. Young White Wines Periodically Exposed to Air.* American journal of Enology and Viticulture, 1979. **30**(1): pp. 49-54.

103. P. Ribéreau-Gayon, P. Pontallier, and Y. Glories, *Some interpretations of color changes in young red wines during their conservation* Journal of the Science of Food and Agriculture, 1983. **34**(5): pp. 505-516.

104. J. Ribéreau-Gayon, *Dissolution d'oxygène dans les vins* 2ed. Contribution à l'Étude des Oxidations et Réductions Dans Les Vins. Application à l'Étude de Vieillissement et des Casses1933, Bordeaux, France.

105. A. Hart and A. Kleinig, The role of oxygen in the aging of bottled wine in Wine Press Club New South Wales Inc2005. pp. 1-14.

106. M. E. Rosa and M. A. Fortes, *Water absorption by cork.* Wood and Fiber Science, 1993. **25**(4): pp. 339-348.

107. A. Şena, T. Quilhób, and H. Pereira, *The cellular structure of cork from Quercus cerris var. cerris bark in a materials' perspective.* Industrial Crops and Products, 2011. **34**(1): pp. 929-936.

108. Y. Hor, J. F. Federici, and R. L. Wample, Non-destructive evaluation of cork enclosures using terahertz/millimeter wave spectroccopy and imaging. Applied Optics, 2008. **47**(1): pp. 72-78.